ABSTRACT

VO, LONG HOANG. Natural Frequency and Soil Damping Analyses for Monopile Foundation Supporting Offshore Wind Turbines and Hybrid Wind-Wave Energy Systems. (Under the direction of Dr. Mohammed Gabr)

Improving reliability and facilitating computation of natural frequency, $f_{1,d}$, and foundation damping, ξ_{fn}, of offshore monopile wind turbine are the aims of this study. Three-dimensional numerical analyses are performed to determine dynamic characteristics of the wind turbine structure assuming several configurations of soil conditions and monopile dimensions. The correlations between pile lateral displacement and rotation at seabed level caused by excitation load and natural frequency and foundation damping obtained from dynamic analyses are established. The derived relationships are used to estimate natural frequency and foundation damping of monopile-supported structures in other settings, namely with presence of scour and in form of hybrid wind-wave system with mounted hydrokinetic devices.

Influences of soil stress history parameters including overconsolidation ratio (OC), and coefficient of earth pressure at rest (K_0) on lateral behavior of single pile are investigated before performing dynamic analyses. The overconsolidation ratio OCR is concluded to have pivotal role in analyses of lateral loaded pile. It affects the magnitude of soil shear modulus, constitutive stress-strain response of soil elements and consequently the outcome of the analyses. A modification the existing empirical relationship between soil maximum shear modulus (G_o) and Cone Penetration Test point resistance (q_c) by introducing two coefficients accounting for soil OCR and vertical effective stress. Soil model parameters are defined by empirical relationships to q_c. Hardening soil with small strain (HSsmall) constitutive model is employed for simulation and the ratios of $G_{ur}^{ref} / G_o^{ref} = 0.3$ and $E_{ur}^{ref} / E_{50}^{ref} = 4$ for model modulus parameters are obtained from model calibration.

Dynamic parametric study on effects of soil relative density, D_R, pile diameter, D_P, and pile embedment, L_P, on $f_{1,d}$ and ξ_{fnd} is performed. A foundation rigidity coefficient, defined as $\lambda = f_{1,d} / f_{1,FB}$, is proposed to express level of foundation fixity relatively to a perfectly fixed restraint case. The D_P appears to have a larger impact on dynamic properties

but the change caused by D_P variation largely comes from change in frequency of fixed based system, $f_{1,FB.}$ In the case of effect of L_P, most of the variation in $f_{1,d}$ and ξ_{fnd} appears when L_P is reduced below the critical length for constant displacement, $L_{c,const}$. Natural frequency also declines faster as scour develops below a certain depth, where the pile effective embedment is equal to $L_{c,const}$

Regression analysis results using data from the parametric study show strong correlation between on $f_{1,d}$ and ξ_{fnd} and monopile lateral displacement, y_o, and rotation, θ_o, caused by excitation load at seabed level. $f_{1,d}$ is best correlated to normalized displacement, y_o/D_P, and ξ_{fnd} has strongest correlation to θ_o. Correlations between these pairs of parameters are formulated. Within the bounds of the parameters utilized herein, the use of the proposed $f_{1,d}$ - y_o/D_P relationship estimates well the natural frequency of existing offshore wind turbines compared to field measurements. It also provides results very close to those obtained by numerical analyses for wind turbines with scour and hybrid systems. The ξ_{fnd} - θ_o correlation, however, yields lower level of agreement with numerical analyses for these cases and it use requires further improvements in future studies.

Natural Frequency and Soil Damping Analyses for Monopile Foundation Supporting Shared Anchoring of Offshore Wind Turbines and Wave Energy Systems

by
Long Hoang Vo

A dissertation submitted to the Graduate Faculty of
North Carolina State University
in partial fulfillment of the
requirements for the degree of
Doctor of Philosophy

Civil Engineering

Raleigh, North Carolina
2022

APPROVED BY:

_____	_____
Dr. Mohammed Gabr Committee Chair	Dr. Roy Borden
_____	_____
Dr. Mervyn Kowalsky	Dr. Brina Montoya
_____	
Dr. Ashly Cabas Mijares	

DEDICATION

I dedicate this work to my grandmother, Sinh Pham, who passed away of cancer in August 2021, when it was the peak of Covid-19 pandemic in my country. While being unable to properly mourn her took a toll on me during the late stage of my study, I insisted myself that finishing this was the best way to tribute her and honor her love and belief in me.

BIOGRAPHY

Long Vo was born and raised in Vinh City, Vietnam, and moved to Hanoi and Ho Chi Minh City for undergraduate study and developing career, respectively. He completed Bachelor's degree in Civil Engineering in 2002 at National University of Civil Engineering in Vietnam, and had been working as structural engineer ever since. He was on Vietnam Education Foundation fellowship to continue his education into graduate school and accomplished Master of Science degree in Civil Engineering at North Carolina State University in 2016. He received the Ph.D. in Civil Engineering with an emphasis in geotechnical engineering in Spring 2022. He intends to develop a career in offshore geotechnical engineering and work in marine renewable energy sector

ACKNOWLEDGMENTS

I would like to express my gratitude to my advisor and mentor, Dr. Mohammed Gabr, for his mentorship, support, direction, and friendship throughout my study at NC State. He has been providing extensive knowledge, and helpful support and guidance throughout the research and preparation of this dissertation. I also would like to extend my appreciation to Dr Roy Borden, who has worked tirelessly with me and Dr Gabr and provided invaluable feedback, advice, and questions for me to complete this study. I would like to show my deep gratefulness for the support they gave me during the Covid-19 pandemic, when, at times, I found it struggle and missed my targets.

I also would like to thank Dr Mervyn Kowalsky, Dr Brina Mortensen Montoya, and Dr Ashly Cabas for being members of my committee, providing knowledge and contribution to my education and this research, and their long-term friendship. The experiences I have had with them in classrooms, and while working with them in research and teaching are valuable for me academically and professionally.

I also would like to thank North Carolina Renewable Ocean Energy Program (NCOEP) and UNC Coastal Studies Institute for the financial support that made this research program possible

Many thanks go to other Professors and friends in Geotechnical group for their helps at times and friendship over this remarkable stage of life.

Finally, and most importantly, my deepest appreciation goes to my beloved wife, Trinh Phan, for boundless support and patience in this journey with me and my sons, Khoi Vo and Ethan Vo, for pressing me to graduate before they respectively go to middle and elementary school.

TABLE OF CONTENTS

LIST OF TABLES ix

LIST OF FIGURES xi

CHAPTER 1. INTRODUCTION 1

1.1. Background 1
1.2. Scope of work 5
1.3. Dissertation layout 5

CHAPTER 2: ROLES OF SOIL STRESS HISTORY IN RESPONSE OF LATERALLY LOADED PILE EMBBBED IN SAND. 7

2.1. Introduction 7
2.2. Soil stress history indicators 10
2.3. CPT-based soil stress history parameters 12
2.4. Impact of OCR on G_o 13
2.5. Soil reaction induced by laterally loaded pile 15
2.6. American Petroleum Institute (API) p-y curves for sand 17
2.7. Input for numerical simulations 18
2.7.1. Test site 19
2.7.2. Test piles 20
2.8. Numerical simulation 22
2.8.1. Shear modulus degradation curve in small strain region 22
2.8.2. Soil modulus parameters for HSsmall model 24
2.8.3. Shear strength parameters 25
2.8.4. Soil history assumptions and 3D model 25
2.9. Analyzing results on impact of soil history 26
2.9.1. Model parameters for Case 1 26
2.9.2. Influences of OCR 27
2.9.3. Influences of K_0 28
2.9.4. Influences of pile installation. 29
2.10. Soil reactions generated from 3D models. 30
2.10.1. Effect of OCR on soil reactions 32
2.10.2. Contribution of soil reaction components 33
2.11. P-y curves generated by numerical simulation versus API recommendations. 34

2.12. Validation of model parameters for loose sand 37
2.12.1. Test pile set-up 37
2.12.2. Soil condition and pile installation 39
2.12.3. Model parameters for pile 40
2.12.4. Model parameters for soil 40
2.12.5. Simulation results 41
2.13. Conclusions and Recommendations 44
CHAPTER 3. NATURAL FREQUENCY AND FOUNDATION DAMPING OF MONOPILE-SUPPORTED OFFSHORE WIND TURBINE IN SANDY GROUND. 47
3.1. Introduction 47
3.2. Overview on natural frequency and soil damping of monopile wind turbine 50
3.2.1. Determination of natural frequency of monopile wind turbines 50
3.2.2. Foundation damping for monopile wind turbines 52
3.2.3. Impacts of monopile dimensions on system natural frequency and foundation damping 53
3.2.4. Closed-formed solution for Eigen frequency by Arany, et al. (2016) 55
3.3. Selection of monopile dimensions 57
3.3.1. Wind loading on monopile 57
3.3.2. Wave loading on pile 58
3.3.3. Wind and waves conditions 59
3.3.4. Monopile embedded length and diameter 59
3.4. Input for numerical simulations 61
3.4.1. CPT-based soil parameters 61
3.4.2. Shear modulus degradation curve and hysteretic damping in HSsmall model 63
3.1.1. Soil modulus parameters for HSsmall model 65
3.5. Wind turbines for model calibration and parametric study 66
3.5.1. Model Calibration 66
3.5.2. Parametric study 68
3.5.3. Loading scenario for dynamic analyses 69
3.6. Numerical model 69
3.6.1. Simulation description 69
3.7. Model calibration results 72
3.7.1. Model Calibration. 72

3.7.2. Effect of ground loading history assumption 72
3.8. Parametric study results 73
3.8.1. Natural frequency of fixed base system 73
3.8.2. Impact of pile embedded length on natural frequency and foundation damping 74
3.8.3. Impact of pile diameter on natural frequency and foundation damping 75
3.8.4. Comparison of obtained results with previous studies' outcomes 76
3.9. Discussion on obtained results 78
3.9.1. Obtained results in design context 78
3.9.2. Dynamic amplification factor of wave load 79
3.9.3. Role of critical embedment 80
3.10. Conclusions 81
CHAPTER 4: APPROACHES FOR DETERMINING NATURAL FREQUENCY AND FOUNDATION DAMPING OF MONOPILE-SUPPORTED WIND TURBINE AND HYBRID WIND WAVE SYSTEM 84
4.1. Introduction 84
4.2. Determination of natural frequency of monopile wind turbines 87
4.2.1. Numerical approaches for determining natural frequency of monopile wind turbines 87
4.2.2. Closed-formed solution for Eigen frequency by Arany, et al. (2016) 88
4.2.3. Monopile foundation stiffness 91
4.2.4. Effects of soil relative density, pile embedded length, and pile diameter on monopile wind turbine natural frequency and foundation damping 93
4.2.5. Effect of scour on natural frequency of monopile wind turbine 96
4.3. Approach 1: Estimating system natural frequency and foundation damping by correlations with pile deformations at mudline level derived from numerical analyses. 98
4.3.1. Procedure of establishing the relationships 99
4.3.2. Pile deformations – foundation rigidity coefficient relationships 99
4.3.3. Pile deformations – foundation damping ratio relationships 99
4.3.4. Foundation rigidity coefficient – foundation damping relationship 103
4.4. Approach 2: Estimating natural frequency by computing K_L, K_R, and K_{LR} from pile deformations at mudline level caused by excitation load 104
4.4.1. Calculation procedure 104
4.4.2. Results on foundation rigidity coefficient 105

4.4.3. Recommendation on soil modulus, E_{S0}, in established equations for K_L, K_R, and K_{LR} 105
4.5. Applying developed approaches to estimate natural frequency and foundation damping of existing monopiles offhore winf turbines 107
4.6. Natural frequency and foundation damping of monopile offshore wind turbine with presence of local scour 108
4.6.1. Numerical simulation of monopile with local scour 108
4.6.2. Simulation outcomes for monopile with local scour 109
4.6.3. Estimating impacts of scour on $f_{1,d}$ and ξ_{fdn} by Approach 1 110
4.7. Natural frequency and foundation damping of monopile-supported hybrid system. 113
4.7.1. Numerical simulation of hybrid system 113
4.7.2. Simulation outcomes for monopile with local scour 114
4.7.3. Estimating $f_{1,d}$ and ξ_{fdn} of hybrid system by Approach 1 114
4.8. Conclusions 116
CHAPTER 5. SUMMARY OF CONCLUSIONS, CONTRIBUTIONS, AND RECOMMENDATIONS 119
5.1. Summary of Conclusions 119
5.2. Summary of Contributions 121
5.3. Summary of Recommendations for Future Research 121
REFERENCES 123
APPENDICES 134
7.1. Appendix A. Data on natural frequency and foundation damping resulted from dynamic analyses 135
7.2. Appendix B. Data on pile deformations at mudline and dynamic properties resulted from numerical simulations. 137
7.3. Appendix C. Data natural frequency and foundation damping resulted from numerical simulations for monopile with presence of local scour 138

LIST OF TABLES

Table 2.1. Pile test specifications (McAdam et al., 2019) 22

Table 2.2. Summary of soil model parameters 25

Table 2.3. Computation cases 26

Table 2.4. Force equilibrium check for lateral loads 33

Table 2.5. Input of k_h (API, 2020) and ϕ' (Zdravković et al., 2019) for API p-y curves 35

Table 2.6. Pile S5 cross section parameters (Aguirre et al., 2018) 39

Table 3.1. Simulation scenarios for foundation (Arany et al., 2017) 61

Table 3.2. Wind turbine data (after Arany et al. (2016)) 67

Table 3.3. Met-ocean data (after Jalbi et al. (2019)) 68

Table 3.4. Matrix of analyses on natural frequency and soil damping. 69

Table 3.5. Summary of wind and wave load for normal and operational condition. 70

Table 3.6. Results of simulations for model calibration. 73

Table 3.7. Results of simulations with NC soil. 73

Table 3.8. Fixed base system first natural frequency, $f_{1,FB}$ 74

Table 3.9. Soil parameters for closed-form solution for natural frequency 78

Table 4.1. Established foundation static stiffness formulae for parabolic soil modulus profile 92

Table 4.2. $y_o/D_P - \lambda$ relationship 100

Table 4.3. $\theta_o - \lambda$ relationship 101

Table 4.4. $y_o/D_P - \xi_{fdn}$ relationship 102

Table 4.5. $\theta_o - \xi_{fdn}$ relationship 103

Table 4.6. $\lambda - \xi_{fdn}$ relationship 104

Table 4.7. Data for computing λ and ξ_{fdn} for Burbo Bank and Walney 1 projects 108

Table 4.8. λ obtained from different methods for Burbo Bank and Walney 1 projects 108

Table 4.9. ξ_{fdn} obtained from different methods for Burbo Bank and Walney 1 projects 108

Table 4.10. Matrix of analyses of monopile with local scour 109

Table 4.11. $f_{1,FB}$ computed at different locations of fixed restraint 112

Table 4.12. Data for simulations of hybrid system 113

Table 4.13. $f_{1,FB}$ computed with different M_{MHK} 115

Table 4.14. Change in $f_{1,d}$ caused by selected MHK device for monopiles with L_P=38m and 31.2m 115

Table 4.15. Change in ξ_{fdn} caused by selected MHK device for monopiles with L_P=38m .. 115

Table 4.16. Change in ξ_{fdn} caused by selected MHK device for monopiles with L_P=31.2m 115

Table 7.1. Natural frequency of D_P=5.0m monopile 135

Table 7.2. Natural frequency of D_P=4.7m monopile 135

Table 7.3. Natural frequency of D_P=4.4m monopile 135

Table 7.4. Natural frequency of D_P=4.0m monopile 136

Table 7.5. Foundation damping of D_P=5.0m monopile 136

Table 7.6. Foundation damping of D_P=4.7m monopile 136

Table 7.7. Foundation damping of D_P=4.4m monopile 136

Table 7.8. Foundation damping of D_P=4.0m monopile 137

Table 7.9. λ obtained from FE simulations and Approach 1 for monopile with L_P=38.0m and presence of local scour. 138

Table 7.10. λ obtained from FE simulations and Approach 1 for monopile with L_P=24.0m and presence of local scour. 139

Table 7.11. ξ_{fdn} obtained from FE simulations and Approach 1 for monopile with L_P=38.0m and presence of local scour. 139

Table 7.12. ξ_{fdn} obtained from FE simulations and Approach 1 for monopile with L_P=24.0m and presence of local scour. 140

LIST OF FIGURES

Figure 1.1. Conceptual illustration of hybrid wind-wave energy systems on monopile and jacket structure (Perez& Iglesias, 2012) 4

Figure 2.1. Soil wedge for determining p_u at shallow depth *(Reese et al., 1974)* (left) and distributions of A_s (Reese et al., 1974) and $Q_{c,1}/Q_{c0}$ (Reese& Van Impe, 2011). 9

Figure 2.2. Paths to soil current e-σ state (Mitchell& Soga, 2005) 11

Figure 2.3. Effect of vibration on soil void ratio and K_0 (Vardhanabhuti& Mesri, 2007) 12

Figure 2.4. q_c-based correlations for G_o by Baldi et al. (1989) redrawn using equation 2-15 15

Figure 2.5. Pile-soil interface stresses and reactions (after Davidson (1982) and Zdravković et al. (2019)): distributions of stresses along pile length (a), and on pile cross-section (b), and soil reactions on pile modeled as a beam in 1D analysis (c) 16

Figure 2.6. Comparison of q_c reported by Chow (1996) and by Eq. 2-8, and of OCR and K_0 computed from in-situ tests data and from generated q_c profile based on Eq. 2-8 19

Figure 2.7. G_o profiles reported by Chow (1996) and Zdravković et al. (2019) 20

Figure 2.8. OCR and K_0 computed for q_c profiles generated by equation 2-8 and reported by Zdravković et al. (2019) 21

Figure 2.9. Comparison among G_o computed by equations 2-11 and 2-15 with actual or/and generated q_c profiles and field measurements by Chow (1996) (a) and in 2019 by Zdravković et al. (2019) (b). 21

Figure 2.10. G degradation curves in HSsmall (Brinkgreve R B J et al., 2019a). 24

Figure 2.11. 3D finite element model used in analyses. 27

Figure 2.12. Comparisons of load-ground line displacement responses of test piles DM7, DM4, DM3 and DL1 by FE simulations for Cases 1, 2, 3, and 4 listed in Table 2.3 and Taborda et al. (2019) outcomes 28

Figure 2.13. Differences in K_0 and G_o^{ref} between Cases 1, 2 and Case 3 29

Figure 2.14. Displacement profiles obtained from experimental data and numerical simulations for DM3 (left) and DL2 (right) at various load values. 30

Figure 2.15. Interface discretization (a), stress points on triangular elements (b) and stresses on elements along pile wall (c) and at pile base (d). 31

Figure 2.16. Distributions of p(z) and m(z) resulted from analyses for Case 1 and Case 2 at various values of lateral load. 33

Figure 2.17. Development of H_b (left) and M_z (right) with applied lateral load 34

Figure 2.18. Comparisons of p-y curves obtained from analyses with and without soil history consideration and by API recommendation for selected depths above (top) and below (bottom) point of rotation. 35

Figure 2.19. The depth where API's $p_{u1}=p_{u2}$ for various friction angle 36

Figure 2.20. Effect of wall friction angle on passive failure surface (Terzaghi& Peck, 1967) 37

Figure 2.21. Typical vertical displacement pattern of soil adjacent to pile and the pile wall. 38

Figure 2.22. Test pile typical cross section (Aguirre et al., 2018) 38

Figure 2.23. Pile test S5 setup (Aguirre et al., 2018) 39

Figure 2.24. Typical pile head displacement history (Aguirre et al., 2018) 40

Figure 2.25. CPT tip resistance and soil properties computed for test pile S5 41

Figure 2.26. Pile S5: Finite element model and soil domain meshing. 42

Figure 2.27. Pile S5: Pile head load-displacement response. 43

Figure 2.28. Pile S5: Displacement profile at peaks of push and pull cycles. 43

Figure 3.1. Normalized power spectral density (PSD) and frequency ranges of loads acting on offshore wind turbine system (Bhattacharya, 2019). 48

Figure 3.2. Ratio of measured to design first natural frequency for 400 OWTs (Kallehave, Byrne, et al., 2015). 50

Figure 3.3. Terminology of wind turbine components and model (Arany et al., 2016). 54

Figure 3.4. CPT cone resistance and soil properties obtained for various relative densities. 63

Figure 3.5. Hysteretic behavior of soil described in the HSsmall constitutive model. 64

Figure 3.6. Secant modulus (E_S) and tangent modulus (E_t) (left), and soil hysteretic damping ratios (right) at different strain level in HSsmall model. 66

Figure 3.7. Distribution of wave load below mean sea level (MSL) of projects in calibration and for different pile diameters in parametric study. 70

Figure 3.8. Typical model for dynamic analysis 71

Figure 3.9. Time history of lateral acceleration at turbine level of Gunfleet Sands (left) and determination of $f_{1,S}$ by power energy spectrum of lateral acceleration for 3 projects (right). 72

Figure 3.10. Comparison of input and output of analyses with NC and OC soil: (a) - G_o^{ref}, and initial σ_3' and (b) - obtained a_x 74

Figure 3.11. Effect of monopile embedded length on system first natural frequency. 75

Figure 3.12. Effect of monopile embedded length on foundation damping 76

Figure 3.13. Effect of monopile diameter on system first natural frequency resulted from FEM and equations by Arany et al. (2016). 77

Figure 3.14. Effect of monopile diameter on foundation damping 77

Figure 3.15. DAF and magnitude of wave load in normal and operational condition on monopile wind turbine at various pile diameter, embedded length, and soil D_R 80

Figure 3.16. Displacement profiles caused by excitation loads for pile with D_P=5m and various lengths of embedment in different soil relative densities 81

Figure 4.1. Normalized power spectral density (PSD) and frequency ranges of loads acting on offshore wind turbine system (Bhattacharya, 2019). 85

Figure 4.2. Terminology of wind turbine components and model (Arany et al., 2016). 89

Figure 4.3. Effect of monopile embedded length on system first natural frequency 95

Figure 4.4. Effect of monopile embedded length on foundation damping 95

Figure 4.5. Effect of monopile diameter on system first natural frequency 96

Figure 4.6. Effect of monopile diameter on foundation damping 96

Figure 4.7. Modified vertical effective stress and reaction modulus E_{py} for API p-y curves in analyses with presence of global and local scour (API, 2008) 98

Figure 4.8. Influence of scour depth on offshore wind turbine supported by monopile in different soil conditions (Prendergast et al., 2015) 98

Figure 4.9. Relationships between y_o/D_P and λ (top), and between θ_o and λ (bottom) at different soil D_R. 100

Figure 4.10. Relationships between y_o/D_P and λ, and between θ_o and λ. 101

Figure 4.11. Relationships between y_o/D_P and ξ_{fdn}, and between θ_o and ξ_{fdn} 102

Figure 4.12. $\lambda - \xi_{fdn}$ relationships at various pile diameters (left) and in general (right) 103

Figure 4.13. Comparison of λ resulted from FE analyses and Approach 2 by soil relative density, pile diameter, and embedded length 106

Figure 4.14. Comparisons of K_L (top) and K_R (bottom) resulted from solving equations 3-88and Shadlouand Bhattacharya (2016) formulae. 106

Figure 4.15. λ/λ_{FEM} ratio with λ computed by Shadlouand Bhattacharya (2016) formulae using $E_{S0}=E_{ur}$. 107

Figure 4.16. Numerical model for dynamic analyses with presence of local scour 110

Figure 4.17. Influence of local scour depth on natural frequency at various soil D_R and L_P. 111

Figure 4.18. Influence of local scour depth on ξ_{fdn} at various soil D_R and L_P. 111

Figure 4.19. Comparisons of λ (left) and ξ_{fdn} (right) by FE simulations and Approach 1 for monopile with local scour. 112

Figure 4.20. Numerical model for hybrid wind-wave system. 114

Figure 4.21. Comparisons of λ (left) and ξ_{fdn} (right) by FE simulations and Approach 1 for hybrid system. 116

Figure 7.1. Data points of (y_o/D_P, ξ_{fdn}) (top), and (θ_o, ξ_{fdn}) (bottom) at different soil D_R 137

Figure 7.2. Data points of (λ, ξ_{fdn}) at different soil D_R 138

CHAPTER 1. INTRODUCTION

1.1. Background

Developing renewable energy sources has been one of key measures to reduce greenhouse gases production and combat global warming and associated climate change. Recently, the leaders of nearly 200 countries have agreed to sign the Glasgow Climate Pact at the United Nations Climate Change Conference (COP26) and join force in actions to limit the increase in global temperature. Along with that are the pledges to diminish greenhouse gas emission by about a half by 2030 and to reach carbon neutrality by midcentury by more than 100 countries. These efforts open an enormous opportunity for renewable energy, including ocean renewable energy, to develop and fill the gap in supply due to reduction in fossil fuel usage. In fact, offshore wind is at the center of the climate agenda of Biden-Harris administration and European Union energy policy.

Renewable energy has made significant progresses in last decade. By 2018, about a third of global total electricity capacity was accounted for through the use of renewable sources, of which 7.9% was contributed by wind energy (Koebrich, et al., 2020). Moreover, renewable energy has become more cost effective. Since 2010 the global weighted average of levelized cost of electricity (LCOE) of most available renewable sources, wind energy included, has been within the range of fossil fuel-generated power costs as per a report by International Renewable Energy Agency (IRENA) (2019). The LCOE for offshore wind-generated power is more than twice as much as that of onshore wind and hydropower, which are the two least expensive renewable sources. In the US, renewable energy reached 20.5% of cumulative power capacity by 2018 (Koebrich, et al., 2020). Wind power has been one of the fastest-growing sources in capacity since 2000 replaced hydropower in terms of largest capacity by 2016 (Wiser, et al., 2015). However, American wind power has been entirely dependent on onshore wind.

The development of American offshore renewable energy, comprising of offshore wind and marine hydrokinetic (wave, tidal and current) energy, is still at very early state but with enormous potential capacity. An assessment by National Renewable Energy Lab (NREL) estimated technical resource capacity of 2,858 GW for offshore wind in the US (Musial, et al., 2016), which is more than double of 2018 total electricity capacity of 1,219

GW from all fossil and renewable sources. Other investigations on energy resource from wave, tidal streams and ocean currents by Electric Power Research Institute (EPRI) and Georgia Tech provide technical resource potential estimations of 898–1,229 TWh/year for waves energy (Jacobson, et al., 2011), 222–334 TWh/year for tidal streams energy (Haas, et al., 2011) and 45–163 TWh/year for ocean currents energy (Haas, 2013). So far, there has been only operational 30MW offshore wind project, the Block Island Wind Farm in Rhode Island, while Marine Hydrokinetic (MHK) power in US and worldwide is still in pilot deployment and test-site stage (Koebrich, et al., 2020).

Interests in offshore wind have soared due to recent release of Biden-Harris administration's ambitious Climate Agenda, with offshore wind as the driving force of renewable energy. The administration aims at expanding offshore wind energy off the US East Coast with the vision of generating 30GW of electricity by the end of the decade and has approved the first commercial scale offshore wind farm, the Vineyard Wind in Massachusetts, with a generating capacity of 800MW. The target likely leads to more wind energy areas being added to existing proposed offshore wind energy projects in the 25.8GW pipeline reported by Musial, et al. (2019), as well as acceleration in development of the projects. In the reported pipeline, North Carolina is one of three states that possess most offshore wind capacity with nearly 4GW anticipated from potential wind farm deployments off Kitty Hawk and Wilmington. The developers have site control in the former while the latter is at planning stage. Governor Roy Cooper in a letter to Bureau of Ocean Energy Management (BOEM) expressed the needs to proceed with activities to lease the Wilmington wind areas by the summer of 2022, and to identify additional wind energy areas off the North Carolina coast.

Improving cost competitiveness has been one of the biggest challenges of offshore renewable energy. Policies and investments have been focused on improving wind energy technologies and expanding large-scale offshore wind projects. The offshore wind LCOE is predicted to continue declining both globally and in the US since new projects are able to deploy state-of -the art technologies, e.g. larger and more efficient turbines, and utilize developers' global experiences (Musial, et al., 2019). On the other hand, the marine hydrokinetic (MHK) industry in the US and worldwide is still in pilot-scale testing modes and has to overcome major obstacles, including improvement of technology reliability and

reducing energy cost, before commercialization (Koebrich, et al., 2020, Laws and Epps, 2016). It is important now to direct more attention and available resources to MHK energy for a sustainable future of offshore renewable energy. The combined exploitation of wave and offshore wind energies in same marine environment is a promising approach to improving competitiveness of both sources. European Union (EU) considers collocated and hybrid offshore renewable energy approaches as fundamental component in EU energy policy and has financed two projects named ORRECA and MARINA to explore possibilities to develop diversity and combination across marine energy resources.

Integrated systems, in the form of co-located and/or hybrid systems can be attractive deployment options. Colocation refers to placement arrays of MHK devices in the vicinity of wind farms. A hybrid system, whether bottom-fixed or floating, combines wind turbine and wave and/or current converters on shared structure and anchoring (Figure 1.1). Integration of wind and MHK devices can potentially increase the energy yield per unit area of marine space and optimize the costs of installation, operation and maintenance, and supporting infrastructure. As such, the LCOE of combined marine energy system can be significantly improved in comparison with stand-alone wind and wave energy farms. LCOE of wave energy system can be reduced by more than 50% when switching from stand-alone farm to co-located farm with existing monopole wind turbines (Astariz, et al., 2015). Therefore, the opportunity to deploy wave and current devices integrated with offshore wind farms can enhance economic viability of wave energy and propel the MHK industry into expedient deployment and operation of full-scale arrays.

Foundation systems choice is a key factor in wind farm design and its costs plays a significant role in project finance, and the LCOE. Monopile has been the most common foundation selection for wind turbines in water depth of up to 30m due to both commercial and technical advantages (Kallehave, et al., 2015a). Jackets is reported to be increasingly deployed in future projects as a result of the tendency of developing wind farms in deeper water and farther from shore (Musial, et al., 2019). Monopile wind turbine is a dynamically sensitive, and lateral load and moment resisting structure that experiences a very large number of cycles of loading over its lifetime. The design is typically governed by natural frequency and serviceability limit state (SLS) criteria rather than ultimate limit state (ULS) (LeBlanc, et al., 2010).

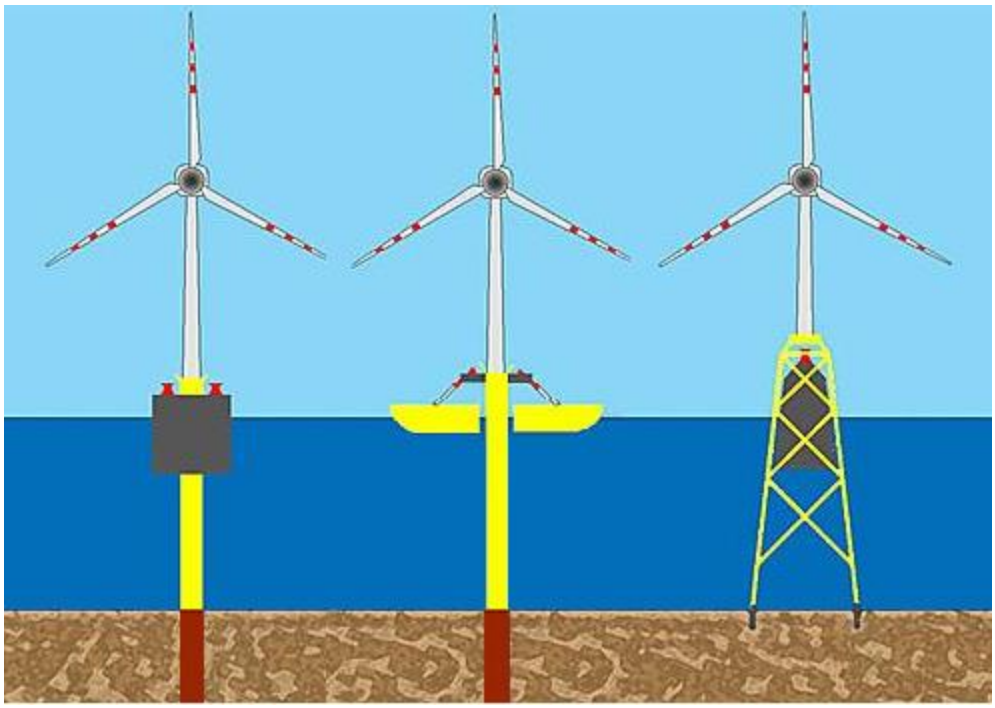

Figure 1.1. Conceptual illustration of hybrid wind-wave energy systems on monopile and jacket structure (Perez and Iglesias, 2012)

One of the most challenging and important tasks that govern the accuracy in the context of limit states analyses is determining first natural frequency, f_1, of the structure (Bhattacharya, 2014). The author suggests that the design is only conservative if f_1 is accurately estimated; however, underprediction of f_1 is generally found in design of monopile wind turbine projects (Kallehave, et al., 2015a). Natural frequency and system damping are used for computing dynamic load amplification factor to determine the demands for serviceability limit state (SLS), ultimate limit state (ULS), and fatigue limit state (FLS). Fatigue damage typically happens in cross-wind direction (Damgaard, et al., 2013), where system damping is significant less than damping in along-wind direction. As the second largest damping component in along-wind system damping and the largest one in crosswind direction, foundation damping has a significant role in fatigue analysis.

Long-term dynamic performance is also a major challenge since the system likely experiences variation in soil stiffness due to impact of cyclic loading and the development of global and/or local scour due to current and wave activities. These changes should be anticipated to ensure the structure is safe over its lifespan.

Hybrid system concept can be deployed in newly developed and existing offshore wind farms. Its configurations with additional wave and/or tidal energy devices change dynamic properties and loading pattern of the monopile-supported structure. Improving reliability of natural frequency and foundation damping evaluations for monopile-supported wind turbines and hybrid structures is crucial for viability of the hybrid system.

This study, hereby, will focus on developing approaches to effectively and reliably estimate natural frequency of offshore wind turbines and hybrid systems supported by monopile foundation.

1.2. Scope of work

To investigate dynamic performance of monopile-supported wind turbines and hybrid system, following tasks are performed:

- Literature review on numerical simulation of lateral loaded pile in sandy ground under static, dynamic, and cyclic load.
- Critical review on loading history of sand and its impact on input of numerical simulation of pile subjected to lateral load. Correlation between soil relative density (D_R), CPT tip resistance (q_c), soil overconsoliation ratio (OCR) and maximum shear stress (G_o)
- Investigation on influences of soil relative density, pile diameter and length, and depth of local scour on natural frequency of the monopile wind turbine and soil damping.
- Establishing correlation between pile deformations at mudline level and vibration characteristics
- Evaluation of effects of local scour on natural frequency and foundation damping
- Evaluation of natural frequency and foundation damping of hybrid system

1.3. Dissertation layout

The dissertation is organized in form of three papers. Paper 1 is focused on role of sandy ground stress history in numerical simulation laterally loaded pile. By simulating pile tests for PISA project, the paper shows how consideration of K_0 and OCR of existing ground

can improve accuracy of the simulations and allay effect of pile installation on pile performance. Impact of soil stress history on simulation input, soil constitutive model, and outcomes on load-displacement response, and soil reactions on the pile.

Paper 2 is aimed to investigate influences of soil condition and monopole configurations on offshore wind turbine natural frequency and foundation damping ratio. Numerical dynamic analyses are performed for numerous wind turbine structures with different soil relative densities, pile diameter, and pile embedment.

Paper 3 focuses on establishing correlations between pile deformations at seabed level and dynamic properties of the system. The correlations are developed based on outcomes of the parametric study in Paper 2. Derived relationships are used to estimate natural frequency of two existing monopole wind turbines with available frequency measurements and check with other numerical simulation of wind turbines with local scour and hybrid systems

A summary of the conclusions and contributions of this study and recommendation for future research is placed at the end of this dissertation.

CHAPTER 2: ROLES OF SOIL STRESS HISTORY IN RESPONSE OF LATERALLY LOADED PILE EMBBBED IN SAND.

Abstract

This study explores the possibility of inclusion of soil stress history into numerical simulation to improve accuracy of the analyses of the test piles under lateral load. Soil loading history parameters, OCR and K_0 are determined by existing OCR-K_0 relationship and empirical correlations with CPT tip resistance, q_c. OCR and K_0 influence initial stress condition, G_0 in soil domain and constitutive stress-strain response of soil elements. Two correction factors for effective stress and OCR are proposed for G_0-q_c relationship by Baldi, et al. (1989). Simulations with OCR and K_0 in soil descriptions yield more accurate estimations on load-displacement responses of piles, especially in small displacement region. OCR, or preconsolidation pressure, appears to have major impact on pile performance. Soil reactions are integrated from stresses on interface elements for analyses with and without OCR. Obtained results suggest that distributed moment along pile length and pile base shear have significant contributions to resisting moment (from 22% to 37% in total) and play a more important role in analysis not including OCR. P-y curves generated from numerical outcomes are compared with API recommended relationships. Impacts of positive and negative wall friction angle on ultimate soil reaction, which are omitted in API p-y curves, are discussed. The study also raises a question regarding effect on shear vibration on soil OCR and K_0 of sand.

2.1. Introduction

Understanding site loading history and its effect on soil behavior is important in assessing the behavior of several geotechnical infrastructure. Soil stress history, which is characterized by overconsolidation ratio (OCR) and/or at-rest horizontal stress ratio (K_0), is an aspect that requires further investigation, especially with respect to analyzing laterally loaded pile. The inclusion of stress history in analyses of laterally loaded piles necessitates the definition of past geologic loading as well as the effect of pile installation. While the latter is typically neglected in analyses due to complexity of the various installation measures, the former is insufficiently examined and employed, especially for piles embedded in sandy soils, of which OCR and its correlation with K_0 are more difficult to define.

The American Petroleum Institute (API) p-y curves approach is commonly used in design of piles subjected to lateral load. The static and cyclic p-y relationships for piles embedded in sand were initially developed based on data from field experiments at Mustang Island by Cox, et al. (1974) and formulation by Reese, et al. (1974). The approach was further improved by Murchison and O'Neill (1984). Two fundamental parameters for the development of p-y curves with depth are ultimate soil reaction (p_u) and soil horizontal coefficient of subgrade reaction (k_h). In the original development of the p-y process, the effect of stress history was implicitly included in process of determining p_u and k_h as follows:

- Calibrated k_h for soil is found to be 2.5 times higher than the value recommended for laterally loaded pile by Terzaghi (1955). The reason could be related to the ratio of unloading/reloading to virgin loading modulus. As described by Gavin and Lehane (2003) and Yang, et al. (2014), lateral stress at a point increases as pile is being driven or pushed down, and peaks when pile tip reaches its depth, but then decreases to a value that corresponds to pile stationary state. This phenomenon indicates that after pile driving, a soil mass surrounding the pile is overconsolidated; therefore, when the pile is being loaded laterally, resisting soil will initially experience reloading behavior, which will influence the value of calibrated k_h.
- The p_u is computed with assumption of K_0=0.4, which is close to value determined by Jaky's equation (1944) for normally consolidated sand with reported friction angle $\varphi=39^o$. However, in the currently used approach in practice (e.g., API RP 2A) the p_u must be adjusted by empirical factor A, which is defined as the ratio of measured ultimate resistance to computed value. For static loading, A_s is greater than 1 for depth of up to three times the pile diameter. In this zone, p_u is defined by limit equilibrium analysis using failed soil wedge free body bounded by assumed failure surfaces at shallow depth (Figure 1). K_0 is used in the computation of lateral force F_n and, therefore, governs value of shear resistant F_s on surface AED. Therefore, underestimation of K_0 could be a contributing factor for underestimating p_u.
- Additional details of Mustang Island tests are described in a book by Reese and Van Impe (2011), of which results of penetrometer testing were conducted before and after pile installation. Data indicate that surrounding soil is densified and there is

considerable increase in cone resistance in upper depth of five pile diameters due to pile driving. Ratio of cone resistance after compared to before pile installation. As shown in Figure 2.1, $Q_{c,1}/Q_{c,0}$, has similar distribution pattern to that of the coefficient A_s with depth. Coefficient A_s likely compensates for the lack of including pile installation effects and the underestimation of K_0. Meyer and Reese (1979) found that Reese, et al. (1974) approach overestimate significantly lateral deflection of driven piles embedded in heavily overconsolidated soil even when K_0 =1 is used.

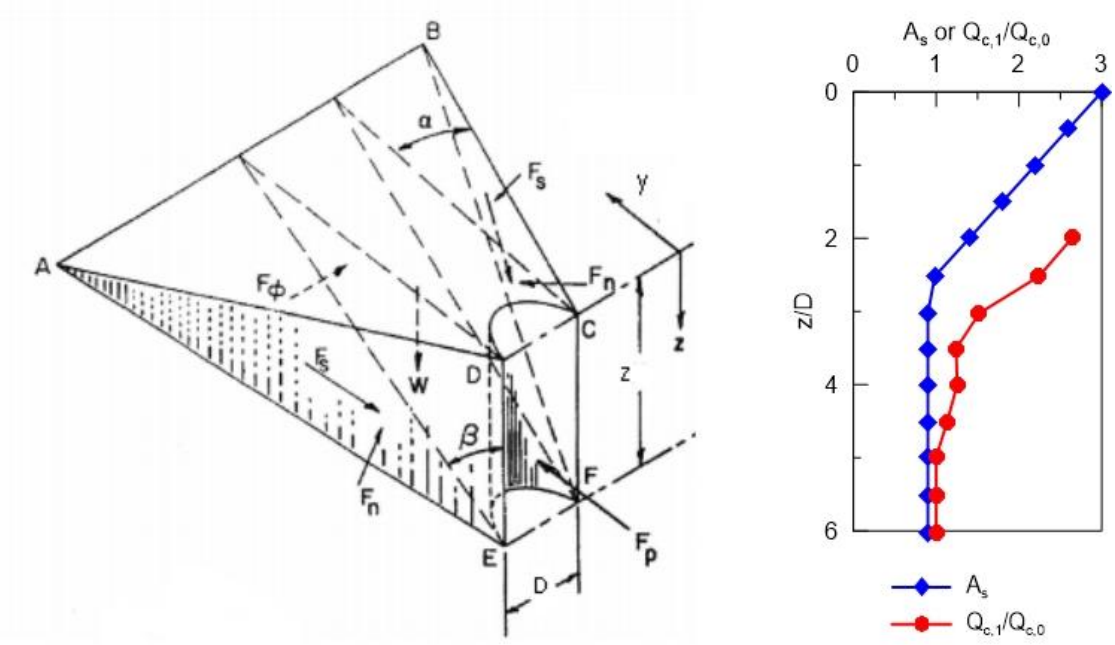

Figure 2.1. Soil wedge for determining p_u at shallow depth *(Reese, et al., 1974)* (left) and distributions of A_s (Reese, et al., 1974) and $Q_{c,1}/Q_{c0}$ (Reese and Van Impe, 2011).

Several numerical studies have included soil history components in the analyses and have shown its impacts on pile load-displacement response and p-y curves. Fan and Long (2005) compare p-y curves generated from 3D modeling and found that both initial stiffness and p_u increase with increasing values of K_0. Taborda, et al. (2019) performed two sets of simulations for pile tests of PISA projects and obtained better comparison with measured data from models using maximum shear modules, G_0, measured by seismic cone penetration test (SCPT) than the ones using G_0 derived from triaxial tests. Murphy, et al. (2018) uses empirical correlations with cone point resistance, q_c, to determine parameters, including OCR and K_0, for Hardening Soil (HS) constitutive model of Plaxis 3D. Murphy, et al. (2018)

obtained good agreement with experimental results. These findings suggest the potential use of in-situ soil investigation data to examine existing ground stress history for analyzing laterally loaded pile in sandy soils.

Assumption on soil OCR and K_0 has direct impact on numerical modeling procedure and its results. It controls the values of the soil parameters in model calibration. Furthermore, when the calibrated model is deployed for conditions that has significant difference in stress history, the accuracy of the simulation is not guaranteed. Work herein investigates how stress history affects response of pile subjected to lateral load and how to synthesize stress history of soil strata prior to pile installation to improve accuracy of predictive results.

2.2. Soil stress history indicators

Soil stress history is characterized by OCR. It is defined as ratio of the maximum vertical effective stress a soil element has experienced (σ'_p) to the current effective overburden stress (σ'_{vo}) acting on the element. Mayne and Kulhawy (1982) indicates a direct relation between OCR and K_0 and, therefore, K_0 can be used as an indication of soil stress history. The definition of OCR and K_0 during unloading by Mayne and Kulhawy (1982) is expressed as follows:

$$OCR = \frac{\sigma'_p}{\sigma'_{vo}} \qquad (2\text{-}1)$$

$$K_{0,OC} = (1-\sin\phi')OCR^{\sin\phi'} \qquad (2\text{-}2)$$

According to Mitchell and Soga (2005), there are different paths to reach a given stress- void ratio state of a soil element (Figure 2.2). It could be through conventional means of loading and unloading (path **a-b-c**) or via direct path **a-c**, for example due to creep. For sand, path **a-c** is likely to occur under impact of vibrations that cause rearrangement of soil particles. However, it is unclear if the OCR and K_0 of soil experiencing path **a-c** are identical to those of **a-b-c**.

Sand volume change is more sensitive to shear than longitudinal vibration. Studies on vibratory compaction of sand show that sand densification is unnoticeable when vibration acceleration is well below 1g or dynamic stress initial is lesser than 20% of soil overburden

pressure (D'Appolonia and D'Appolonia, 1967, D'Appolonia, 1970, Whitman and Ortigosa, 1969). Shear vibration, on the other hand, cause appreciable volume change as shear strain exceeds 0.01% (Youd, 1972). The rate of densification is greater with increasing magnitude of cyclic shear strain applied on testing specimen; however, insignificant difference is reported for the magnitude of larger than 0.05% (Silver and Seed, 1971, Youd, 1972). Volume change is found inversely proportional to sand relative density and confining pressure (Silver and Seed, 1971) and independent of shear vibration frequency (Youd, 1972)

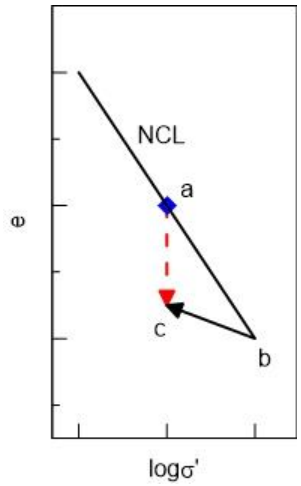

Figure 2.2. Paths to soil current e-σ state (Mitchell and Soga, 2005)

Undergoing path **a-c** due to vertical vibration leads to changes in K_0 and OCR in soil. For normally consolidated sands, Vardhanabhuti and Mesri (2007) reveal that vertical vibration significantly decrease soil sample void ratio and increase K_0 . As shown in Figure 2.3, vertical vibration applied at vertical stress of 50kPa decreases void ratio of a sample from 0.82 to stabilized value of 0.78 and increases K_0 from about 0.447 to 0.6. Subsequent loading in oedometer test shows decrease in K_0 to the before-vibration value at 125 kPa, which means the presconsolidation pressure is raised from 50kPa to 125 kPa by the vibration. However, the relation between increased K_0 and OCR with cyclic stress magnitude and duration are not established. Likewise, impact of shear vibration on loading history parameters have not been studied.

Definition of stress history of sand, therefore, is not so apparent. Stress history of sand is hard to be examined by lab test due to the challenge of having sand samples without

disturbance and it is normally determined by in-situ tests, including CPT and flat dilatometer test (DMT). However, in-situ test correlations for K_0 and OCR have been developed by vertical-stress-based approach (path **a-b-c**). Since dense sand and over consolidated (OC) clay are dilatant under shear, packing of sand particles, or relative density D_R, might be an indication of OC state for either path of stress versus soil volume change. Nevertheless, it is not within the scope of this paper. The analyses in this study are performed with assumption that the relation expressed by equation 2-2 is valid.

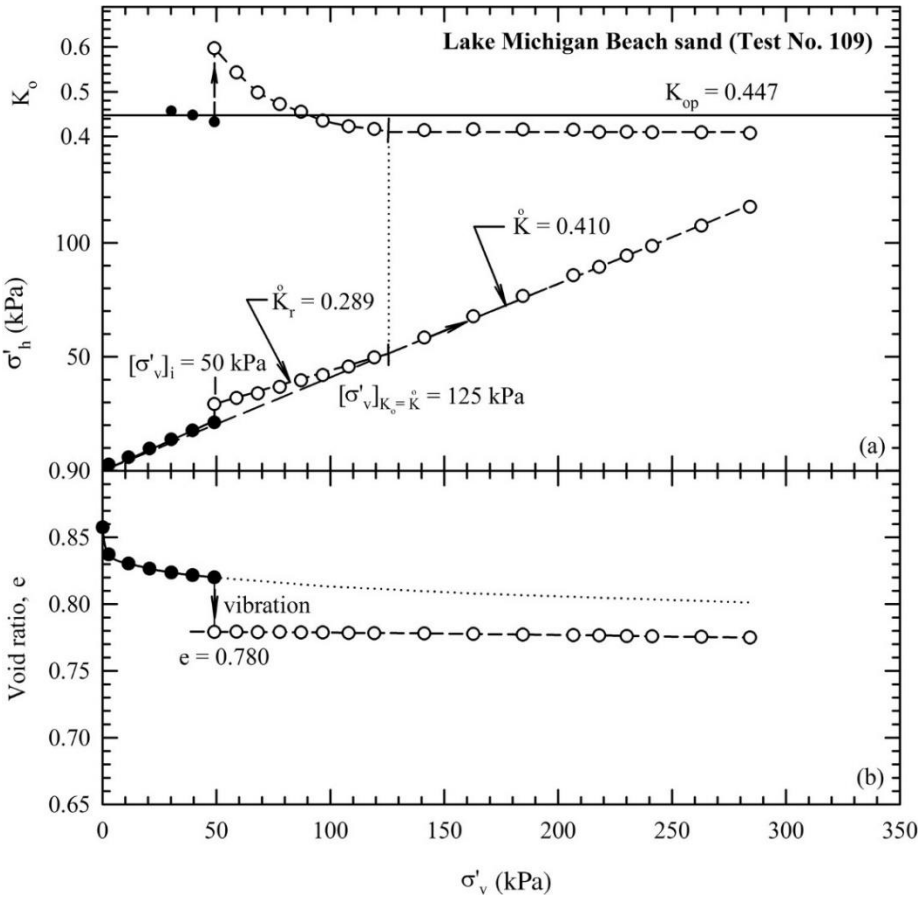

Figure 2.3. Effect of vibration on soil void ratio and K_0 (Vardhanabhuti and Mesri, 2007)

2.3. CPT-based soil stress history parameters

Sandy soil classification and engineering parameters can be determined by empirical correlations with CPT-measured point resistance q_c. Sand relative density, D_R, friction angle, ϕ', and K_0 are correlated to q_c per equations 2-3 to 2-5 (Kulhawy and Mayne, 1990, Mayne, et al., 2001):

$$D_R = \sqrt{\frac{q_c / P_a}{305\left(\sigma'_{vo} / P_a\right)^{0.5}\left(OCR\right)^{0.18}}} \quad (2\text{-}3)$$

$$\phi' = 17.6 + 11\log\left(\frac{q_c / P_a}{(\sigma'_{vo} / P_a)^{0.5}}\right) \quad (2\text{-}4)$$

$$K_0 = 1.33\left(q_c\right)^{0.22}\left(\sigma'_{vo}\right)^{-0.31}\left(OCR\right)^{0.27} \quad \text{with } q_c \text{ in MPa and } \sigma'_{vo} \text{ in kPa} \quad (2\text{-}5)$$

where: P_a=100 kPa is atmospheric pressure. With the assumption of that OCR – K_0 relationship by equation 2-2 is applicable, OCR can be correlated to q_c by combining equations 2-2 and 2-5 as in equations 2-6 and 2-7

$$1.33\left(q_c\right)^{0.22}\left(\sigma'_{vo}\right)^{-0.31}\left(OCR\right)^{0.27} = (1-\sin\phi')\left(OCR\right)^{\sin\phi'} \quad (2\text{-}6) \text{ or}$$

$$OCR = \left[\frac{1.33(q_c)^{0.22}}{(1-\sin\phi')(\sigma'_{vo})^{0.31}}\right]^{\frac{1}{\sin\phi'-0.27}} \quad (2\text{-}7)$$

When the q_c data are not available but the soil unit weight and D_R are, alternative correlation between q_c and D_R can be used to generate q_c profile, e.g. by using the data by Lunne and Christoffersen (1983) or by Jamiolkowsky, et al. (1985). The latter describes the relation between cone resistance in field condition and soil D_R as in equation 2-8.

$$q_c = \left(1 + \frac{D_R - 30}{100}\right)\left(P_a\sigma'_{vo}\right)^{0.5} 10^{(D_R/68+1)}, \text{ with } D_R \text{ in percent} \quad (2\text{-}8)$$

DMT horizontal stress index, K_D, is sensitive to soil stress history (Marchetti, 2010). For sites that have both CPT and DMT data available, Baldi, et al. (1986) offer an alternative correlation of K_0 to q_c and K_D in equation 2-9.

$$K_0 = 0.376 + 0.095K_D - 0.0046q_c / \sigma'_{vo} \quad (2\text{-}9)$$

2.4. Impact of OCR on G_0

Soil small strain maximum shear modulus is dependent of soil void ratio, OCR and confining stress on soil element. Hardin and Richart Jr (1963) report that longitudinal and shear waves propagate faster through granular soil samples conditioned with lower void ratio and larger confining pressure. Hardin and Black (1966, 1968) proposed expressions for G_0 in

sand and clay in similar form as in equation 2-10. OCR is reported to have insignificant impact on G_o of sand in studies by Hardin and Black (1966) and Zdravković, et al. (2019). However, Baldi, et al. (1989) establish q_c-G_0 relationships for quartz sand with noticeable difference in G_o at OCR=1 and OCR=10 (Figure 2.4).

$$G_o = AP_a \left(OCR\right)^m \left(\sigma'_m / P_a\right)^n f(e) \qquad (2\text{-}10)$$

where: A, m and n coefficients determined by curve fitting and n=0.5 is typically assumed; σ'_m is mean effective stress and f(e) is a function representing influence of void ratio.

The discrepancy in effect of OCR, in mentioned studies, is likely due to the different approaches used to induce the over consolidation state. Hardin and Black (1966) and Zdravković, et al. (2019) use isotropic loading and unloading of triaxial testing while Baldi, et al. (1989), with chamber tests, vary only vertical pressure (as in consolidation test). The latter approach leads to more volume change under same increase in stress on the same soil sample.

Jardine, et al. (2005) describe Baldi, et al. (1989) q_c-G_o relation by equation 2-11. However, the equation only reflects well the curve for σ'_{vo}=300kPa and OCR=1. Therefore, modifiers are introduced herein to the q_c-G_o correlation for computing G_o at other values of overburden stress and OCR. Modified q_c-G_o correlation combining above correction factors is written as in equation 2-15.

$$G_o = q_c \left[0.0203 + 0.00125\eta + \left(1.216E-6\right)\eta^2\right]^{-1} \qquad (2\text{-}11)$$

$$\text{where } \eta = \frac{q_c}{\left(P_a \sigma'_{vo}\right)^{0.5}} \qquad (2\text{-}12)$$

- *OCR correction factor, F_{OCR}:* Baldi, et al. (1989) reports that as OCR increases from 1 to 10, G_o rises by about 15% at both $\sigma'_{vo} = 50$ kPa and 300kPa. Assuming this rule is valid for OCR increasing from 10 to 100, OCR correction factor is proposed in form of equation 2-13.

$$F_{OCR} = 1 + 0.16 \log OCR \qquad (2\text{-}13)$$

- *Effective stress correction factor, F_σ:* Baldi, et al. (1989) data also indicates that G_o increases by about 15% at OCR =1 and 10 when σ'_{vo} decreases from 300kPa to 50kPa. Since modulus exponential number n=0.5, the proposed effective stress correction factor expressed as in equation 2-14 is implemented into equation 2-11 assuming same increment rate in G_o happens for every 1/6-fold decrease in effective stress outside the studied range.

$$F_\sigma = \left(\sqrt{300/\sigma'_{vo}}\right)^{0.156} = \left(300/\sigma'_{vo}\right)^{0.078} \qquad (2\text{-}14)$$

$$G_{o,OCR} = \left(1 + 0.16 \log OCR\right)\left(\frac{300}{\sigma'_{vo}}\right)^{0.078}\left\{\frac{q_c}{0.0203 + 0.00125\eta + \left(1.216E-6\right)\eta^2}\right\} \qquad (2\text{-}15)$$

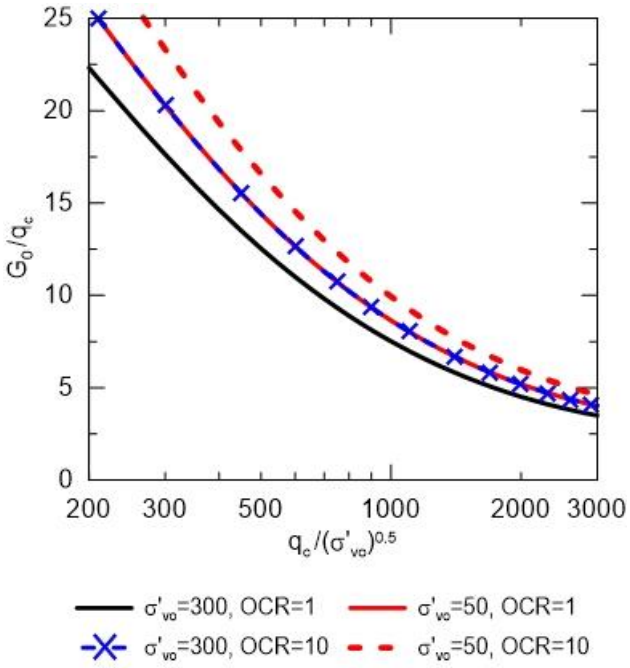

Figure 2.4. q_c-based correlations for G_o by Baldi, et al. (1989) redrawn using equation 2-15

2.5. Soil reaction induced by laterally loaded pile.

Stresses in soil surrounding pile change as the pile is displaced by lateral load. On the surface along pile length, the stresses can be categorized as effective normal stress, $\sigma'_n(z,\theta)$,

vertical shear stress, $\tau_1(z,\theta)$, and tangential shear stress, $\tau_2(z,\theta)$ while at pile base there are effective normal stress, $\sigma'_{n,b}$, and shear stress, $\tau_{h,b}$ (Figure 2.5). Integrations of the stresses over pile perimeter yield values distributed soil lateral force p(z) and distributed moment m(z) along pile length. Resultant of shear stress on pile base area is base share, H_b, and normal stress on the base induces a resisting moment, M_b. These four components - p(z), m(z), H_b and M_b - are soil reactions acting on embedded pile in 1D analyses (Byrne, et al., 2015, Davidson, 1982, Zdravković, et al., 2019)

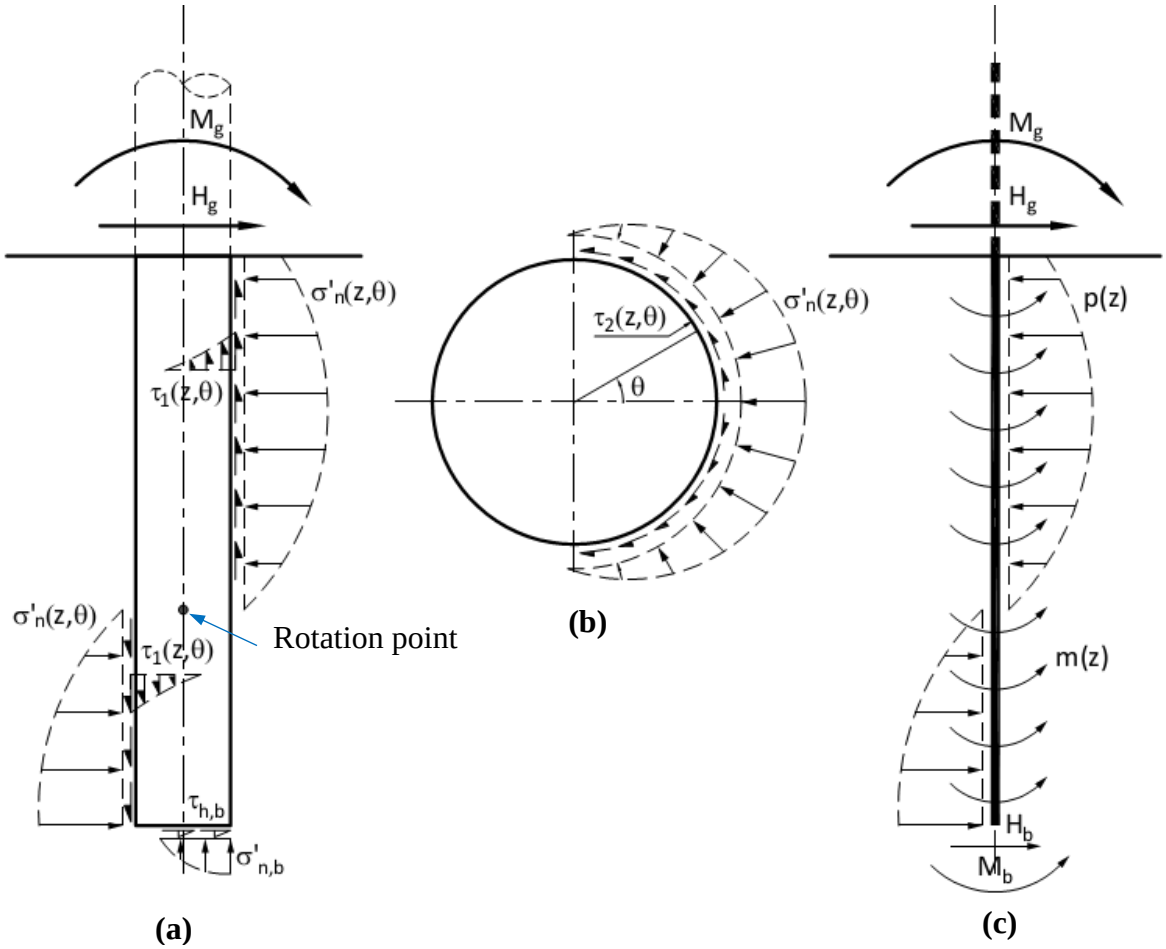

Figure 2.5. Pile-soil interface stresses and reactions (after Davidson (1982) and Zdravković, et al. (2019)): distributions of stresses along pile length (a), and on pile cross-section (b), and soil reactions on pile modeled as a beam in 1D analysis (c)

Pile rigidity might affect importance and thus implementation of soil reaction components. For long flexible pile, most of soil resistance in provided by p(z); however, for

short rigid pile contributions of other factors are significant (Byrne, et al., 2015, Davidson, 1982). (Byrne, et al., 2015) suggest that for piles with embedded-length-to-diameter ratio $L/D \geq 10$ m(z), H_b and M_b can be neglected. Soil reaction components are computed from generated soil stresses by equations from 2-16 to 2-19 (Davidson, 1982):

$$p(z) = \int_0^{2\pi} \left[\sigma_n'(z,\theta) \cdot \cos\theta + \tau_2(z,\theta) \cdot \sin\theta \right] (D/2)\, d\theta \qquad (2\text{-}16)$$

$$m(z) = \int_0^{2\pi} \tau_1(z,\theta) \cos\theta (D/2)^2\, d\theta \qquad (2\text{-}17)$$

$$H_b = \int_0^{D/2} \int_0^{2\pi} \tau_{h,b} (D/2)\, d\theta dr \qquad (2\text{-}18)$$

$$M_b = \int_0^{D/2} \int_0^{2\pi} \sigma_{n,b}' \cos\theta (D/2)^2\, d\theta dr \qquad (2\text{-}19)$$

2.6. American Petroleum Institute (API) p-y curves for sand

API p-y curves are widely used in engineering practice for analyzing laterally loaded piles. The relationship between soil lateral reaction per unit length, p, and pile displacement, y, at given depth, z, caused by static lateral load acting on pile embedded in sand was developed by Reese, et al. (1974) and Murchison and O'Neill (1984) in following form:

$$p = A_s p_u \tanh\left(\frac{k_h z}{A_s p_u} y \right) \qquad (2\text{-}20)$$

where:

- k_h is lateral modulus of subgrade reaction,
- A_s is empirical modification factor p_u:

$$A_s = \max\{0.9, 3 - 0.8z/D\} \qquad (2\text{-}21)$$

- $p_u = \min\{p_{u1}, p_{u2}\}$ is ultimate soil resistance, where p_{u1} is computed at shallow depth with soil wedge free body (Figure 2.1) while p_{u2} is for depth well below ground surface with soil horizontally flowing failure mechanism. With the value of $\alpha = \phi'/2$

and $\beta=45^o+\phi'/2$ for the soil wedge and the same β for angle of failure planes of flowing blocks, p_{u1} and p_{u2} defined by Reese, et al. (1974) can be rewritten as in equations 2-22 and 2-23 (Zhang, et al., 2005).

$$p_{u1} = \gamma z\left[D\left(K_p - K_a\right) + z\left(K_p - K_0\right)\sqrt{K_p}\tan(\frac{\phi'}{2}) + zK_0\sqrt{K_p}\left(\frac{1}{\cos(\phi'/2)} + 1\right)\tan(\phi')\sin(45^o + \frac{\pi}{2})\right] \quad (2\text{-}22)$$

$$p_{u2} = \gamma zD\left(K_p^3 + K_0K_p^2\tan\phi' - K_a\right) \quad (2\text{-}23)$$

where: K_0=0.4, $K_a = \tan^2\left(45^o - \phi'/2\right)$ and $K_p = \tan^2\left(45^o + \phi'/2\right)$ are at-rest, active and passive earth pressure coefficients, respectively.

It is noteworthy that originally k_h was selected based on soil relative density and ϕ' was determined by triaxial tests (Reese, et al., 1974). Meyer and Reese (1979) used correlations between SPT N-value and D_R and ϕ' to develop the chart for selecting k_h from either D_R or ϕ' that has been adopted in Murchison and O'Neill (1984) and API recommendations. Reese and Van Impe (2011) still recommend using triaxial ϕ' for API p-y curves.

Effect of soil stress history parameters on test piles deflection and induced soil reactions on the pile are examined in this study. Plaxis 3D finite element package is employed to perform numerical simulation of the piles subjected to lateral load, with Hardening Soil with small strain modulus (HSsmall) constitutive model for surrounding soil. Soil model properties, OCR and K_0 are determined by correlation with CPT tip resistance q_c. The analyses are performed with soil description including and excluding soil OCR and K_0 that effect on initial stress condition, soil maximum shear modulus and eventually on the overall performance of the pile under lateral load and individual components of soil reactions resisting to that load. Contributions of the soil reactions will be examined, including a comparison of the comparison of p-y curves obtained from the simulations and API recommendations.

2.7. Input for numerical simulations

The simulations in this study are performed for pile experiments in marine sand at Dunkirk in northern France. The pile tests are part of the PISA Joint Industry Research Project, which has the aim of improving design methodology for offshore monopile foundations for wind turbines.

2.7.1. Test site

The test site consists of upper 3m of very dense hydraulic filling sand placed in 1970s and natural marine sand deposit (Chow, 1996, Zdravković, et al., 2019). Chow (1996) assessed soil investigation data, including CPT and DMT, and concluded that the sand fill and the marine deposit had D_R =100% and D_R=75%, respectively. The author also reports soil moist and saturated unit weight of 17.1 kN/m^3 and 19.9 kN/m^3, respectively, and ground water table (GWT) at depth = 4m. Using equation 2-8, a q_c profile is generated based on ground descriptions by Chow (1996) and it confirms the relative densities suggested by the author (Figure 2.6 and Figure 2.9a).

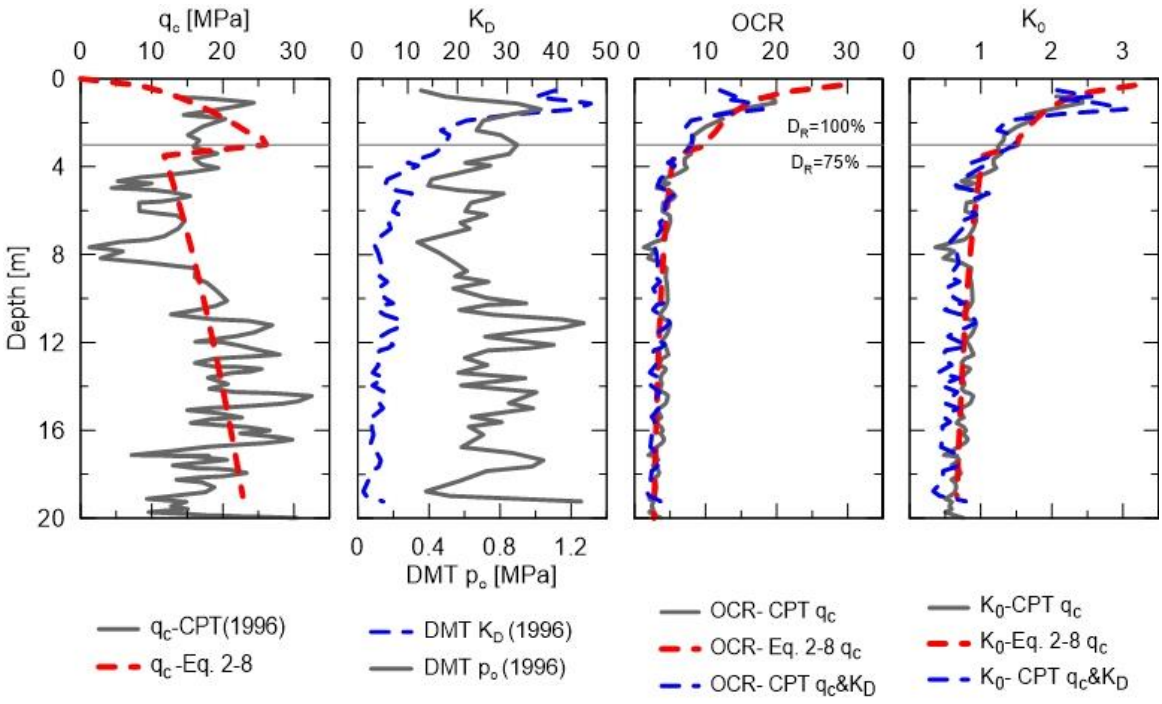

Figure 2.6. Comparison of q_c reported by Chow (1996) and by Eq. 2-8, and of OCR and K_0 computed from in-situ tests data and from generated q_c profile based on Eq. 2-8

The PISA test site is about 100m away from location described by Chow (1996).

Zdravković, et al. (2019) performed a new investigation program. The authors found ground water table at deeper depth of 5.4m and adopted relative density values reported by Chow (1996) for the soil layers despite of that the assessment of CPT data offered the possibility of the marine sand deposit having denser packing .

The G_o profiles reported by Chow (1996) and Zdravković, et al. (2019) show that the 1996 site has significant lower G_o in depth from 3 to 10m (Figure 2.7). Therefore, in conjunction with Zdravković, et al. (2019) CPT data, in this study the natural sand deposit is considered to be denser with D_R=86% and start from depth of 4.4m. Figure 2.8 and Figure 2.9b show good agreements in OCR, K_0 and G_o profiles computed from generated q_c and Zdravković, et al. (2019) CPT . Equation 2-15 appears to better describe $G_o - q_c$ relationship (Figure 2.9). Equation 2-11 likely captures the lower bound of G_o values obtained from measurements of shear wave velocity.

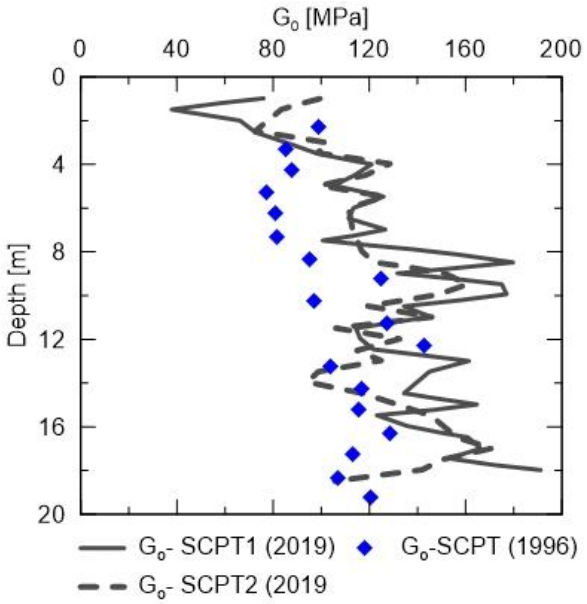

Figure 2.7. G_o profiles reported by Chow (1996) and Zdravković, et al. (2019)

2.7.2. Test piles

The experimental results used in simulations are selected pile tests from the PISA project at Dunkirk site (McAdam, et al., 2019). Test pile specifications, including pile diameter, D, embedded length, L, pile wall thickness, t, and cantilever arm from ground surface to applied lateral load, H, are listed in Table 2.1. The piles were installed by

vibration to depth of up to 1.5 m and subsequent hammer driving.

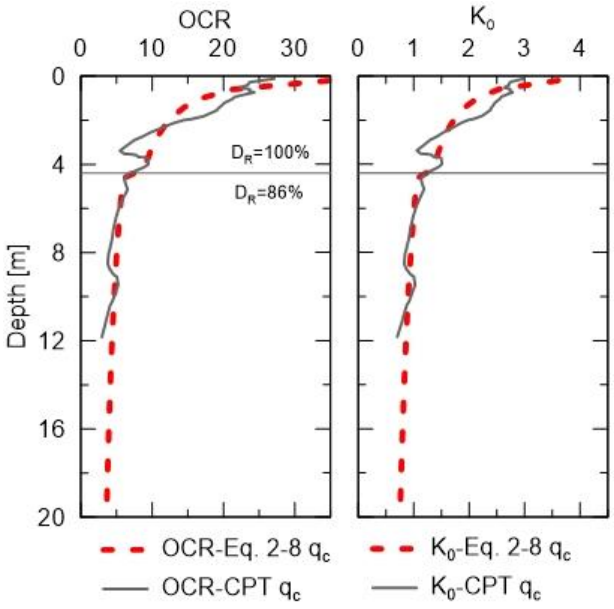

Figure 2.8. OCR and K_0 computed for q_c profiles generated by equation 2-8 and reported by Zdravković, et al. (2019)

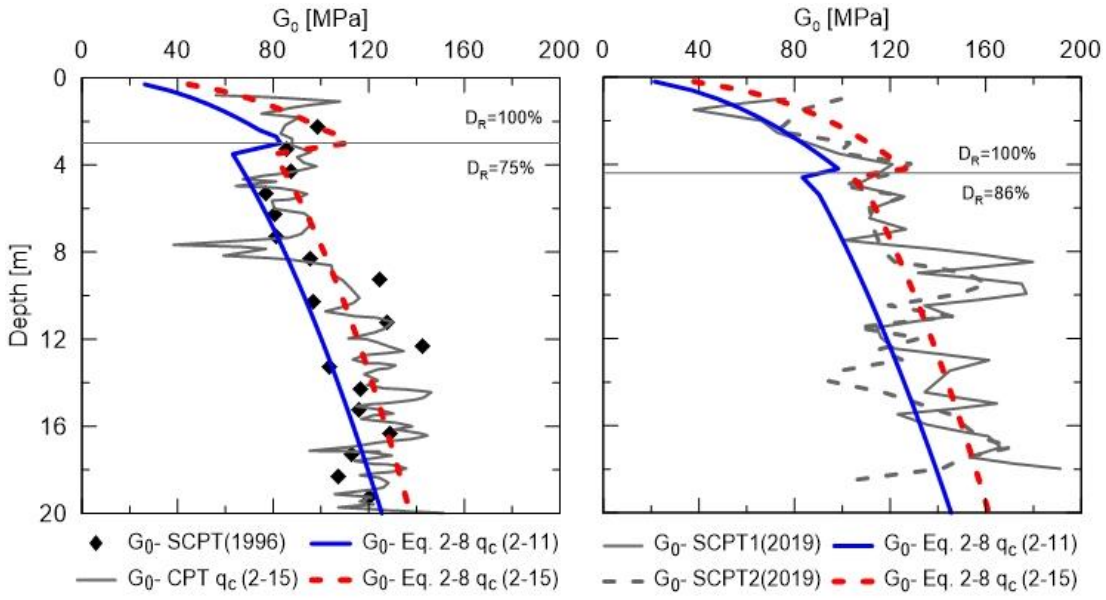

Figure 2.9. Comparison among G_o computed by equations 2-11 and 2-15 with actual or/and generated q_c profiles and field measurements by Chow (1996) (a) and in 2019 by Zdravković, et al. (2019) (b).

Table 2.1. Pile test specifications (McAdam, et al., 2019)

Pile	D (m)	L (m)	t (mm)	h (m)
DM7	0.762	2.24	10	10
DM4	0.762	3.98	14	9.98
DM3	0.762	6.02	25	10.06
DL2	2.0	10.61	38	9.90

2.8. Numerical simulation

Taborda, et al. (2019) performed two sets of 3D simulations of pile tests in PISA project. The main difference between two sets is that one used G_0 determined by triaxial test and the other used G_0 profile validated by 2019 SCPT measurements data by Zdravković, et al. (2019). The ground was assumed normally consolidated and a K_0=0.4 was adopted for all the simulations. Shear strength parameters at different void ratios were obtained from triaxial tests, of which constant volume friction angles $\phi'_{cv} = 32^o$ was reported. The results showed that the simulations with field-validated G_0 provided more accurate pile force-displacement response. However, the role of soil stress history was not explicitly examined in Taborda, et al. (2019).

In this study, Hardening Soil with small strain modulus (HSsmall) constitutive model of Plaxis 3D (Brinkgreve, et al., 2019a) is utilized to simulate the experiments. The soil model combines shear modulus degradation relationship at small strain and subsequent hyperbolic stress-strain response at larger strain. Model parameters comprise of soil moduli for small strain, virgin loading, unloading and reloading; therefore, it is possible to capture pile cyclic load-displacement response and damping. The soil domain is layered, and depending on assumptions regarding soil stress history, values of OCR, K_0 and G_o are computed at mid-depths and assigned to sublayers. OCR, K_0, G_0 and ϕ' are all evaluated by correlations with q_c generated by equation 2-8.

2.8.1. Shear modulus degradation curve in small strain region

Shear modulus degradation curve in HSsmall model follows Hardin and Drnevich (1972) relationship and subsequent modifications by Dos Santos and Correia

(2001). Secant (G_s) and tangent (G_t) shear moduli are described as functions of shear strain (γ) (equations 2-24 and 2-25) (Brinkgreve, et al., 2007, Brinkgreve, et al., 2019a):

$$G_s = \frac{G_o}{1 + 0.385\,|\gamma / \gamma_{0.7}|} \tag{2-24}$$

$$G_t = \frac{G_o}{\left(1 + 0.385\left|\gamma / \gamma_{0.7}\right|\right)^2} \tag{2-25}$$

where $\gamma_{0.7}$ is the shear strain at which G_s=0.722G_0. Brinkgreve, et al. (2010) reported that $\gamma_{0.7}$ ranges between $1x10^{-4}$ to $2x10^{-4}$ and can be correlated to D_R (expressed in decimal form) by equation 2-26.

$$\gamma_{0.7} = (2 - D_R) \cdot 10^{-4} \tag{2-26}$$

However, the small strain domain is bounded by the cut-off strain at $G_t = G_{ur}$, where G_{ur} is shear modulus corresponding to unloading/reloading modulus, E_{ur} (Figure 2.10). The G_o/G_{ur} ratio varies from 2.5 for stiff soil to 10 for soft soil (Brinkgreve, et al., 2007).

Beyond $\gamma_{cut-off}$, if soil element is still in reloading regime, the stress-strain response follows the modified segment of degradation curves (Figure 2.10) with $G_t = G_{ur}$ (equation 2-28). Once entering virgin loading, the stress-strain relation is in hyperbolic form described by Duncan and Chang (1970) with E_{ur} being the initial tangent stiffness. Secant modulus at 50% ultimate deviatoric stress, E_{50} can be computed by correlation with E_{ur}, and tangent modulus for primary loading, E_{oed} =0.8E_{50} (Brinkgreve, et al., 2019a). Whole stress-strain relationship will be defined once the ratios of G_{ur}^{ref} / G_0^{ref} and $E_{ur}^{ref} / E_{50}^{ref}$ are determined.

$$G_{ur} = \frac{E_{ur}}{2(1 + \nu_{ur})} \tag{2-27}$$

$$\gamma_{cut-off} = \frac{\gamma_{0.7}}{0.385}\left(\sqrt{\frac{G_o}{G_{ur}}} - 1\right) \tag{2-28}$$

where $\nu_{ur} = 0.2$ is Poisson's ratio chosen for unloading/reloading.

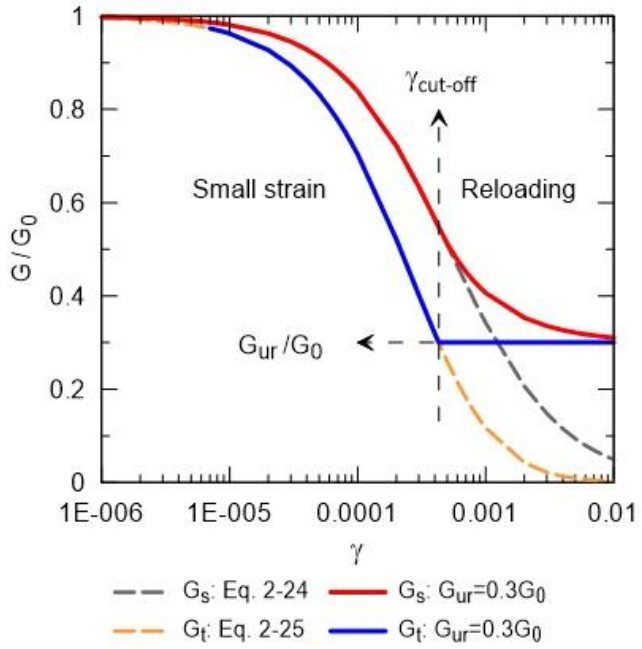

Figure 2.10. G degradation curves in HSsmall (Brinkgreve, et al., 2019a).

2.8.2. Soil modulus parameters for HSsmall model

Stress dependent soil moduli in HSsmall model are evaluated at reference confining stress $p'_{ref} = P_a = 100\text{kPa}$ (Brinkgreve, et al., 2019a). For sublayer *k*, average maximum shear modulus at reference stress is computed at mid-depth by equation 2-29.

$$G_{o,k}^{ref} = \frac{G_{o,k}}{\left(\frac{c \cdot \cos\phi' - \sigma'_3 \sin\phi'}{c \cdot \cos\phi' + P_a \sin\phi'} \right)^n} \qquad (2\text{-}29)$$

where $G_{o,k}$ is the maximum shear stress determined by equation 2-11 or 2-15, depending on assumption of OCR, or field measurements, $\sigma'_{z,k}$ and $\sigma'_{x,k}$ are vertical and horizontal geostatic stresses, c is soil cohesion, and n is pressure exponential number. For sand, n varies depending on confining pressure and soil relative density (Duncan, et al., 1980, Duncan and Chang, 1970, Wroth, 1979); however, n=0.5 is reported to well represent soil stiffness dependency on stress level (Janbu, 1963, Kelly, et al., 2006, Seed and Idriss, 1970, Wroth and Houlsby, 1985).

2.8.3. Shear strength parameters

Dilation angle is calculated as difference of friction angle ϕ' by correlation with q_c and ϕ_{cv} =32^o obtained in triaxial tests (Zdravković, et al., 2019). Triaxial tests also indicates that ϕ_{cv} is reached at axial strain of 35%; therefore, a dilation cap in term of void ratio is prescribed to ensure no dilation taking place beyond that strain. Since the soil investigation data and pile test description report the presences of negative pore water pressure of 13.5 kPa in soil above GWT (Zdravković, et al., 2019) and inter-facial gap between soil and pile wall (McAdam, et al., 2019), respectively, a cohesion c = 2kN/m^2 is assigned for all soil layers. The summary of soil parameters is presented in Table 2.2.

Table 2.2. Summary of soil model parameters

Layer	**1**	**2**
Thickness (m)	4.4	-
D_R (%)	100	86
$\gamma_{0.7}$	$\gamma_{0.7} = (2 - D_R) \cdot 10^{-4}$	
G_{ur}^{ref} / G_0^{ref}	0.3 (from model calibration)	
$E_{ur}^{ref} / E_{50}^{ref}$	4.0 (from model calibration)	
ϕ' (^{o})	45.8	43.5
ψ (^{o})	13.8	11.5

2.8.4. Soil history assumptions and 3D model

To examine how assumption on soil stress history affects outcomes of numerical modeling of lateral loaded piles, the simulations are performed in four settings (Table 2.3). Model calibration will start with full assessment of soil stress history (Case 1). It is aimed to determine $\gamma_{0.7}$ and the ratios of G_{ur}^{ref} / G_o^{ref} and $E_{ur}^{ref} / E_{50}^{ref}$ that induce the responses agreeing with pile experiments. Subsequently, impacts of OCR and K_0 are examined respectively by setting OCR=1 in Case 2, and OCR=1 and K_0=0.4 in Case 3. The G_o profiles in Case 1, Case 2 and Case 3 are identical, computed by equation 2-15, and matched with G_o obtained from in-situ measurements of shear wave velocity. In case 4, soil is considered as normally consolidated (OCR=1 and K_0=0.4) and G_o is computed for NC soil by equation 2-11 (without

modification factors for OCR and effective stress) being the lower bound of the four. Values of $\gamma_{0.7}$ and the ratios of $G_{ur}^{ref} / G_{o}^{ref}$ and $E_{ur}^{ref} / E_{50}^{ref}$ determined for Case 1 are used in other cases.

Table 2.3. Computation cases

Assumption	Symbol	OCR	K_0	G_o
OC soil, with in-situ Go	Case 1	Eq. 2-7	Eq. 2-2	Field data or eq. 2-15 with OCR of Case 1
OC soil, with in-situ Go, but OCR =1	Case 2	1	Eq. 2-2	
NC soil, with in-situ Go	Case 3	1	0.4	
NC soil, without in-situ Go	Case 4	1	0.4	Eq. 2-11

The simulations will capture loading, unloading and reloading stages of the pile tests. Soil domain dimensions are selected as in Figure 12 avoid significant impact of boundary condition per recommendation by Wallace, et al. (2002) and Kim and Jeong (2011). Interface elements are prescribed between soil and pile surface along pile wall and under pile tip.

2.9. Analyzing results on impact of soil history

2.9.1. Model parameters for Case 1

Model modulus parameters for Case 1 are tabulated in Table 2.2. Numerical simulations generate overall load-displacement relationships in very good agreement with experimental data (Figure 2.12). The response is particularly better at the displacement up to D/20, where creep is less significant. Creep and slower rate of loading to avoid sudden collapse of piles at larger displacement (McAdam, et al., 2019) are the main reasons for difference in the response as the soil constitutive model is not formulated to capture these features. Overall and particularly in small displacement range, responses delivered by this numerical procedure are more accurate than results by Taborda, et al. (2019) simulations for the same piles. Accurate prediction of the response at low displacement indicates that the calibrated soil model is proper for performing 3D numerical dynamic analysis or generating p-y curves for 1D analyses of natural frequency of offshore monopile wind turbines.

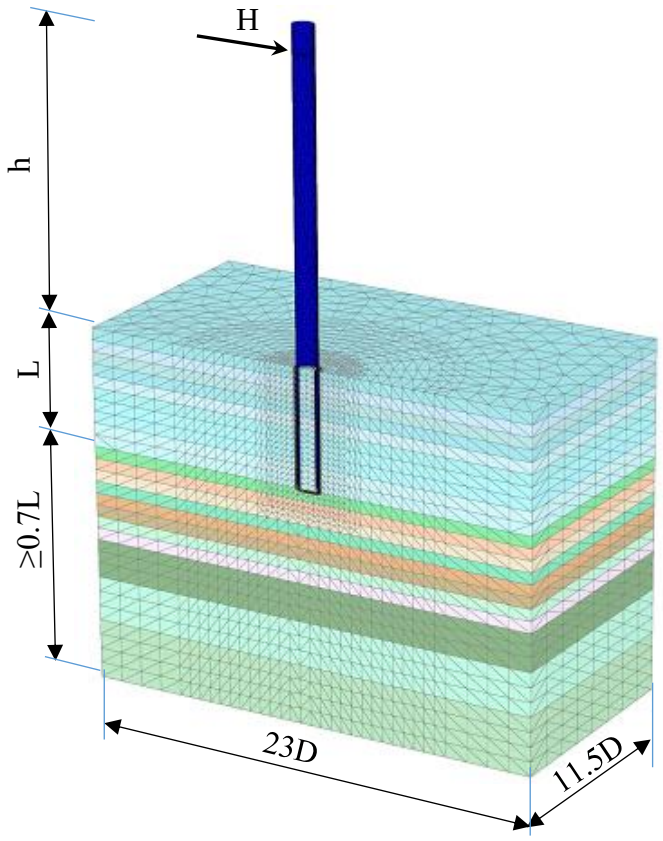

Figure 2.11. 3D finite element model used in analyses.

2.9.2. Influences of OCR

Pile load – ground line displacement responses plotted in Figure 2.12 describes effects of OCR and K_0. Influence of OCR is shown in difference of Case 1 and Case 2 and as OCR is reduced to 1, a softer response is obtained. Soil elements with OCR=1 will enter hyperbolic stress-strain relationship right after small-strain region, while ones with OCR>1 have additional reloading segment in between small strain and virgin loading until preconsolidation pressure is reached.

OCR also contributes to the difference between Case 3 and Case 4. G_o resulted from field measurements likely includes effect of soil loading history that is overlooked in laboratory experiments. Analyses without available in-situ G_o data and using equation 2-11 for q_c-G_o relationship (Case 4) have lowest modulus profile for input, as described in Figure 2.9, and thus yields largest pile displacement among the computational cases.

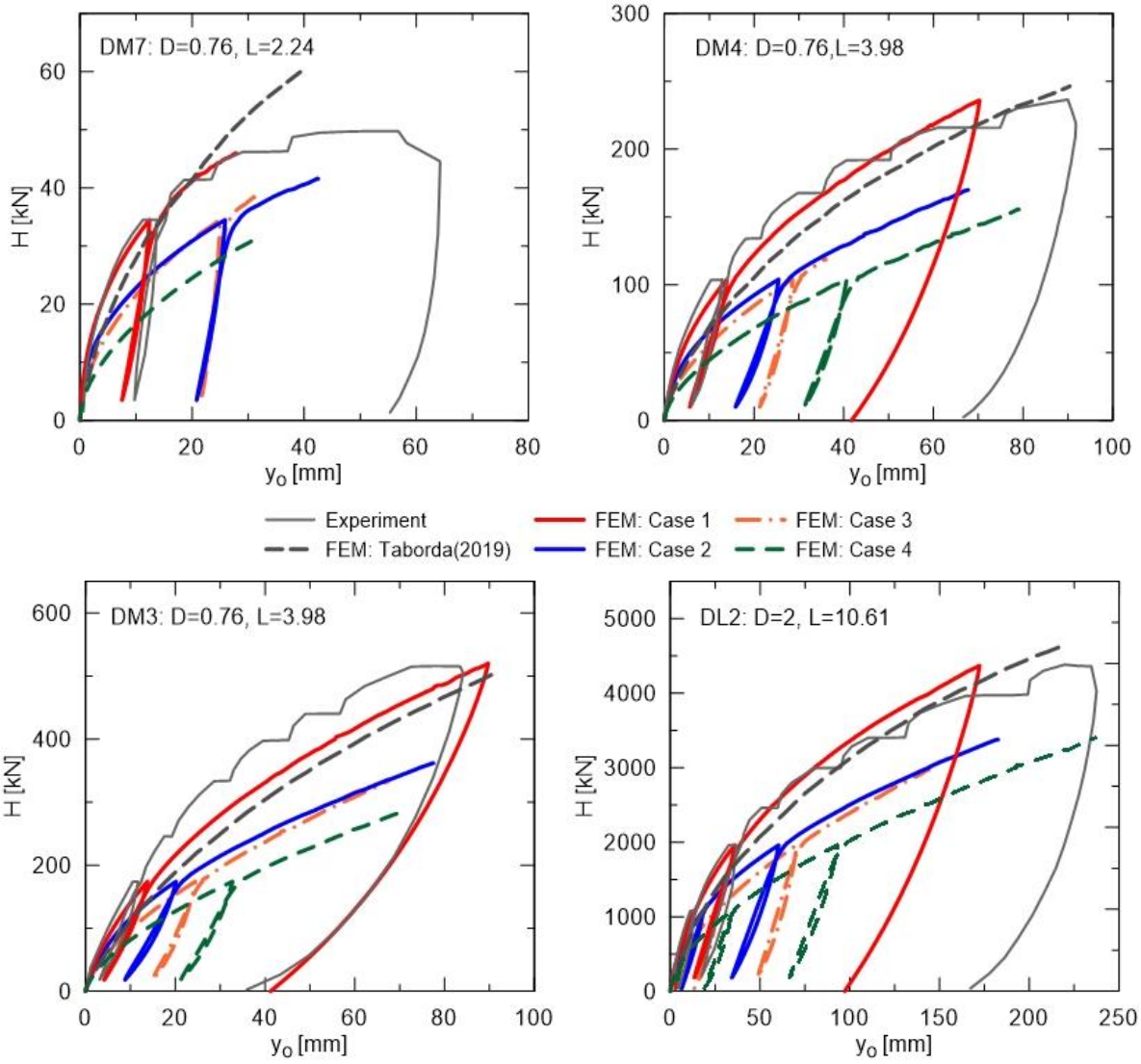

Figure 2.12. Comparisons of load-ground line displacement responses of test piles DM7, DM4, DM3 and DL1 by FE simulations for Cases 1, 2, 3, and 4 listed in Table 2.3 and Taborda, et al. (2019) outcomes

2.9.3. Influences of K_0

Responses of Case 2 and Case 3 are nearly identical despite of difference in K_0 assumption. However, it is the expectation and the evidence of the reliability of soil constitutive model and the simulations. The disparity in K_0 leads to different σ'_3 profiles and it has been addressed by separate computing of input values of reference maximum shear modulus G_o^{ref} (Equation 2-29) for the cases (Figure 2.13). As long as values of K_0 and G_o^{ref}

are assigned correctly correspondingly to the assumption on K_0 for soil layers in the model, G_o values at depths in two cases are identical after initial K_0-condition stress state of soil domain is analyzed thanks to stress-dependent rule adopted for modulus in the soil constitutive model. Change in K_0, therefore, has less significant impact than change in OCR from overconsolidated to normally consolidated state.

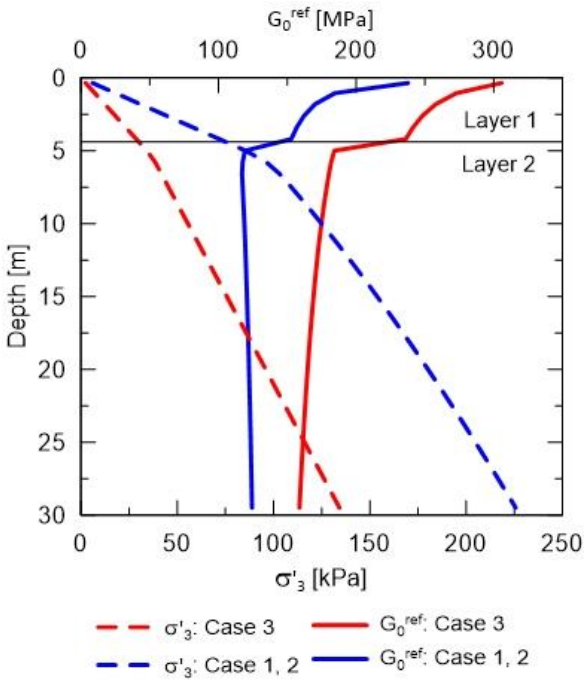

Figure 2.13. Differences in K_0 and G_o^{ref} between Cases 1, 2 and Case 3

2.9.4. Influences of pile installation.

Effect of pile driving is likely reflected in accuracy level of the simulations. Numerical estimations are better with piles with lower ratio of L/D and higher ratio of D/t. Simulation of DM3 with L/D=8 and D/t=30 has least accurate results, bettered by DM4 and DL2 with L/D=5.25 and D/t$\approx$53 and DM7 with L/D=3 and D/t=76. L/D and D/t are factors affecting level of soil plugging at open-ended pile tip during pile installation, which in turn contributes to magnitude of lateral stress along pile wall and in surrounding soil during and after pile installation (Gavin and Lehane, 2003, Ko and Jeong, 2014, Paik and Salgado, 2004). Since OCR has larger impact on simulation results than K_0, the determining value of maximum stress during pile driving is more important than stabilized value of pile in subsequent stationary state. Pile DM3 installation likely induces a stress history that has

significant larger OCR than values used for the simulations.

Impact of pile installation on soil layers is discovered by comparison of displacement profiles by experiments and simulations (Figure 2.14). Good matching of DL2 results in both layers 1 and 2 indicates installation effect is well covered by assessing OCR of existing ground. For DM2, effect of pile installation in layer 2 is greater, reflecting in relative difference between experimental and modeling results. It results from including but not limited to further soil densification and higher degree of soil plugging while pile penetrating 2nd layer that leads to larger discrepancy in OCR values in simulation and in-field.

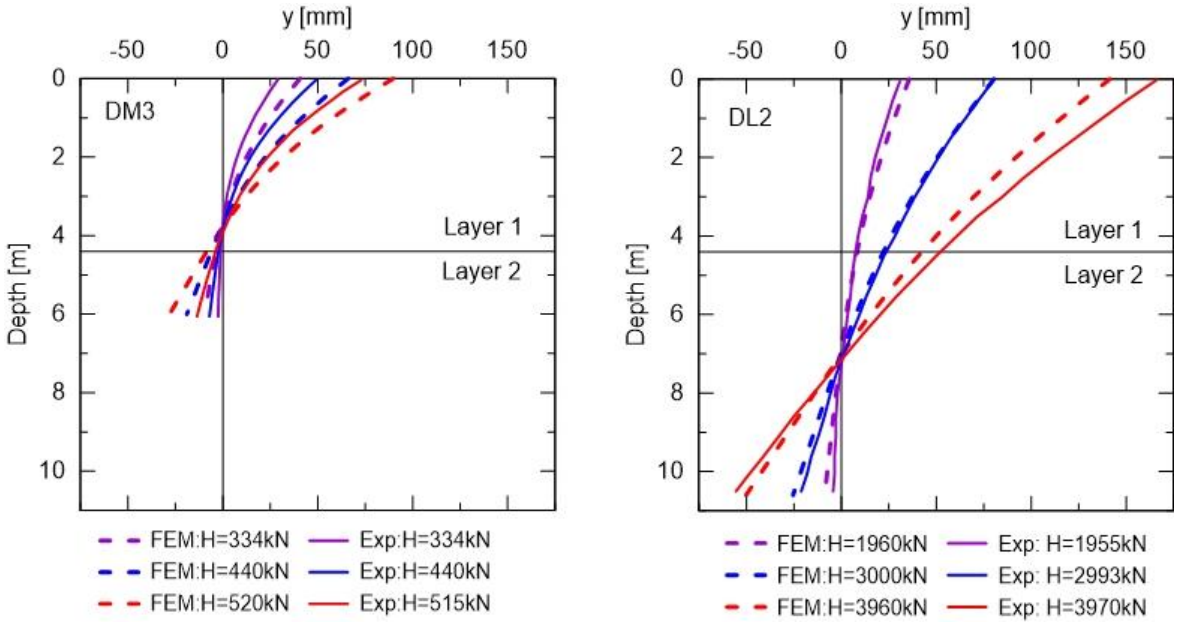

Figure 2.14. Displacement profiles obtained from experimental data and numerical simulations for DM3 (left) and DL2 (right) at various load values.

2.10. Soil reactions generated from 3D models.

Influence of OCR on soil reactions – p(z), m(z), H_b, M_b – on pile DL2 is investigated. The reactions are generated by integrating stresses on soil-pile interface elements. Discretization of interface elements along pile length and at pile tip are illustrated in Figure 2.15. Every triangular element has 6 stress points and there are 3 stresses, a normal and 2 shear stresses, at each point. The total value of force, F, caused by stress, f, on element *k* is as follows (Brinkgreve, et al., 2019b):

$$F = \sum_{i=1}^{6} f_i w_i A \qquad (2\text{-}30)$$

where:

- A – area of the element,
- f_i – value of stress f at stress point *i*,
- w_i – weighted factor accounting to distributed area of stress point *i*. For triangular element with 6 stress points (Figure 2.15b), w =0.109952 for points 1, 2 and 3, and w=0.223382 for points 4, 5 and 6 (Brinkgreve, et al., 2019b)

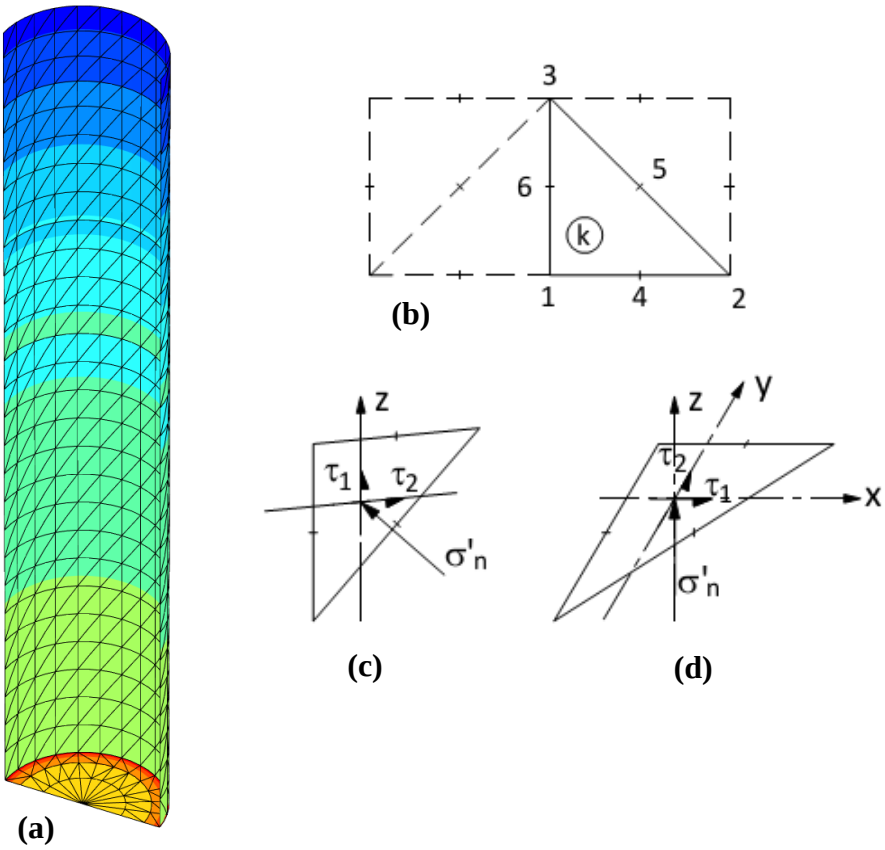

Figure 2.15. Interface discretization (a), stress points on triangular elements (b) and stresses on elements along pile wall (c) and at pile base (d).

When applying equation 2-30 into computing soil reactions described by equations 2-16 to 2-19, w_i is taken into considering distributed angle $\Delta\theta_i$ for the stress points. The weighted factor is also considered in determining distributed length for calculation of total

lateral resistance and resisting moment caused by distributed horizontal reaction p(z) and moment m(z), respectively. The reactions are determined without considering inclination of the pile which means that pile rotation is assumed to be negligible. Therefore, force equilibrium is checked for lateral loads on pile at different driving force levels and the errors is found less than 3% for all the cases (Table 2.4)

Soil reactions are generated for Case 1 and Case 2. Contributions of base shear, H_b, and resisting moments caused by vertical stress at pile base, M_b, by base shear, M_{Hb}, and summation of m(z) – M_{mz} – are examined in relations to driving load, H_g, and moment at ground, M_g. Lateral reaction p(z) at selected depths above and below rotational point are compared with API p-y curves. Coefficient of lateral subgrade reaction, k_h, is selected for layer 1 and layer 2 per API recommendations (API, 2020). Triaxial friction angle reported by Zdravković, et al. (2019), therefore, is utilized for determining p_u values of the p-y curves.

2.10.1. Effect of OCR on soil reactions

Differences in soil reactions generated for Case 1 and Case 2 are presented in Table 2.4 and figures from 2.16 to 2.18. Table 2.4 and Figure 2.16 show that similar p(z) was caused by mentioned cases and summation of p(z) by Case 2 is slightly larger. As a result, values of H_b obtained from Case 2 are greater those of Case 1 to maintain equilibrium. Summations of p(z) for zones above and below point of rotation shows that Case 2 has larger resultants of p(z) in both zones up to lateral load of 1,960kN. Point of rotation is deeper in Case 2 to this value of load. The opposite trend in p(z) resultants is observed for larger loads, where similar depth of rotational point is noticed in both cases. However, summation of p(z) for whole pile length in Case 2 is consistently larger.

Since soil described with OCR are stiffer, the pile in analysis without OCR experiences larger displacement and rotation to mobilize sufficient resisting reactions. In layer 2, especially below rotational point, vertical stress $\tau_1(z,\theta)$ is larger in Case 2, resulting in greater summation of m(z) along pile length (Figure 2.17). Higher level of normal stress is mobilized under pile base in Case 2, resulting in bigger base shear and thus the moment caused by H_b (Figure 2.17). These findings suggest that m(z) and H_b play more significant roles in resisting driving forces in analysis without consideration of soil stress history.

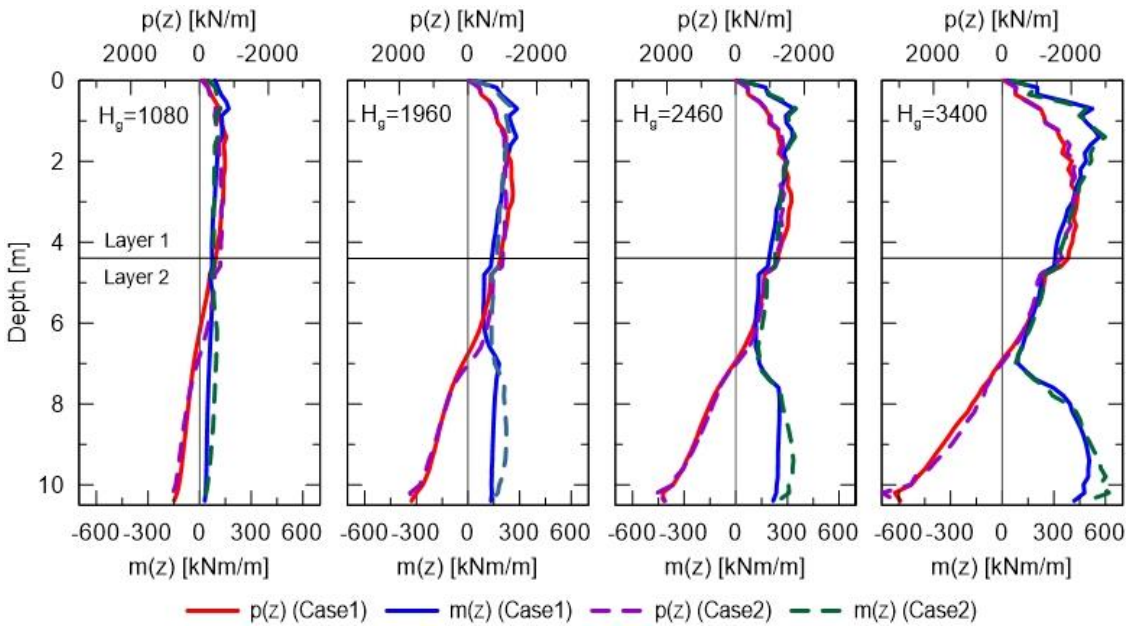

Figure 2.16. Distributions of p(z) and m(z) resulted from analyses for Case 1 and Case 2 at various values of lateral load.

Table 2.4. Force equilibrium check for lateral loads

H_g (kN)	Case 1			Case 2		
	Σp(z) (kN)	H_b (kN)	Error (%)	Σp(z) (kN)	H_b (kN)	Error (%)
365	-428.4	55.8	-2.07	-433.2	64.4	-1.04
400	-470.6	63.6	-1.75	-476.3	73.8	-0.62
1,080	-1,337.1	242.7	-1.33	-1,358.3	290.8	1.16
1,960	-2,252.0	334.2	2.15	-2,301.1	394.6	2.73
2,460	-2,779.2	386.3	2.73	-2,826.3	434.7	2.78
3,000	-3,319.7	402.1	2.75	-3,356.0	432.9	2.56
3,400	-3,732.9	407.5	2.43	-3,760.7	438.1	2.28
3,960	-4,289.7	415.6	2.17	-	-	-
4,370	-4,697.6	418.2	2.07	-	-	-

Note: Negative values for Σp(z) is to indicate direction of total reaction opposite to that of H_g and H_b. Negative error means that Σp(z) is greater than sum of H_g and H_b and vice versa.

2.10.2. Contribution of soil reaction components

M_b is found to make up less than 1% of M_g in both cases so it has limited contribution compared to H_b, m(z), and p(z) in soil resistance. H_b is in the same direction of H_g and equal to about 22% and 27% of H_g in Case 1 and Case 2, respectively. H_b approaches to it maximum value as H_g goes beyond 2,500kN. Meanwhile, resistance induced by distributed moment m(z) – M_z – double its share, from 6% to 12% of M_g, as lateral load increases from 0 to 3,400kN in Case 2 and to 4,370kN in Case 1. Total resisting moment by m(z) and H_b ranges from 22% to 31% of M_g in Case 1 and from 25% to 37% in Case 2.

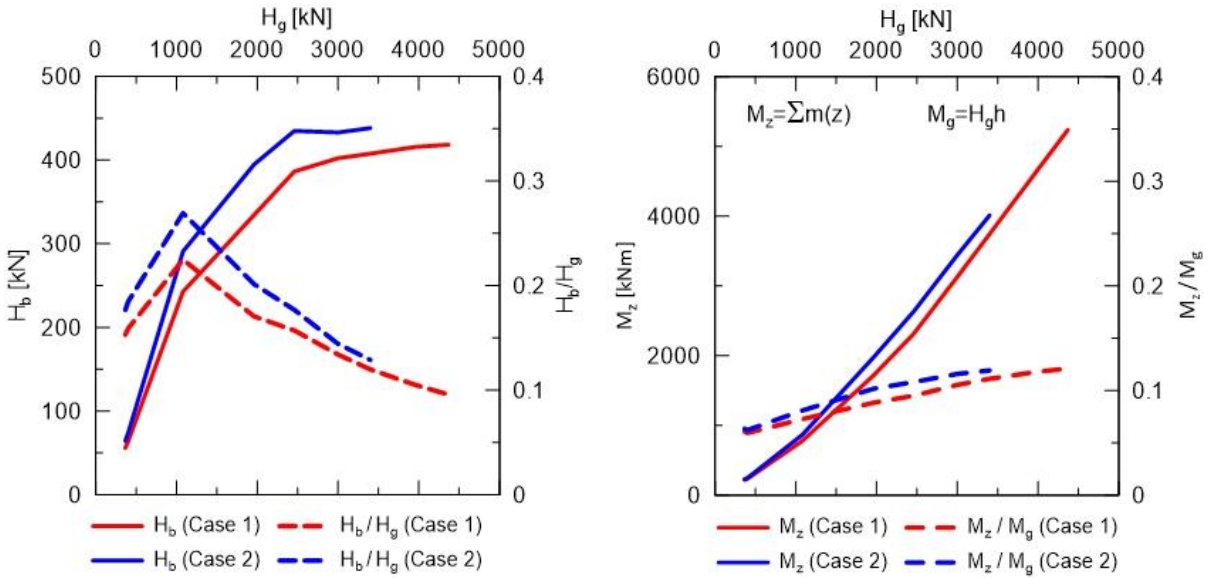

Figure 2.17. Development of H_b (left) and M_z (right) with applied lateral load

2.11. P-y curves generated by numerical simulation versus API recommendations.

Figure 2.18 compares p-y curves obtained from numerical analyses and by equations 2-20 to 2-23 recommended by API (2020) for selected depths above and below rotation point. Simulation-generated p-y curves are derived from Case 1 and Case 2 analyses up to the lateral load of 4,370 and 3,400kN, respectively. Meanwhile, API recommended p-y relations are built with k_h selection in accordance with soil D_R and submergence and triaxial ϕ' reported by Zdravković, et al. (2019) (Table 2.5)

It is obvious that p-y curves by Case 2 is softer as the pile needs to displace further to reach the same reaction as in Case 1. However, consistent with Figure 2.16 at a certain value of lateral load, reaction in two cases is similar and either case might have larger figure from depth to depth. The FEM-based curves at all selected depths have not reached the ultimate

reaction. At shallow depths, i.e. 1.4m and 2.2m, reaction obtained from numerical analyses can exceed p_u of API curves. However, the difference in reactions by numerical analyses and API formulation is enlarged at deeper locations. In general, API curves has higher stiffness and arrive at ultimate resistance at lower deflection. Similar findings are reported in studies by (Yan and Byrne, 1992) and Lam and Law (1996).

Table 2.5. Input of k_h (API, 2020) and ϕ' (Zdravković, et al., 2019) for API p-y curves

Layer	Description	k_h (kN/m^3)	ϕ' (deg)
1	D_R=100%, above water table	74,640	44.25
2	D_R=86%, below water table	42,070	42.33

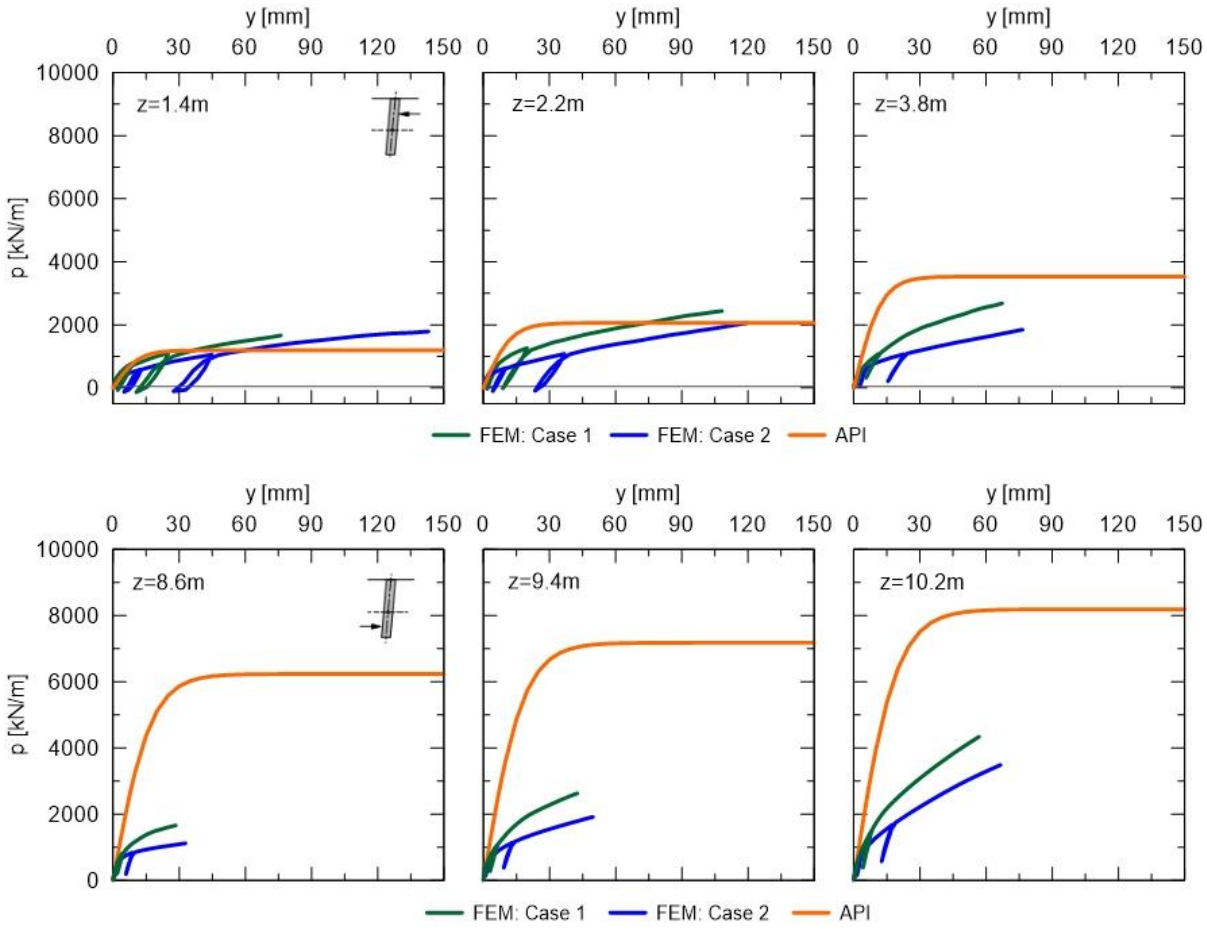

Figure 2.18. Comparisons of p-y curves obtained from analyses with and without soil history consideration and by API recommendation for selected depths above (top) and below (bottom) point of rotation.

There are some reasons for the differences. Firstly, API formulation was developed with assumption of that initial stiffness, or reaction modulus, linearly increased with depth and it overestimated stiffness of p-y curves from depth of few pile diameters (Lam and Law, 1996). Secondly, p_{u1} defined by equation 2-22 underestimates ultimate reaction at depths above point of rotation and, in contrast, overestimates the values for the zone below due to negligence of soil-pile interface friction. It is worth mentioning that the depth z*, where $p_{u1} = p_{u2}$, depends on pile diameter and ϕ'. For ϕ' in range from 30^o to 45^o, the ratio of z*/D ranges from 13 to 29 (Figure 2.19); therefore, for all p-y curves plotted in Figure 2.18 $p_u=p_{u1}$.Even though correction factor A_s is applied, the roots of the problem are likely not correctly identified and addressed.

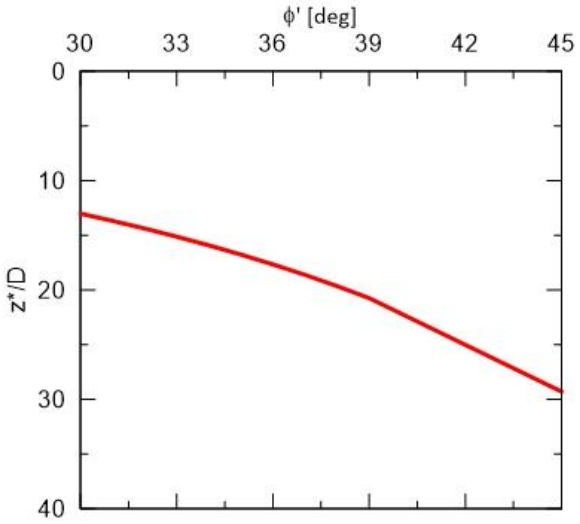

Figure 2.19. The depth where API's $p_{u1}=p_{u2}$ for various friction angle

Reese, et al. (1974) found that pile wall friction was not significantly influential to p_{u1}. However, their consideration of interface friction likely did not include two following key aspects:

- Difference in sign of pile wall friction angle: depending on relative displacement between soil and pile surface, pile wall friction angle could be either positive or negative. Above rotational point, the angle tends to be positive (surrounding soil causes an upward dragging stress on pile surface), and it increases soil passive-like pressure; on contrary, below the turning point, the angle is negative and has opposite effects.

- Effect of pile wall friction on altering shape of failure surface (Figure 2.20): when wall friction angle ϕ_w is greater $\phi'/3$, curved sliding surface must be considered (Terzaghi and Peck, 1967). The positive angle leads to a deeper and longer curved sliding surface than Coulomb or Rankine's failure plane, and an increased ultimate resistance. The negative wall friction angle yields the reversed outcome.

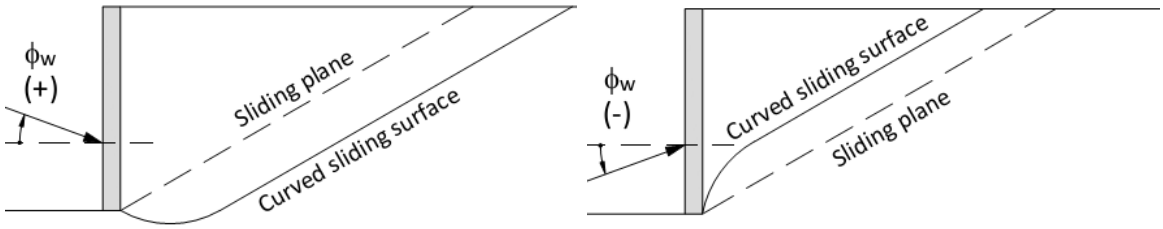

Figure 2.20. Effect of wall friction angle on passive failure surface (Terzaghi and Peck, 1967)

The pile-wall interface friction coefficient is included in numerical analyses. Distributions of m(z) confirm that there are upward shear stress $\tau_1(z,\theta)$ in the passive zone above point of rotation and downward shear stress in the passive zone below (as described in Figure 5). Figure 2.21 unveils the relative vertical displacements between pile wall and surrounding soil, and it can be concluded that positive and negative angle of wall friction occur above and below point of rotation, respectively. That is likely the reason why p-y curves obtained at 8.6m and 9.4m do not appear to be stiffer than the one at 3.8m as what is observed with the curves in API p-y family.

2.12. Validation of model parameters for loose sand

2.12.1. Test pile set-up

The simulation procedure is repeated for another pile test in loose sand. The test pile, S5, is one in total of 12 pile tests performed at Constructed Facility Lab, North Carolina State University (Aguirre, et al., 2018). The test pile cross section and pile material is described in Figure 2.22 and Table 2.6. Soil medium is bounded by pit wall circular concrete plate near bottom of the pit and two half-moon shaped concrete plates on top as described by Figure 2.23. Additional surcharge on soil surface can be applied tension forces on vertical post-tension bars connecting the concrete. The bounded conditions created by pit wall and soil-

sandwich system allow the formation of inground plastic hinge and reaching pile failure before pile collapse due to reaching ultimate lateral capacity.

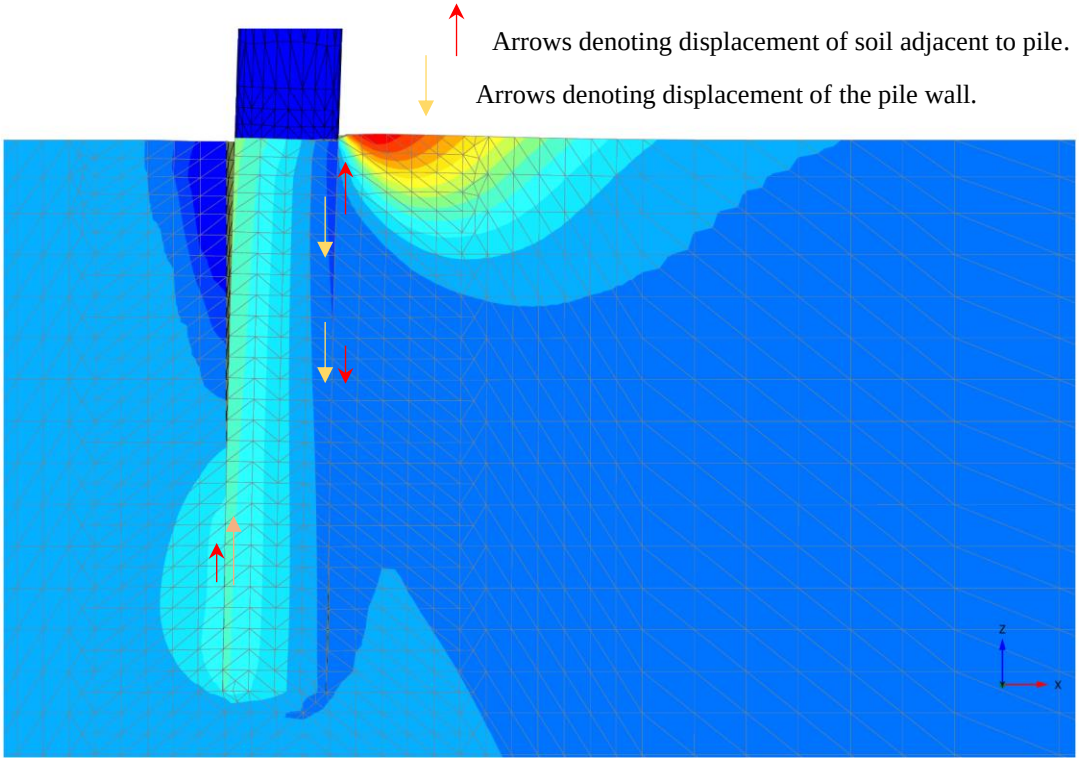

Figure 2.21. Typical vertical displacement pattern of soil adjacent to pile and the pile wall.

The two-way loading protocol applied at pile head is displacement controlled with single cycle for elastic region, three-cycle for inelastic response, and increasing displacement amplitude until pile rupture (Figure 2.24). The Δy'=9.55cm is the anticipated pile head displacement at first yield limit state, where yielding starts occurring in steel tube. The displacements for loading cycles prior to first yield are at Δy'/4, Δy'/2 and 3Δy'/4. The predicted pile head displacement at equivalent yield limit state is 14.3cm.

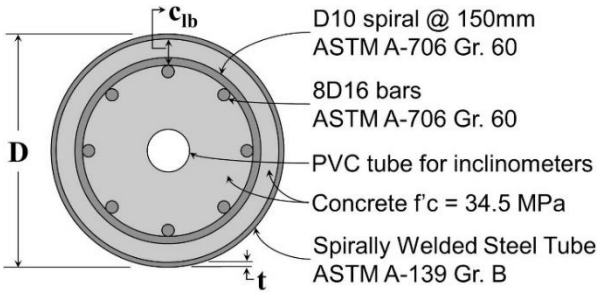

Figure 2.22. Test pile typical cross section (Aguirre, et al., 2018)

Table 2.6. Pile S5 cross section parameters (Aguirre, et al., 2018)

Pile test	L (m)	D (m)	t (mm)	D/t	Cantilever length (m)
S5	5.82	0.324	3.3	95	1.73

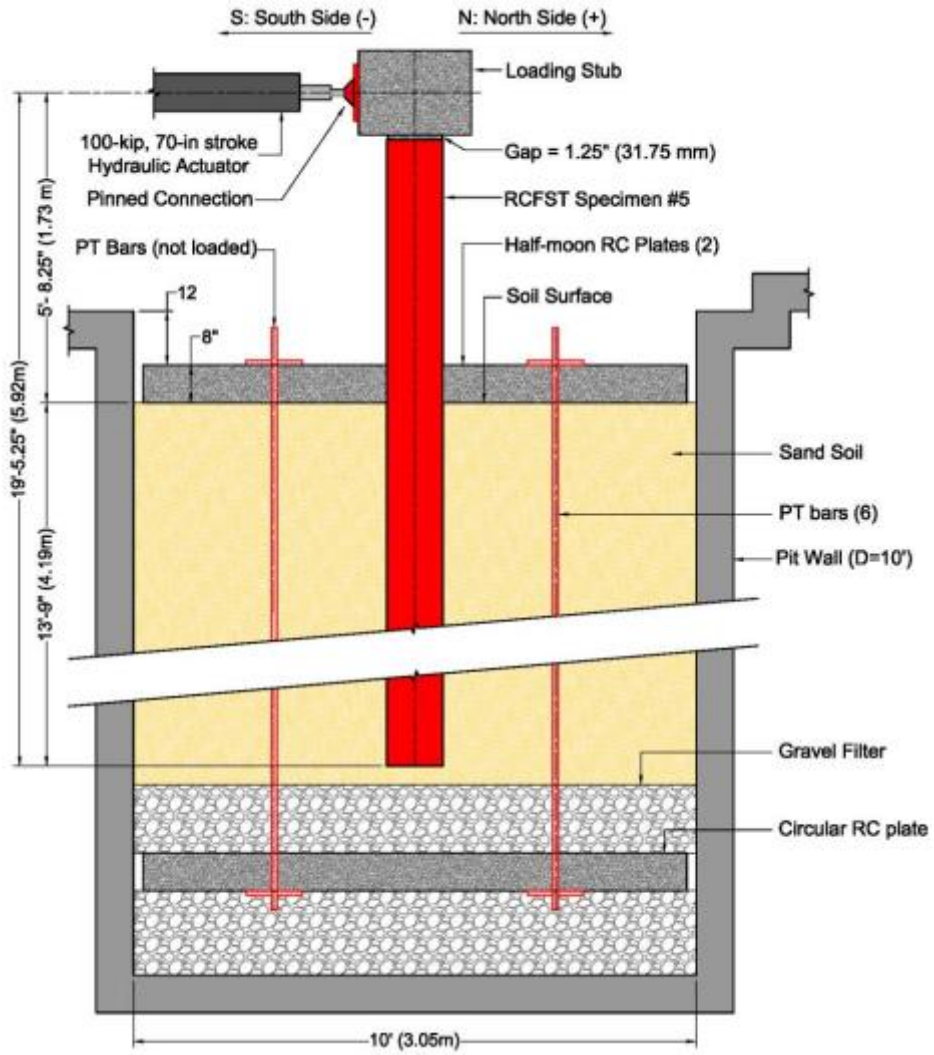

Figure 2.23. Pile test S5 setup (Aguirre, et al., 2018)

2.12.2. Soil condition and pile installation

Piles are placed into desired depth when soil is being liquefied; therefore, pile installation effect is negligible. Water then drains down out of the pit through valve for some days. The formed moist homogeneous fine to medium sand domain, therefore, is expected to be in loose packing and to have some level of cohesion due to matrix suction, which

contributes to formation of the gap between soil and pile surface during testing. Soil tests, including particles size distribution, specific gravity, moisture content, and 16 triaxial tests are conducted to classify the soil and determined friction angle and modulus. Soil relative density of 11% is back calculated by performing numerical simulation of the pile test with monotonic load (Vo, 2016) and is adopted for this study.

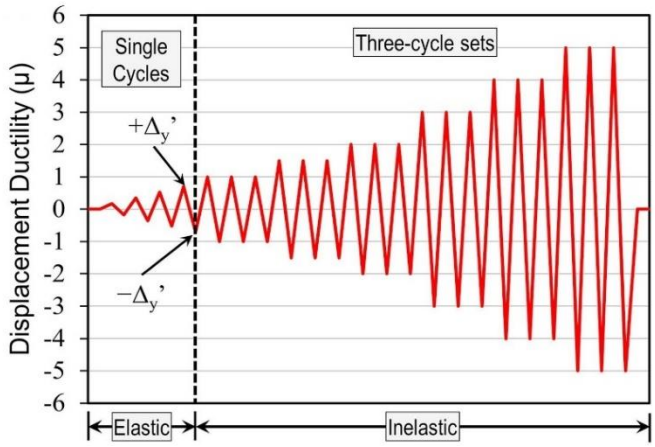

Figure 2.24. Typical pile head displacement history (Aguirre, et al., 2018)

2.12.3. Model parameters for pile

The test specimen is a reinforced concrete-filled steel tube pile and is described as a composite volume pile. The pile section comprises of elasto-plastic shell elements enclosing an elastic core representing the reinforced concrete. Since crack occurs as section curvature increases, cracked section flexural rigidity $(EI)_{cr}$ = 13,626 kN/m^2 is determined from moment-curvature response and is used to defined elastic modulus for the core (Vo, 2016). Yield stress f_y = 374.9 MPa is assigned to the shell element material to capture the yielding to steel casing, if necessary.

2.12.4. Model parameters for soil

Model parameters are computed with assumed soil relative density of 11%. Soil domain are layered into sublayers with thickness of 0.3m. CPT q_c is generated from soil D_R (equation 2-8) and soil friction angle, K_0, OCR, G_o and G_o^{ref} are computed by equations 2-4, 2-5, 2-7, 2-15 and 2-29, respectively, at mid-depths of each sublayers (Figure 2.25). Parameters for small-strain stress-strain curves, namely $\gamma_{0.7}$ and the ratios of $G_{ur}^{ref} / G_o^{ref} = 0.3$

and $E_{ur}^{ref} / E_{50}^{ref} = 4$ are chosen as in Table 2.2. Friction angle ϕ' =29.8° and cohesion c=0.65 kN/m^2 are assigned to soil layers. Interface elements are described along pile length and for pile tip area to capture the gap between soil and pile surface, if applicable.

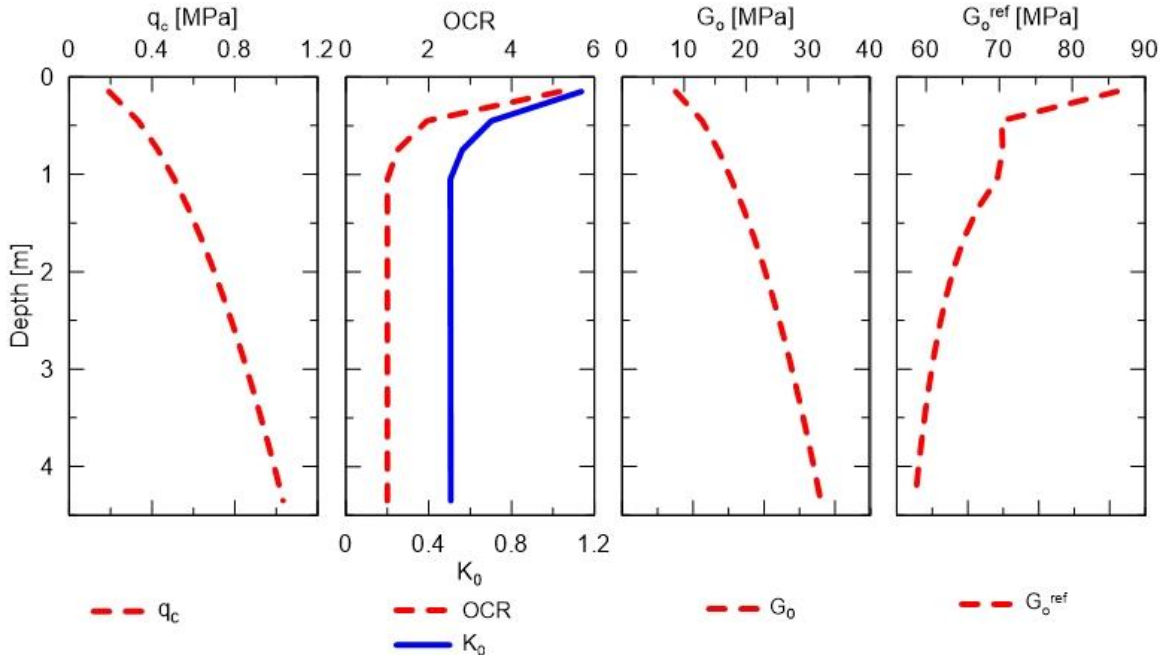

Figure 2.25. CPT tip resistance and soil properties computed for test pile S5

2.12.5. Simulation results

The simulations are performed up to the displacement that corresponds to limit state of equivalent yield of pile section (ductility of 1). Finite element model includes presence of pit wall and concrete plate on top of soil domain (Figure 2.26). Lateral displacement is applied on pile at level of 1.73m to simulate displacement-control pile test. First simulation is for monotonic loading to determine the pile head load-displacement backbone response. Second one is with cyclic loading to capture the pile head load-displacement loops comprising of loading, unloading, and reloading segments.

Pile head load-displacement response and outcomes on displacement profile at the end of loading cycles are compared with experimental data (Figure 2.27 and Figure 2.28). Overall, both data sets are in good agreement. Pile head load-displacement and displacement profiles resulted from numerical modeling match better with experimental figures while pile remains elastic (up to first yield) than beyond yielding. Besides limitation of the software in

describing inelastic behavior of the pile, effect of soil caving-in is not considered in the simulation. The gap between soil and pile surface was observed during the tests. When pile deflection is still small, soil medium is intact thanks to cohesion; however, as the deflection increases, local collapse on soil walls starts from sides and then from back of the pile, falling into gapping spaces. This phenomenon likely has impact on side shear between soil and pile surface and the soil reaction in front of the pile when loading is reversed.

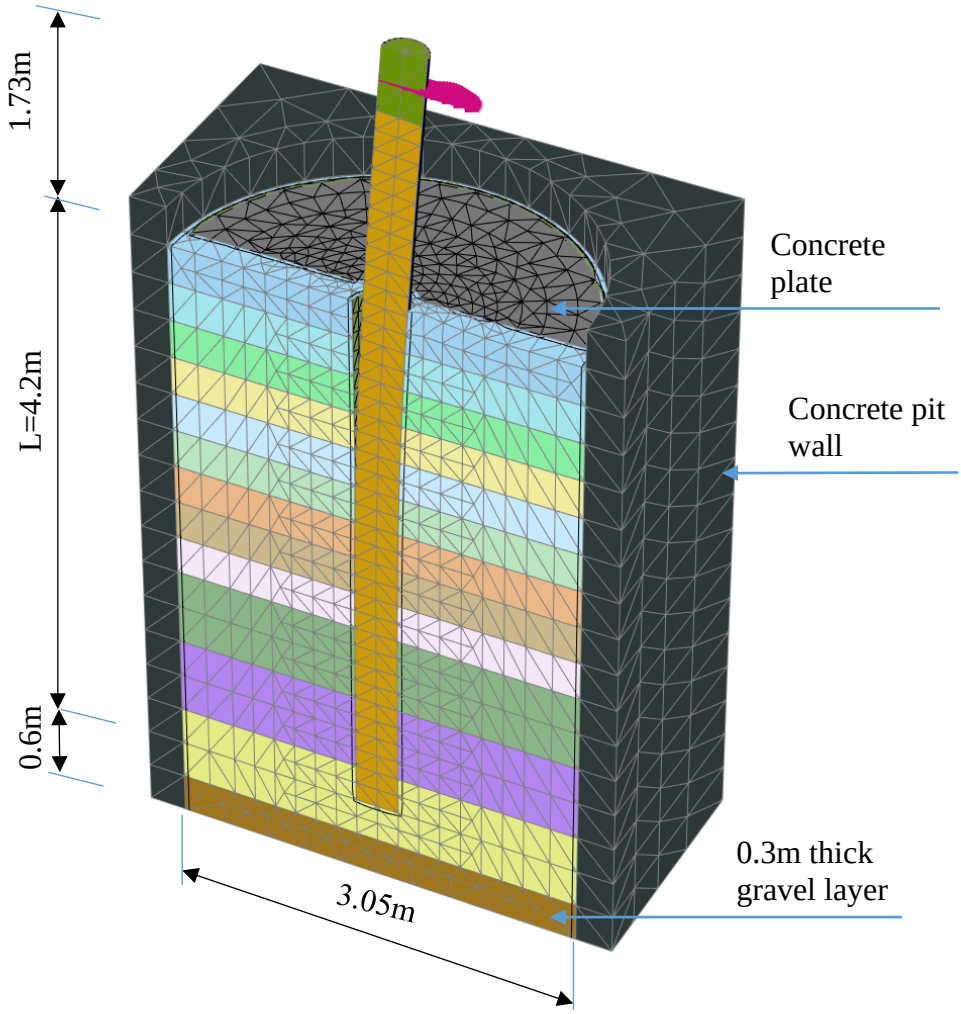

Figure 2.26. Pile S5: Finite element model and soil domain meshing.

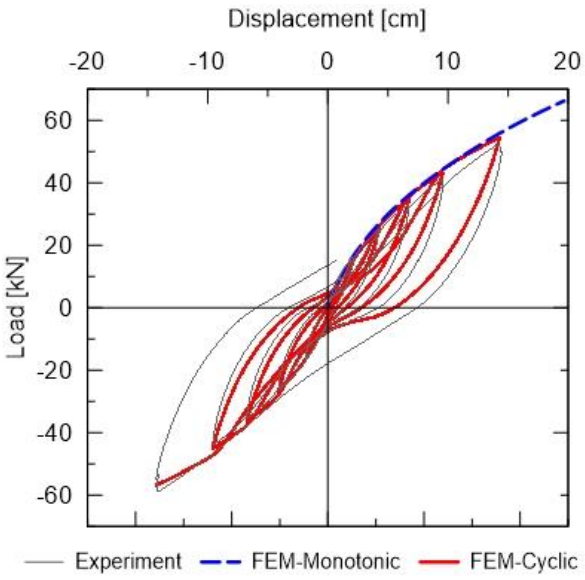

Figure 2.27. Pile S5: Pile head load-displacement response.

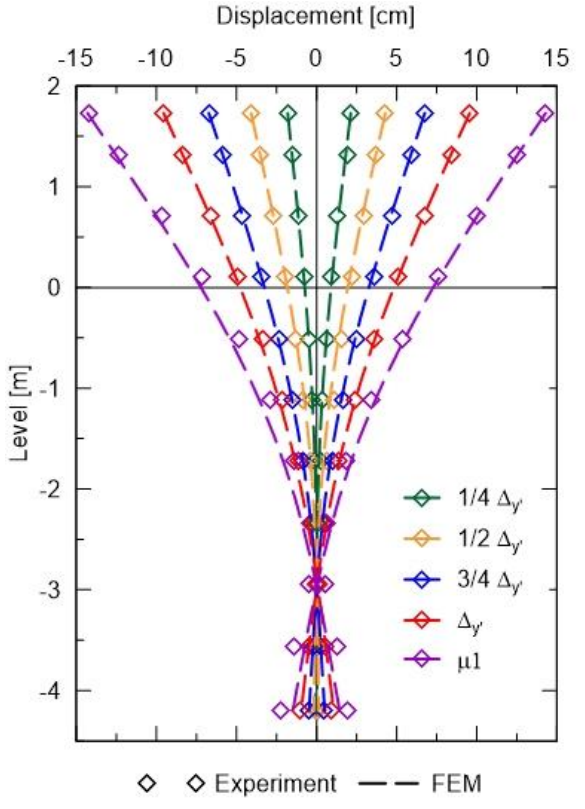

Figure 2.28. Pile S5: Displacement profile at peaks of push and pull cycles.

2.13. Conclusions and Recommendations

Effects of soil loading history parameters on lateraly loaded pile analyses are investigated. OCR and K_0 are determined by correlation with CPT q_c and Mayne and Kulhawy (1982) OCR-K_0 relationship . These parameters affects initial stress state ,input values of G_0 and stress-strain consistutive relation in numerical analyses and, therefore, influence the outcomes of pile load-displacement response and soil reactions . Following are the conclusion drawn from thi study's results :

- A modified G_o-q_c correlation is formulated for Baldi, et al. (1989) chart by adding two correction factors for effective stress, F_σ, and OCR, F_{OCR}, into an existing description by Jardine, et al. (2005). Baldi, et al. (1989) G_o-q_c correlation can be rewritten as:

$$G_{o,OCR} = \left(1 + 0.16 \log OCR\right)\left(\frac{300}{\sigma'_{vo}}\right)^{0.078} \left\{q_c \left[0.0203 + 0.00125\eta + \left(1.216E-6\right)\eta^2\right]^{-1}\right\}$$

- Parameters that define small strain stress-strain response, $\gamma_{0.7} = (2 - D_R)\cdot 10^{-4}$ recommended by Brinkgreve, et al. (2010), $G_{ur}^{ref} / G_o^{ref} = 0.3$ and $E_{ur}^{ref} / E_{50}^{ref} = 4$, appear to be work well in simulations of laterally loaded piles in both dense and loose sands. Along with soil history characteristics, above values are recommended for HSsmall constitutive model.

- Simulations of laterally loaded piles that use loading history of existing ground are proved to have accurate estimations of load-displacement responses at mudline/pile head level and displacement profiles of piles installed into dense sand by hammer (with installation effect) and placed into loose sand via liquefaction (without installation effect)

- Simulations with OCR and K_0 of exsiting ground and without considering pile installation effect better capture load-displacement responses of the pile tests. OCR appears to have major effect on analyzed results as overconsolidated soil elements experience reloadling before reaching preconsolidation pressure and entering virgin compression segment, resulting in stiffer response than that obtained fromanalyses for normally consolidated soil. Change in assumption of K_0 from OC to NC

condition does not lead to remarkable change in pile response as long as the simulation desribes initial stress state and corresponding maximum shear modulus at reference pressure $\left(G_o^{ref}\right)$ in consistence with the chosen stress-dependent rule for soil modulus and assumption on soil stress history.

- Pile installation effect, therefore, is only significant if it has created higher OCR than the OCR of the ground before the pile is installed. Study on impact of pile installation on lateral performance of pile, therefore, should focus on the maximum stress (vertical an/or lateral) in soil medium caused by the pile driving method.
- Soil reactions are generated for test pile DL2 by integrating stresses on interface elements. Distributed moment m(z) and base shear H_b have significant contributions in resisting driving forces, and the contributions are larger in analysis without OCR. H_b is in the same direction as driving force, H_g and can be equal to 24% to 27% of H_g in analyes with and without OCR, respectively. Sumation of m(z) can make up up to 12% of total resisting moment while moment cause by H_b is accounted for as much as 22% (with OCR) and 27% (without OCR). This values likely varies with different L/D ratios or/and caltilever lengths as suggested by Byrne, et al. (2015), and m(z) and H_b should not be negelected in analyses of short pile.
- Comparison of p-y curve generated from numerical analyses and API-recommended relation shows that in general numerically derived curves reach ultimate reaction at larger deflection. At shallow depths, lateral reactions from simulations exceed the ultimate value determined by API recommendations. API p-y curves understimates ultimate soil reaction at shallow depth (above point of rotation) and overestimate it at depth below rotation points majorly due to lack of considerations of sign of pile-wall friction angle and its effect on shape if the failure surface.

Further researches are recommeded on following topics:

- OCR and K_0 are determined from q_c based on Mayne and Kulhawy (1982) OCR-K_0 relationship. However, it is still unclear if the relationship is still valid for sandy soils, whose volume change are sensitive to shear vibration. Therefore, studies impact of shear wave propagation on soil K_0 and OCR is highly recommended. The

idea of using soil relative density as an indication of soil stress history also needs to be investigated.

- Since API $p_{u1} = p_{u2}$ at depth of from 13D to 29D for friction angle ranging from 30^o to 45^o, value of p_{u1} largely governs the outcomes of analyses using API p-y curves. Therefore, it is recommended to re-formulate the equation form p_{u1} that includes wall friction and its effect on slip surface , and K_0 profile in limit equilibrium analyses.

CHAPTER 3. NATURAL FREQUENCY AND FOUNDATION DAMPING OF MONOPILE-SUPPORTED OFFSHORE WIND TURBINE IN SANDY GROUND.

Abstract

This study examines impacts of monopile embedment, L_P, and diameter, D_P, on offshore wind turbine first natural frequency, $f_{1,d}$, and foundation damping ξ_{fnd}. Variation in foundation rigidity coefficient $\lambda = f_{1,d}/ f_{1,FB}$ represents influences of the pile dimensions and soil properties on $f_{1,d}$. OCR and K_0 of soil are considered and a soil constitutive model capturing hysteretic behavior is used in the analyses. ξ_{fnd} is found to be more sensitive to change in L_P and D_P. L_P generally has little impact but can significantly changes $f_{1,d}$ and ξ_{fnd} when it drops below the critical depth for constant displacement ($L_{c,const}$) . D_P is more influential to $f_{1,d}$ and ξ_{fnd}, and D_p - $f_{1,d}$ response is almost linear. The contribution of foundation rigidity coefficient to variation of $f_{1,d}$ is insignificant as D_P of the monopile in the study increases from 4m to 5m. Soil relative density appears to have opposite impacts on the rate of change in $f_{1,d}$ caused by variations in L_P and D_P. $f_{1,d}$ decreases more in softer soil as L_P declines but less with decreasing D_P.

3.1. Introduction

A monopile is major substructure-foundation component of offshore wind turbines (OTW) constructed in water depth up to 30m (Bhattacharya, 2014, Kallehave, et al., 2015a, Musial, et al., 2019). Multiple dynamic loads induced by operational rotor (1P), passing blades (3P), and wind and wave activities. Det Norske Veritas (DNV) (2002) code recommends that the first natural frequency of the system, f_1, should not fall within the frequency ranges of f_{1P} and f_{3P} plus safety margin of 10%, as illustrated in Figure 3.1. There is only a narrow band in the *soft-stiff* zone recommended for common practice of wind turbine design since the *soft-soft* corresponds to very flexible system and, in contrast, *stiff-stiff* design requires massive tower and foundation (Bhattacharya, 2014, 2019). Since wind turbine operational frequency varies with magnitude of wind load/speed on the structure (Kallehave, et al., 2015b) and with the presence of excitation loads that have varying frequency in range from 0.01Hz to 1Hz (Bhattacharya, et al., 2011), resonance and load amplification are significant concerns. The system needs to have suitable natural frequency and sufficient damping to minimize impacts of resonance and load amplification on

accumulation of fatigue damages. Accuracy of f_1 and system damping estimations, therefore, is crucial for evaluations of load ampilification/resonance and consequent risk of fatigue damages in structure.

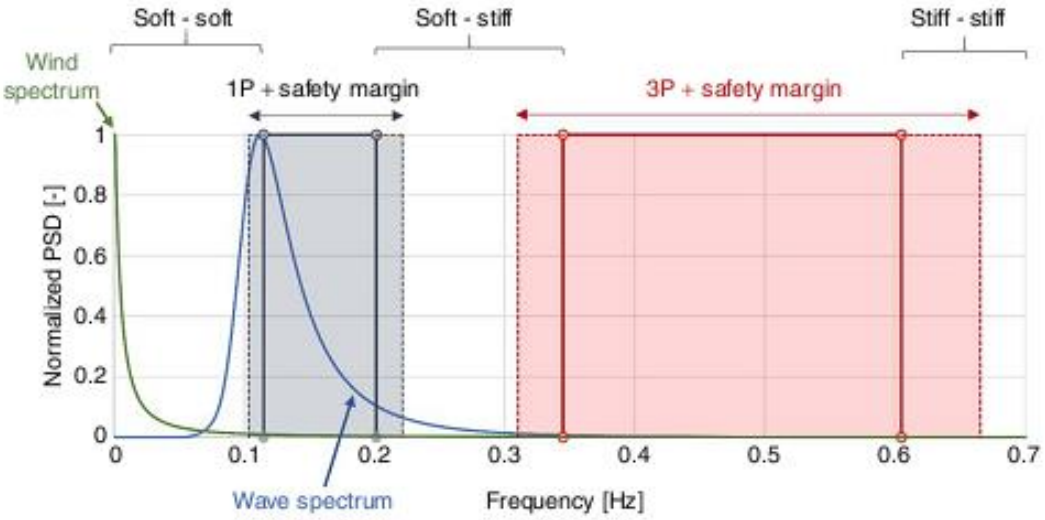

Figure 3.1. Normalized power spectral density (PSD) and frequency ranges of loads acting on offshore wind turbine system (Bhattacharya, 2019).

Offshore wind turbine frequency and damping ratio are directional dependent. Due to misalignment of wind and wave loading, the vibration happens in both along-wing (fore-aft) and crosswind (side-side) directions. System damping consists structural damping, hydrodynamic damping, soil/foundation damping and aerodynamic damping (Carswell, et al., 2015, Chen and Duffour, 2018, Cook and Vandiver, 1982, Shirzadeh, et al., 2013, Tarp-Johansen, et al., 2009). In fore-aft direction of an operating wind turbine, passing blades induces high level of aerodynamic damping, which is the largest factor in system damping, to dampen vibration energy and amplitude. However, in crosswind direction of running turbines or in both directions of idle or park wind turbines, with low or negligible aerodynamic component, the system damping is much less and, therefore, the side-side vibration can have substantial impact on fatigue lifespan of the wind turbines (Damgaard, et al., 2013, Kallehave, et al., 2015a, Tarp-Johansen, et al., 2009).

Foundation damping is the second largest contributor in system damping for fore-aft vibration and the most prominent damping component for vibration in crosswind direction. Therefore, performing acceleration measurements and dynamic simulation of wind turbines

in rotor-stop tests are reasonable approached to determine foundation damping (Carswell, et al., 2015, Damgaard, et al., 2013). Moreover, it is reported by Germanischer Lloyd (2005), Damgaard, et al. (2013), Tarp-Johansen, et al. (2009), Versteijlen, et al. (2011) and Shirzadeh, et al. (2013) that foundation damping defined by existing literature has poor agreement with values back-calculated from measurements on full-scale wind turbines. That likely results from the facts of that soil damping for wind turbine foundation is insufficiently studied and of that soil damping, being hysteretic strain-dependent material damping (Carswell, et al., 2015, Cook and Vandiver, 1982), is normally described as constant or frequency-dependent viscous dashpots in common analyses (Álamo, et al., 2018, Carswell, et al., 2015, Chen and Duffour, 2018, Damgaard, et al., 2013, Shirzadeh, et al., 2013, Tarp-Johansen, et al., 2009, Versteijlen, et al., 2011, Zania, 2014). Description of soil damping ratio at depths along pile length and lumped values of foundation damping at the mudline requires considerations of hysteretic behavior of material and strain distribution in soil domain surrounding the pile. Another the reason is related to wind turbine design process, where monopile dimensions are chosen by Serviceability Limit State (SLS) and Ultimate Limit State (ULS) design criteria before being checked with frequency recommendation (Arany, et al., 2017) with limited available guidelines on selecting values for foundation damping (Carswell, et al., 2015). Therefore, the impacts of monopile configurations on foundation damping and associated risk of fatigue damages are overlooked.

The design of offshore wind turbine is only conservative when f_1 of the offshore wind turbine–support structure–foundation is accurately estimated (Bhattacharya, 2014). However, Damgaard, et al. (2014) and Kallehave, et al. (2015a) find that f_1 of monopile wind turbines and is generally underpredicted (Figure 3.2). Zaaijer (2006) reported an underpredicted error of about 50% of a monopole wind turbine at Lely (Netherlands) in design, which resulted in the operational frequency of the wind turbine lying within frequency range of 3P load. Underestimation of f_1 leads to selection of larger-than-required pile and substructure dimensions. However, this practice decreases soil damping in the crosswind direction and total damping, to which accumulation of structural fatigue damage has high sensitivity (Aasen, et al., 2017, Fontana, et al., 2015), and, therefore, might result in shorter fatigue lifespan even though larger pile dimensions are selected.

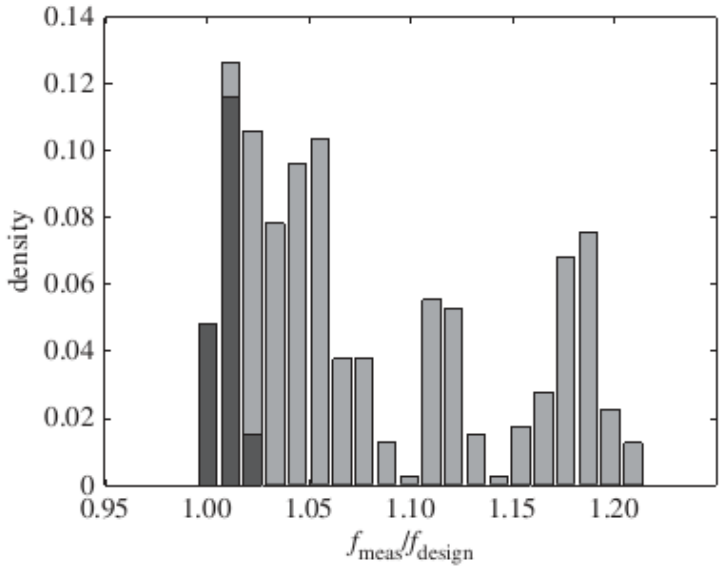

Figure 3.2. Ratio of measured to design first natural frequency for 400 OWTs (Kallehave, et al., 2015a).

This study herein investigates sensitivity of system first natural frequency and foundation damping ratio to monopile diameter and embedded length in sandy ground with different packing state. Numerical dynamic analyses are performed with a constitutive model capturing hysteretic damping of soil and consideration of existing ground stress history. The results will be compared to previous studies by Arany, et al. (2016) and Álamo, et al. (2018). Influences of pile dimensions on pile displacement profile and strain distribution in soil domain along pile length are examined to understand their effect on dynamic behavior of the monopile wind turbines.

3.2. Overview on natural frequency and soil damping of monopile wind turbine

3.2.1. Determination of natural frequency of monopile wind turbines

Natural frequency of wind turbines can be estimated numerically, experimentally with scaled models, and by measurements on full-scale structure. Scaled experiments are performed with forced vibrations to find resonance frequencies or an impulsive excitation following by recording system's acceleration decay (Bhattacharya, et al., 2013, Bhattacharya, et al., 2011, Prendergast, et al., 2015, Prendergast, et al., 2013). Full-scale measurements of monopile-supported offshore platforms and wind turbines have been reported by numerous studies for operational mode and rotor-stop tests (Cook and Vandiver, 1982, Damgaard, et

al., 2013, Devriendt, et al., 2013, Hansen, et al., 2006, Jensen, 1990, Magalhães, et al., 2010, Shirzadeh, et al., 2013, Versteijlen, et al., 2011). The rotor-stop tests are performed to have free vibration in one direction without significant effects of wind loading and aerodynamic damping, which are compatible with vibration if cross-wind direction (Damgaard, et al., 2013). Scaled experiments and full-scale measurement required instrumentation of acceleration transducers and/or strain gages at various locations on the structures and performing spectral analyses, for example Fast Fourier Transformation (FFT), on collected data to determined first dominant frequency peaks and first damped frequency, f_1. System damping, ξ, is defined by fitting exponential curve to decay time series of documented acceleration or displacement (Devriendt, et al., 2013, Magalhães, et al., 2010, Shirzadeh, et al., 2013, Versteijlen, et al., 2011).

The numerical modal analysis is commonly performed by finding Eigen value solutions for the system of discrete lumped masses, beam elements and springs for soi stiffness. Soil domain is described as distributed springs (for stiffness) (Cook and Vandiver, 1982, Damgaard, et al., 2013, Prendergast, et al., 2015, Sørensen and Ibsen, 2013). American Petroleum Institute (API) p-y curves are widely used in this approach. Alternatively, in a simplified approach, the combined effect of inground portion of pile and soil domain is lumped as a set of springs at mudline level (Álamo, et al., 2018, Arany, et al., 2016, Bhattacharya, et al., 2013, Carswell, et al., 2015, Zaaijer, 2006, Zania, 2014, Zuo, et al., 2018). Soil damping is typically described as dashpots in addition the spring to consider energy loss during vibration.

Following findings have been drawn from previous studies:

- Offshore wind turbine frequency varies with wind speed/load acting on the rotor (Kallehave, et al., 2015b). The frequency decreases over time as local scour develops around the pile (Prendergast, et al., 2015, Prendergast, et al., 2013, Sørensen and Ibsen, 2013) while calculation considering scour protection layer yields larger frequency than that resulted from analysis with soil only (Kallehave, et al., 2015a, Kallehave, et al., 2015b)
- The frequency is expected to change with increasing number of loading cycles (Bhattacharya, et al., 2013) and the sign of the change, positive or negative, depends

on whether the soil has hardening or softening behavior with respect to number of cycles of load (Bhattacharya, 2014)

- API p-y curves are reported to underestimate soil stiffness in offshore wind turbine natural frequency analyses, resulting in lower frequency than observed figures of operational wind turbines (Kallehave, et al., 2015a, Kallehave, et al., 2012). The main reason is that API p-y curves was developed and validated for piles that have configurations (diameter and embedded length-to-diameter ratio) very different from monopile. There have been efforts to revise the p-y curves from measured data on offshore monopile wind turbines, e.g. by Hald, et al. (2009) and Kallehave, et al. (2012), with the later using maximum shear modulus G_o and stress-strain relationship in small strain region to reformulate corresponding segment of p-y curve.

3.2.2. Foundation damping for monopile wind turbines

Monopile wind turbine system damping is estimated as the sum of damping components from soil, structure, hydrodynamic interaction between structure and wave, aerodynamic interaction by rotating blades and airflow during bending vibration (Arany, et al., 2016, Chen and Duffour, 2018, Cook and Vandiver, 1982, Damgaard, et al., 2013, Shirzadeh, et al., 2013). System damping and is components are determined by experimental measurements on operating or parked wind turbines.

$$\xi = \xi_{struc} + \xi_{damper} + \xi_{hydro} + \xi_{aero} + \xi_{fdn} \qquad (3\text{-}1)$$

where:

- ξ_{struc} - structural damping ratio, consisting of damping of the material (steel) and structural connections; $\xi_{struc} = 0.15\% - 1.5\%$ (Arany, et al., 2016) or 0.2% – 1.5% (Chen and Duffour, 2018)
- ξ_{damper} - damping ratio of oscillation dampers integrated to wind turbine system.
- ξ_{hydro} - hydrodynamic damping ratio, consisting of wave radiation and viscous damping; $\xi_{hydro} = 0.07\% - 0.23\%$ (Arany, et al., 2016) or 0.11% – 0.39% (Chen and Duffour, 2018)

- ξ_{aero} - aerodynamic damping ratio; in fore-aft direction: $\xi_{aero} = 1.0\% - 6.0\%$ (Arany, et al., 2016) or 4.0%-8.0% (Chen and Duffour, 2018), and in side-side direction or parked turbines $\xi_{aero} = 0.06\% - 0.23\%$ (Arany, et al., 2016) or $0.08\% - 0.24\%$ (Chen and Duffour, 2018).
- ξ_{fdn} - foundation/soil damping ratio, consisting of soil hysteretic and radiation damping, with the latter is negligible for frequencies less than 1Hz (Carswell, et al., 2015, Cook and Vandiver, 1982), which is the typical frequency range of loads acting on wind turbines and the structures' vibration. ξ_{fdn} is reported in range of 0.444% - 1.0% (Arany, et al., 2016) or 0.17% - 1.3% (Chen and Duffour, 2018).

In numerical analyses describing soil/foundation stiffness as springs, soil/foundation damping is described as viscous dampers. Carswell, et al. (2015) utilizes soil hysteretic stress-strain loops and distribution of shear stress in soil volume in pile vicinity to find global foundation damping ratio.

System damping ratio could be in ranges of 1% - 4% for side-side vibration and 2%-10% for fore-aft direction (Arany, et al., 2016, Chen and Duffour, 2018). Therefore, risk for fatigue damages is more prominent for wind turbines structure in cross-wind direction or when the turbines are idle or parked. Fontana, et al. (2015). Studies have shown that increase in damping results in lower moment at mudline, reduced fatigue damage, and increased fatigue life of monopole wind turbine (Damgaard, et al., 2015, Fontana, et al., 2015, Rezaei, et al., 2018).

3.2.3. Impacts of monopile dimensions on system natural frequency and foundation damping

Natural frequency and foundation damping of monopile wind turbine is dependent of level of loading, soil condition and monopile dimensions (Álamo, et al., 2018, Arany, et al., 2016, Đilas, 2018). Arany, et al. (2015a) and Arany, et al. (2016) develop an analytical 3-spring model including lateral stiffness K_L, rotational stiffness K_R and cross-coupling spring K_{LR} and formulate a closed-form solution for first natural frequency (Figure 3.3). Álamo, et al. (2018) employed the similar model, of which the foundation stiffness is lumped as three impedance functions. Each function includes two frequency-dependent terms that represent the stiffness and damping. Parametric studies on impacts of monopile diameter and

embedded length on dynamic characteristics of the structure are performed in the studies and the outcomes are summarized as follows:

- Although most monopoles are neither slender nor rigid pile by definitions by Poulos and Davis (1980), Randolph (1981) or (Carter and Kulhawy, 1992), spring stiffness defined by equations for slender/long pile are more suitable for the analyses. K_R has largest influence on natural frequency (Arany, et al., 2015a, Arany, et al., 2016)
- Change in pile diameter is most influential on variation in natural frequency and foundation damping ratio, while pile embedded length has little effect (Álamo, et al., 2018). This conclusion is in agreement with above finding by Arany, et al. (2016) , because for slender piles, the spring stiffness correlates at higher degree to pile diameter.
- Variations in natural frequency and foundation damping are lower in harder soil

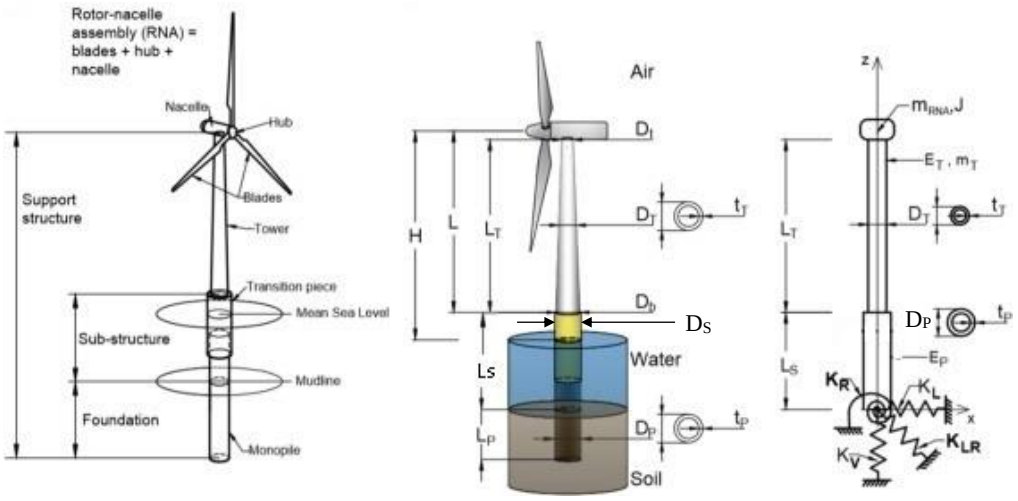

Figure 3.3. Terminology of wind turbine components and model (Arany, et al., 2016).

In both studies, level of loading and mobilized strain are not considered. Therefore, it might be valid for certain condition of wind and wave loads acting on the structure and might need modification to values of soil modulus/stiffness and damping parameters in equations for K_L, K_R, and K_{LR} and impedance functions when analyzing for other environmental scenarios with very different wind speed and wave height.

3.2.4. Closed-formed solution for Eigen frequency by Arany, et al. (2016)

First natural frequency of an offshore wind turbines, which is supported by monopile foundations as described by Figure 3.3, can be estimated by equations from 3-2 to 3-13 (Arany, et al., 2016):

$$f_1 = C_L C_R f_{1,FB} = C_L C_R (C_S f_{FB,T}) \quad (3\text{-}2)$$

where: f_{FB} is the fixed-base first natural frequency of the wind turbine structure, $f_{FB,T}$ is the fixed-base first natural frequency of the tower structure only, C_L and C_R are lateral and rotational foundation flexibility coefficients, and C_S is the substructure flexibility coefficient.

$$f_{FB,T} = \frac{1}{2\pi}\sqrt{\frac{3E_T I_T}{\left(m_{RNA} + \frac{33}{140}m_T\right)L^3}} \quad (3\text{-}3)$$

where: m_{RNA} is the mass of rotor-nacelle assembly, m_T is the mass of the tower, L is the distance from tower bottom to rotor center, and

$$I_T = \frac{1}{8}\pi D_T^3 t_T \text{ is average tower section area moment of inertia} \quad (3\text{-}4)$$

with t_T and $D_T=0.5(D_t+D_b)$ are the average tower wall thickness and tower diameter, respectively.

C_S reflects the effect of transition piece dimensions. In the study, transition piece is assumed to have monopile diameter, D_P, instead of its own diameter D_S (Figure 3.3)

$$C_S = \sqrt{\frac{1}{1+(1+\psi)^2\chi - \chi}} \quad (3\text{-}5)$$

$$\text{where: } \chi = \frac{E_T I_T}{E_P I_P} \text{ is bending stiffness ratio} \quad (3\text{-}6)$$

$$\psi = \frac{L_S}{L_T} \text{ is transition piece/tower length ratio} \quad (3\text{-}7)$$

C_L and C_R are formulated from K_L, K_R, and K_{LR}, which incorporate soil stiffness, pile embedded length and diameter, and tower flexural rigidity and dimensions.

$$C_L(\eta_L,\eta_R,\eta_{LR}) = 1 - \frac{1}{1+0.5\left(\eta_L - \frac{\eta_{LR}^2}{\eta_R}\right)} \quad (3\text{-}8)$$

$$C_R(\eta_L,\eta_R,\eta_{LR}) = 1 - \frac{1}{1+0.6\left(\eta_R - \frac{\eta_{LR}^2}{\eta_L}\right)} \quad (3\text{-}9)$$

$\eta_L, \eta_R, \eta_{LR}$ are non-dimensional foundation stiffness

$$\eta_L = \frac{K_L L_T^3}{E_T I_\eta} \qquad \eta_{LR} = \frac{K_{LR} L_T^2}{E_T I_\eta} \qquad \eta_R = \frac{K_R L_T}{E_T I_\eta} \quad (3\text{-}10)$$

where: $E_P I_P$ is pile section flexural rigidity, L_T is length of the tower and $E_T I_\eta$ is the tower equivalent flexural rigidity considering change in tower cross section (diameter and wall thickness) over its length. For a tower that has linearly declining from D_b at bottom to D_t at top:

$$E_T I_\eta = f(q) E_T I_{top} \quad (3\text{-}11)$$

where:

$$I_{top} = \frac{1}{8}\pi D_t^3 t_t \quad \text{is the moment of inertia of the section at tower top} \quad (3\text{-}12)$$

$$q = \frac{D_b}{D_t}; \quad f(q) = \frac{2q^2(q-1)^3}{3(2q^2 \ln q - 3q^2 + 4q - 1} \quad (3\text{-}13)$$

The set of equations from 3-2 to 3-13 by (Arany, et al., 2016) requires input of foundation stiffness. Equations for K_L, K_R, and K_{RL} have been proposed by many researchers, including Carter and Kulhawy (1992), Gazetas (1984), Pender (1993), Poulos and Davis (1980), Randolph (1981) and (Shadlou and Bhattacharya, 2016). The formulation is based on assumption on distribution of soil stiffness over depth (constant, linear or parabolic) and classification of pile behavior (flexible or rigid). Arany, et al. (2016) recommend to use foundation stiffness proposed by Poulos and Davis (1980) and Randolph (1981).

Equations from 3-2 to 3-13 are only suitable for monopiles that are categorized as non-rigid (Arany, et al., 2016). Pile rigidity can be evaluated by slenderness parameter β

recommended by Poulos and Davis (1980) (equation 3-14). Formulae for K_L, K_R, and K_{LR} of monopiles, which have slenderness parameter $\beta L_P \geq 1.5$ and are embedded in soil that has stiffness linearly increasing with depth, are expressed by equation 3-15 (Poulos and Davis, 1980).

$$\beta = \sqrt[4]{\frac{k_h D_P}{4E_P I_P}} \tag{3-14}$$

$$\begin{cases} K_L = 1.074 k_h^{3/5} \left(E_P I_P\right)^{2/5} \\ K_{LR} = -0.99 k_h^{2/5} \left(E_P I_P\right)^{3/5} \\ K_R = 1.48 k_h^{1/5} \left(E_P I_P\right)^{4/5} \end{cases} \tag{3-15}$$

where: D_P is pile outside diameter, and k_h is soil lateral subgrade reaction coefficient. Terzaghi's (1955) equation (3-16) for k_h is used in the study by Arany, et al. (2016)

$$k_h = A \frac{\gamma'}{1.35} \tag{3-16}$$

where: γ' is soil effective unit weight and A=100-300 for loose sand, A=300-1000 for medium sand, and A=1000-2000 for dense sand.

3.3. Selection of monopile dimensions

Natural frequency is one of the criteria of offshore monopole wind turbine design. Selection of monopole embedded length, L_P, diameter, D_P, and pile wall thickness, t_P, are based on load cases and design criteria for ultimate limit state (ULS), serviceability limit state (SLS) and fatigue limit state (FLS). As described by Arany, et al. (2017), natural frequency is normally checked after the monopile diameter and embedded length have been evaluated by some ULS and SLS requirements. Therefore, it is important to understand which loads combinations are used for monopile analyses and how the selection of pile dimensions by ULS and SLS criteria affects the outcomes of natural frequency analyses.

3.3.1. Wind loading on monopile

The thrust force (T_h) is proportional to square of wind speed and is computed as:

$$T_h = 0.5 \rho_a A_R C_T U^2 = 0.5 \rho_a A_R C_T \left(\bar{U} + u\right)^2 \tag{3-17}$$

where ρ_a is density of air, A_R is swept area of rotor blades, C_T is thrust coefficient, and U is wind speed. The wind speed is modeled as being comprised of mean speed, $\bar{U}$, and a turbulent component, u. Several turbulence models are defined by (IEC, 2009) to evaluate wind turbulence in different wind conditions. The thrust coefficient, C_T, used in these computations is approximated according to the mean speed in relation to the cut-in speed (U_{in}) and the cut-out speed (U_{out}), as shown in equations 3-18 and 3-19 (Frohboese, et al., 2010):

$$C_T = 3.5\left(2U_R + 3.5\right)\frac{1}{U_R^2} \quad \text{for } U_{in} \le \bar{U} \le U_R \quad \text{in m/sec} \tag{3-18}$$

$$C_T = 3.5U_R\left(2U_R + 3.5\right)\frac{1}{\bar{U}^3} \quad \text{for } U_R \le \bar{U} \le U_{out} \quad \text{in m/sec} \tag{3-19}$$

3.3.2. Wave loading on pile

A simplified way to estimated wave load acting on substructure is the Morrison equation (Morison, et al., 1950). Wave force on a unit length of the pile consists of the summation of drag force f_D and inertial force f_I as shown in equation 3-20.

$$f = f_D + f_I = 0.5\rho_w C_D \left|u(x,z,t)\right| u(x,z,t) + \rho_w C_M \frac{\pi D^2}{4}\dot{u}(x,z,t) \tag{3-20}$$

where ρ_w is density of sea water, and $u(x,z,t)$ and $\dot{u}(x,z,t)$ are wave particle velocity and acceleration, respectively. C_D and C_M are drag and inertia coefficients, respectively, and are dependent on Reynolds and Keulegan-Carpenter numbers. C_D=0.7, C_M =2.0 for fatigue and C_D=0.6, C_M =1.7 for extreme conditions (Kühn, 2001)

The values of $u(x,z,t)$ and $\dot{u}(x,z,t)$ can be determined from linear wave theory with x=0 for the substructure

$$u(0,z,t) = \frac{\pi H_w}{T_S}\frac{\cosh\left(k(S+z)\right)}{\sinh\left(kS\right)}\cos\left(\frac{2\pi}{T_S}t\right) \tag{3-21}$$

$$\dot{u}(0,z,t) = \frac{-2\pi H_w}{T_S^2}\frac{\cosh\left(k(S+z)\right)}{\sinh\left(kS\right)}\sin\left(\frac{2\pi}{T_S}t\right) \tag{3-22}$$

where: H_w and T_S are wave height and period, respectively, S is water depth, and k is

wave number computed from dispersion relation.

$$\omega^2 = gk\tanh(kS) \qquad \text{with } \omega = 2\pi / T_S \tag{3-23}$$

3.3.3. Wind and waves conditions

Arany, et al. (2017) summarize five wind and wave loading scenarios, among load cases recommended by design codes, that are essential for design of monopile wind turbine foundation (Table 3.1). These scenarios consider combination of wind and wave conditions. Wind conditions define values for average spped, $\bar{U}$, and turbulence models for u while wave conditions define sea states with corresponding wave heights, periods, and return periods. Wind turbulence models are established by (IEC, 2005) and weight heigh and period at a certain return period can be computed from 50-year significant wave height, $H_{50,S}$, (DNV, 2014) which is obtained from site measure data.

Since wave is induced by wind, it is typical that normal or extreme wind speed and wave height happen at the same time. However, largest wind thrust on the rotor does not occurs at the highest wind speed since pitch-control mechanism lessens wind load when wind speed exceeds rated speed, U_R, and the turbine shuts down at cut-out wind speed, U_{out}, for safety.

It is logical that monopile embedded length and diameter determined by ULS requirements and SLS criterion on deformation are based on extreme load combinations. However, natural frequency, fatigue damages and accumulated deformation should not be required to be evaluated in those conditions because critical situations happen briefly compared to the life span of the wind turbine and extreme wind gust and extreme wave height are of 50-year return period.

3.3.4. Monopile embedded length and diameter

Typical diameter of monopile is in range of 4-6m and embedded length to diameter ratio of less than 10 (Bhattacharya, 2014, LeBlanc, et al., 2010). However, the use of extra-large diameter of up to 10m for deeper water (e.g. 45m to 60m) is in discussion (Bhattacharya, 2014, Kallehave, et al., 2015a, Taborda, et al., 2019). Monopile dimensions are more governed by requirements for deformations, especially pile rotation, and stiffness than by a required factor of safety against ultimate capacity (LeBlanc, et al., 2010).

Kuo, et al. (2012) and Achmus, et al. (2009) review critical embedded length recommended by Germanischer Lloyd (2005) and (DNV, 2009) for static analysis. The critical embedded length is determined by following criteria

- Zero toe-kick: $L_{c,ztk}$ is the minimum embedded length that provides zero displacement at pile tip.
- Vertical tangent: $L_{c,vt}$ is the embedded length that yields vertical tangent of displacement profile at pile tip, and
- Constant pile head displacement: $L_{c,const}$ is the pile length that gives lowest pile head displacement, which remains constant as the length is extended.

The authors conclude that zero toe-kick constraint is overconservative and results in pile embedment that might be impractical for monopile. Vertical tangent is not a suitable requirement for critical embedded length and $L_{c,const}$ is suggested as a better criterion for design. Accumulated displacement under cyclic of the pile with $L_{c,const}$ is slightly larger than that of the pile with $L_{c,ztk}$ in the studied problem using soil degradation stiffness method for cyclic loading (Kuo, et al., 2012).

$L_{c,const}$ and $L_{c,ztk}$ are proportional to values of lateral load and moment arm of the load or bending moment (Kuo, et al., 2012) and likely are dependent on pile diameter and soil stiffness as well. When the embedded length is varied selected in between $L_{c,const}$ and $L_{c,ztk}$, pile head deflection is negligibly affected is governed by pile diameter. Likewise, natural frequency of monopile wind turbine is more sensitive to pile diameter than embedded length as in studies by Arany, et al. (2016) and Álamo, et al. (2016). However, the connection between critical embedded length and variation in system natural frequency and foundation damping have not been examined.

Variation of natural frequency and foundation damping due to changes in soil relative density, pile diameter and length of embedment is investigated in this study. Plaxis 3D finite element package is employed to perform numerical dynamic simulation of offshore monopile wind turbine in rotor-stop test. Hardening Soil with small strain modulus (HSsmall) constitutive model, which captures hysteretic behavior of soil. Calibrated model parameters including soil loading history characteristics are validated once more by comparing dynamic

analyses' results with measured natural frequency of existing wind turbines. Parametric study on effects of soil relative density, pile diameter and pile embedded length on system natural frequency and foundation damping ratio is subsequently performed. Outcomes on natural frequency are compared with values obtained from closed from equations by Arany, et al. (2016). Pile displacement profile and distribution of mobilized shear strain in the soil medium are employed to find the association between changes in pile dimensions and system dynamic characteristics.

Table 3.1. Simulation scenarios for foundation (Arany, et al., 2017)

Scenario	**Name & description**	**Wind model**	**Wave model**	**Alignment**
E1	Normal and operational condition	NTM at U_R (U-1)	1-year ESS (W-1)	Wind and wave act in the same direction
E2	Extreme wave load scenario	ETM at U_R (U-2)	50-year EWH (W-4)	Wind and wave act in the same direction
E3	Extreme wind load scenario	EOG at U_R (U-3)	1-year EWH (W-2)	Wind and wave act in the same direction
E4	Cut-out wind speed and extreme operating gust scenario	EOG at U_{out} (U-4)	50-year EWH (W-4)	Wind and wave act in the same direction
E5	Wind-wave misalignment scenario	ETM at U_R (U-2)	50-year EWH (W-4)	The wind and wave are orthogonal (at 90 ^{o})

Notations used in Table 3.1:

NTM: normal turbulence model

ETM: extreme turbulence model

EOG: extreme operating gust

U_R: rated wind speed ofwind turbine

U_{out}: cut-out wind speed of wind turbine

1-year Extreme Sea State (ESS): using 1-year significant wave height $H_{S,1}$

1-year Extreme Wave Height (EWH): using 1-year maximum wave height $H_{m,1}$

50-year Extreme Wave Height (EWH): using 50-year maximum wave height $H_{m,1}$

3.4. Input for numerical simulations

3.4.1. CPT-based soil parameters

The soil domain is assumed to have homogeneous relative density. The domain is

divided into sublayers and soil properties for a given sublayer are the average values that are computed at its mid-depth. Soil compressibility, shear strength and stress history parameters are included in the soil constitutive model. As concluded by the companion paper in Chapter 2, incoporating soil stress history imroves accuracy of laterally loaded pile analysis, especially of the load-displacement response in small deformation region. The paper uses Jamiolkowsky, et al. (1985) correlation between CPT q_c and soil realtive density, D_R (equation 3-24). Subsequently, soil paremeters are determined by empirical correlations with q_c recommended by Kulhawy and Mayne (1990) and Mayne, et al. (2001) for the analyses (equations 3-25 to 3-31). By varying soil relative density, profiles of q_c and soil parameters can be generated (Figure 3.4).

$$q_c = \left(1 + \frac{D_R - 30}{100}\right)\left(P_a \sigma'_{vo}\right)^{0.5} 10^{(D_R/68+1)} \qquad \text{with } D_R \text{ in percent} \qquad (3\text{-}24)$$

$$\phi' = 17.6 + 11\log\left(\frac{q_c / P_a}{(\sigma'_{vo} / P_a)^{0.5}}\right) \qquad (3\text{-}25)$$

$$K_0 = 1.33\left(q_c\right)^{0.22}\left(\sigma'_{vo}\right)^{-0.31}\left(OCR\right)^{0.27} \quad \text{with } q_c \text{ in MPa and } \sigma'_{vo} \text{ in kPa} \qquad (3\text{-}26)$$

where: P_a=100 kPa is atmospheric pressure and the overburden effective stress σ'_{vo} can be computed from soil saturated unit weight estimated by following formula (Brinkgreve, et al., 2010)

$$\gamma_{sat} = 19 + 1.6 D_R / 100 \quad (kN/m^3) \qquad \text{with } D_R \text{ in percent} \qquad (3\text{-}27)$$

With the assumption of that the OCR – K_0 relationship by Mayne and Kulhawy (1982) in Equation 4 is applicable, the OCR can be correlated to q_c as shown in Equation 5:

$$K_{0,OC} = (1 - \sin\phi')OCR^{\sin\phi'} \qquad (3\text{-}28)$$

$$OCR = \left[\frac{1.33(q_c)^{0.22}}{(1\text{-}\sin\phi')(\sigma'_{vo})^{0.31}}\right]^{\frac{1}{\sin\phi' - 0.27}} \qquad (3\text{-}29)$$

Soil small strain maximum shear modulus is dependent of soil void ratio, OCR and confining stress on soil element (Baldi, et al., 1989, Hardin and Black, 1966, Hardin and Richart Jr, 1963). In Chapter 2, two correction factors for OCR and effective stress are

introduced to Jardine, et al. (2005) expression to better capture q_c-G_0 relationship established by Baldi, et al. (1989) . The modified q_c-G_0 correlation is shown in equation 3-30.

$$G_{0,OCR} = \left(1 + 0.16 \log OCR\right)\left(\frac{300}{\sigma'_{vo}}\right)^{0.078}\left\{\frac{q_c}{0.0203 + 0.00125\eta - \left(1.216E-6\right)\eta^2}\right\} \quad (3\text{-}30)$$

$$\text{where } \eta = \frac{q_c}{\left(P_a \sigma'_{vo}\right)^{0.5}} \quad (3\text{-}31)$$

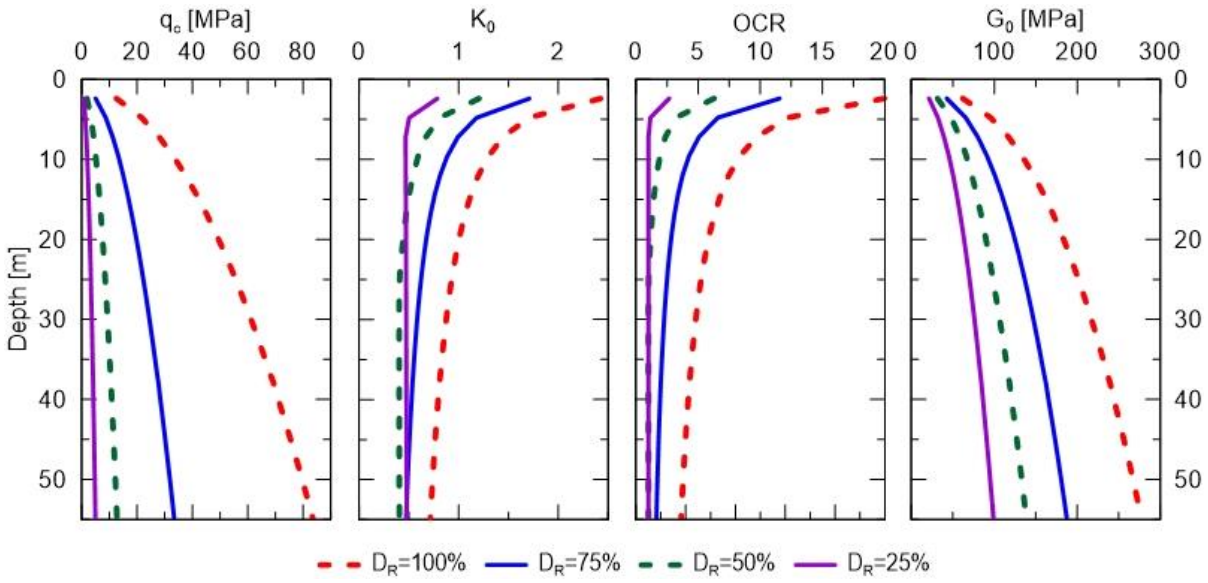

Figure 3.4. CPT cone resistance and soil properties obtained for various relative densities.

3.4.2. Shear modulus degradation curve and hysteretic damping in HSsmall model

Hardening Soil with small strain modulus (HSsmall) captures soils hysteretic behavior in small strain region Figure 3.5. Shear modulus degradation curve in HSsmall model follows Hardin and Drnevich (1972) relationship and subsequent modifications by Dos Santos and Correia (2001). Secant (G_s) and tangent (G_t) shear moduli are described as functions of shear strain (γ) as in equations 3-32 and 3-33 (Brinkgreve, 2005, Brinkgreve, et al., 2019a).

$$G_s = \frac{G_o}{1 + a\left|\gamma / \gamma_{0.7}\right|} \quad (3\text{-}32)$$

$$G_t = \frac{G_o}{\left(1 + a\left|\gamma / \gamma_{0.7}\right|\right)^2} \tag{3-33}$$

where a = 0.385 is a constant and $\gamma_{0.7}$ is the shear strain at which G_s=0.722G_0. Brinkgreve, et al. (2010) reported that $\gamma_{0.7}$ ranges between 1x10^{-4} to 2x10^{-4} and can be correlated to D_R (expressed in decimal form) as:

$$\gamma_{0.7} = (2 - D_R) \cdot 10^{-4} \tag{3-34}$$

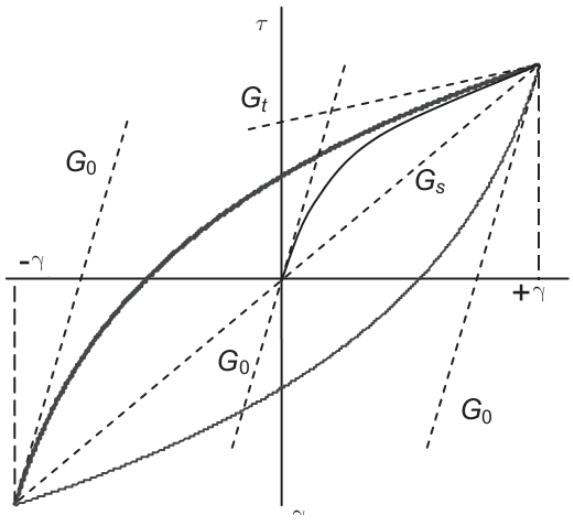

Figure 3.5. Hysteretic behavior of soil described in the HSsmall constitutive model.

HSsmall model uses Masing rule to define hysteretic damping. The hysteretic damping ratio at shear strain amplitude of γ is computed by equation 3-35 (Brinkgreve, et al., 2007):

$$\xi = \frac{A_D}{4\pi A_S} \tag{3-35}$$

where: A_D represents dissipated energy in the load cycle and A_S is stored energy at maximum strain γ

$$A_D = \frac{4G_o\gamma_{0.7}}{a}\left[2\gamma - \frac{\gamma}{1 + \gamma_{0.7}/(a\gamma)} - \frac{2\gamma_{0.7}}{a}\ln\left(1 + \frac{a\gamma}{\gamma_{0.7}}\right)\right] \tag{3-36}$$

$$A_S = 0.5G_s\gamma^2 = \frac{G_o\gamma^2}{2(1 + a\gamma/\gamma_{0.7})} \tag{3-37}$$

However, the small strain domain is bounded by the cut-off strain at $G_t = G_{ur}$, where G_{ur} is shear modulus corresponding to unloading/reloading modulus, E_{ur}. Beyond $\gamma_{cut-off}$, if soil element is still in reloading regime, the stress-strain response follows the modified segment of degradation curves with $G_t = G_{ur}$. Once entering virgin loading, the stress-strain relation is in hyperbolic form described by Duncan and Chang (1970) with E_{ur} being the initial tangent stiffness. Soil hysteretic damping ratio plateaus as $\gamma > \gamma_{cut-off}$.

$$G_{ur} = \frac{E_{ur}}{2(1+\nu_{ur})} \tag{3-38}$$

$$\gamma_{cut-off} = \frac{\gamma_{0.7}}{a}\left(\sqrt{\frac{G_o}{G_{ur}}} - 1\right) \tag{3-39}$$

where $\nu_{ur} = 0.2$ is Poisson's ratio for unloading/reloading.

The hyperbolic segment has three characteristic moduli namely secant modulus at 50% ultimate deviatoric stress, $E_{50,}$ unloading/ reloading modulus E_{ur}, and tangent modulus for primary loading, and constrained modulus, $E_{oed} = 0.8E_{50}$ (Brinkgreve, et al., 2019a). Whole stress-strain relationship within and beyond small strain zone will be defined once the ratios of G_{ur}/G_0 and E_{ur}/E_{50} are determined. Simulation of piles tests in Chapter 2 indicates that $G_{ur}/G_0 = 0.3$ and $E_{ur}/E_{50} = 4$ are suitable for dense and loose sand, and these values, therefore, are adopted in this study. By varying soil relative density, shear modulus degradation and damping curves with regard to shear strain are plotted for D_R of 100%, 75%, 50%, and 25% in Figure 3.6.

3.1.1. Soil modulus parameters for HSsmall model

The stress-dependent soil stiffness in the HSsmall constitutive model implemented within the Plaxis 3-D finite element model is evaluated at a reference confining stress $p'_{ref} = P_a = 100\text{kPa}$ (Brinkgreve, et al., 2019a). G_o^{ref} and G_{ur}^{ref} are modulus parameters for small strain segment and E_{ur}^{ref}, E_{50}^{ref}, and E_{oed}^{ref} are for hyperbolic stress strain relationship beyond $\gamma_{cut-off}$. G_o^{ref} is determined by equation 3-40 while the others are computed from correlations of $G_{ur}^{ref}/G_0^{ref} = 0.3$, $E_{ur}^{ref}/E_{50}^{ref} = 4$, and $E_{50}^{ref} = 0.825E_{oed}^{ref}$. For a given sublayer ***k***,

the average maximum shear modulus at the reference stress is computed at mid-depth as:

$$G_{o,k}^{ref} = \frac{G_{o,k}}{\left(\frac{c \cdot \cos\phi' - \sigma_3' \sin\phi'}{c \cdot \cos\phi' + P_a \sin\phi'}\right)^n} \quad (3\text{-}40)$$

where $G_{o,k}$ is the maximum shear stress determined by equation 3-30 or field measurements, $\sigma'_{z,k}$ and $\sigma'_{x,k}$ are vertical and horizontal geostatic stresses, c is soil cohesion, and n is pressure exponential number. For sand, n varies depending on confining pressure and soil relative density (Duncan, et al., 1980, Duncan and Chang, 1970, Wroth, 1979); however, n=0.5 is reported to well represent soil stiffness dependency on stress level (Janbu, 1963, Kelly, et al., 2006, Seed and Idriss, 1970, Wroth and Houlsby, 1985).

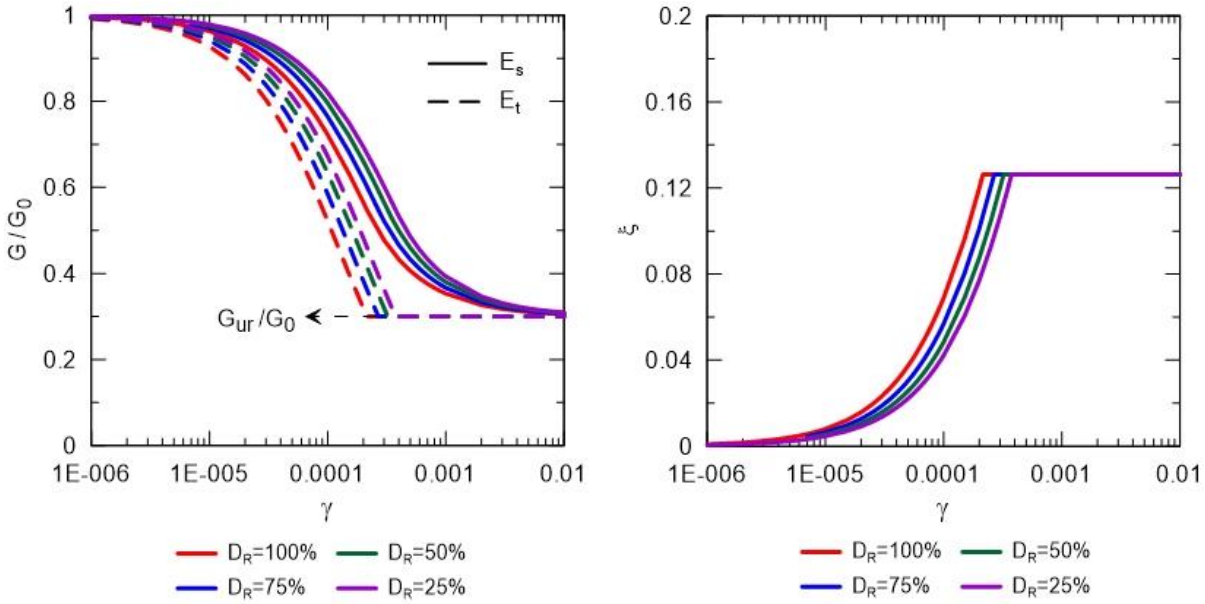

Figure 3.6. Secant modulus (E_S) and tangent modulus (E_t) (left), and soil hysteretic damping ratios (right) at different strain level in HSsmall model.

3.5. Wind turbines for model calibration and parametric study

3.5.1. Model Calibration

Three offshore wind turbines, which belong to three diferent offshore wind farms are used in the analyses herein, namely: Burbo Bank, Walney 1 and Gunfleet Sands. Data on wind turbines, superstructure and substructure geometries, met-ocean condition and

subsurface properties are adopted from studies by Arany, et al. (2016) and Jalbi, et al. (2019) (Table 3.2 and Table 3.3)

Table 3.2. Wind turbine data (after Arany, et al. (2016))

Parameter	**Symbol**	**Unit**	**Burbo Bank**	**Walney 1**	**Gunfleet Sands**
Mass of the rotor	m_{RT}	tons	234.5	234.5	234.5
Hub height from mean sea level	H	m	83.5	83.5	75.5
Tower top diameter	D_t	m	3	3	3
Tower bottom diameter	D_b	m	5	5	5
Average tower wall thickness	t_T	mm	28	44	33
Substructure length	L_S	m	22.8	37.3	28
Substructure diameter	D_S	m	5.45	6.46	5.40
Substructure wall thickness	t_s	mm	75	80	50
Pile diameter	D_P	m	5.0	6.0	5.0
Embedded length	L_P	m	24	30	38
Pile wall thickness	t_P	mm	75	80	50
Rated wind speed	U_R	m/sec	14.0		
Cut-out wind speed	U_{out}	m/sec	25.0		
Rotor operational frequency	f_{1P}	Hz	0.077 to 0.2		
Blades turning frequency	f_{3P}	Hz	0.231 to 0.6		
Measured 1st natural frequency	$f_{1,meas}$	Hz	0.292	0.35	0.314
Soil description	-	-	Dense sand	Medium and dense sand	Sand and clay
Soil relative density	D_R	%	100	75	75

The Siemens SWT-3.6-107 3.6 MW turbine is used for the structures. The turbine specifications indicate rotor operational frequency (f_{1P}) ranging from 0.077 to 0.2Hz. However, natural frequency measurements show that all three wind turbines operate at about 0.29 to 0.3Hz, which is outside the recommended range and is well inside blade turning frequency (f_{3P}) range, which is from 0.231Hz to 0.6Hz. Brief soil description is provided by

Arany, et al. (2016). The authors consider the grounds as homogeneous sand and use soil relative density of 100% for all three projects. In this study, lower D_R of 75% is selected for Walney 1 and Gunfleet Sands to be more suitable with the description on ground condition.

Table 3.3. Met-ocean data (after Jalbi, et al. (2019))

Parameter	**Symbol**	**Unit**	**Burbo Bank**	**Walney 1**	**Gunfleet Sands**
Water depth	S	m	8	21.5	15
50-year max. wave height	$H_{m,50}$	m	3.4	9.0	6.3
50-year max wave period	$T_{m,50}$	sec	6.5	10.6	8.9
1-year max. wave height	$H_{m,1}$	m	2.7	7.2	5.0
1-year max wave period	$T_{m,1}$	sec	5.8	9.5	8.0
1-year significant wave height	$H_{s,1}$	m	1.5	3.9	2.7
1-year significant wave period	$T_{s,1}$	sec	4.3	7.0	5.8

3.5.2. Parametric study

The parametric study is performed for the Gunfleet Sands wind turbine. 43 different dynamic simulations (including the model for validation) for natural frequency and foundation damping are performed in different soil properties and pile configurations. Monopile diameters of 5.0m, 4.7m, 4.4m, and 4.0m, embedment varies from 38m to 19.2m, and soil relative density is from 100% to 25% (Table 3.4). Soil parameters for the constitutive model vary with soil D_R as described in Figure 3.4 and Figure 3.6.

For each diameter, simulations are initially performed with L_P=38.0m, 24m, and 19.2m, and D_R=100%, 75%, and 25%. The largest changes in obtained natuaral frequency are -4.1% (from 0.315 to 0.308) when D_R declines from 100% to 25%, and -2.2% (from 0.322 to 0.308) when L_P decreases from 38m to 19.2m. Both largest variations happen with D_P=5.0m. Simulations at D_R=50% and L_P=31.2m are added to examine wether additional configurations are required. The additional results show that natual frequency for L_P=31.2m is almost identical to that at L_P=38.0m, and valuea for D_R=50% are very close to either those at D_R=75% or the mean of values at D_R=75% and 25%. Therefore, simulations at L_P=31.2m and D_R=50% are not performed to other diameters.

The outcomes of natural frequency are compared with that of the fixed base system, $f_{1,FB}$. As the monopile diameter changes, diameter of transition piece, $D_S=D_P+0.3m+2t_P$, alters as well, resulting in change in $f_{1,FB}$ although the tower dimensions remain unchanged. The distributed wave load on the system also is affected by variation in D_S. The monopole wall thickness is kept constant in the parametric analyses.

Table 3.4. Matrix of analyses on natural frequency and soil damping.

D_R(%) / L_P (m)	100	75	50	25	Remarks
38	D_P = 5.0, 4.7, 4.4, 4.0m	D_P = 5.0, 4.7, 4.4, 4.0m	D_P = 5.0m	D_P = 5.0, 4.7, 4.4, 4.0m	D_P=5, L_P=38 are dimensions of existing wind turbine
31.2	D_P = 5.0m	D_P = 5.0m	D_P = 5.0m	D_P = 5.0m	
24	D_P = 5.0, 4.7, 4.4, 4.0m	D_P = 5.0, 4.7, 4.4, 4.0m	D_P = 5.0m	D_P = 5.0, 4.7, 4.4, 4.0m	
19.2	D_P = 5.0, 4.7, 4.4, 4.0m	D_P = 5.0, 4.7, 4.4, 4.0m	D_P = 5.0m	D_P = 5.0, 4.7, 4.4, 4.0m	

3.5.3. Loading scenario for dynamic analyses

The excitation loads for the simulations are calculated in normal and operational condition (scenario E1 in Table 3.1). Peak values of coaligned wind thrust and wave load are used as the excitation. Values of wind load and total wave load on monopiles of three projects for calibration are summarized in Table 3.5 and Figure 3.7.

In parametric study, the wind thrust on the rotor are the same in all analyses. However, as D_S changes due to modification of D_P, distributed wave load varies accordingly. Distribution of wave load below mean sea level (MSL) for different pile diameters are plotted in Figure 3.7.

3.6. Numerical model

3.6.1. Simulation description

The dynamic analyses simulate rotor-stop test, where the system vibration is captured following the removal of excitation loads. Soil domain dimensions are illustrated in Figure

3.8 per recommendations by Wallace, et al. (2002) and Kim and Jeong (2011). The tubular structure members (tower, transition piece, and monopile) are described by elastic shell elements. The model does not consider the damping from aerodynamic, structural and hydrodynamic sources; therefore, foundation damping ratio is the only damping obtained from the analyses.

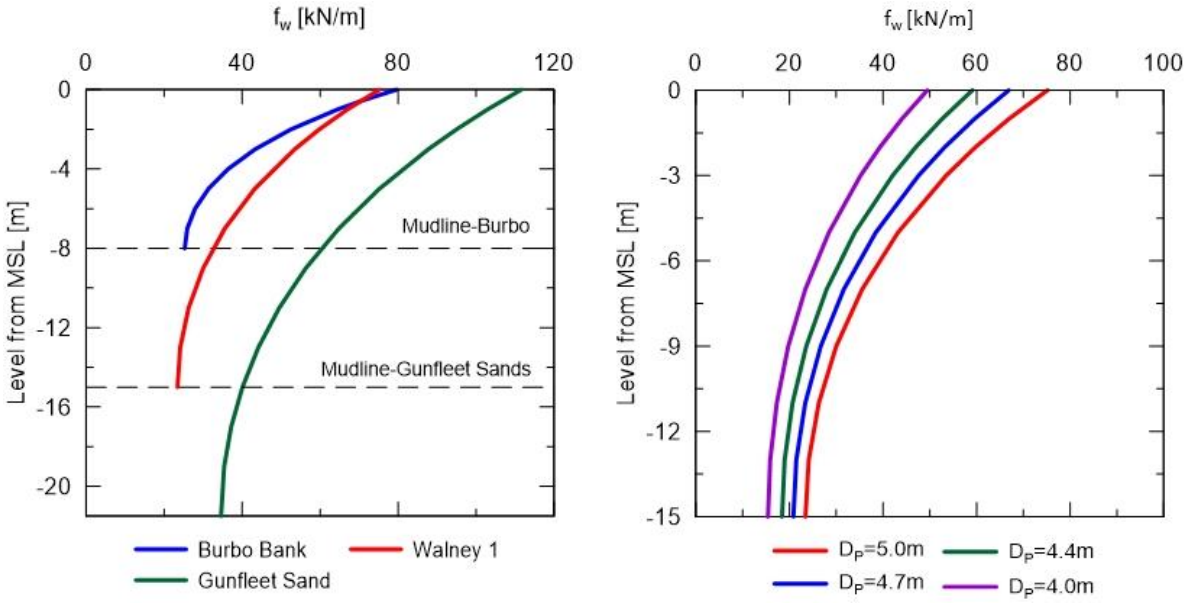

Figure 3.7. Distribution of wave load below mean sea level (MSL) of projects in calibration and for different pile diameters in parametric study.

Table 3.5. Summary of wind and wave load for normal and operational condition.

Parameter	**Symbol**	**Unit**	**Burbo Bank**	**Walney 1**	**Gunfleet Sands**
Mean wind speed	$\bar{U}$	m/sec	14.0		
Wind turbulence	u	m/sec	1.19		
Thrust coefficient	C_T	sec	0.5		
Wind thrust	T_h	kN	635.5		
Total wave load	W	kN	334.1	1,181	586.3

One cycle of excitation loads is applied before performing dynamic analysis. This is aimed to simulate actual soil stress-strain state in ground. The duration for dynamic analyses is 160sec and time interval Δt of calculation steps is 0.01sec. Time histories of lateral

displacement and acceleration at rotor or other level can be extracted from simulation outcomes. Fast Fourier Transformation is performed on displacement or acceleration record to determine the power energy spectrum and first vibration frequency, $f_{1,S}$, of the structure. Foundation damping, ξ_{fdn}, can be determined by curve fitting equation 3-41 to the decay of lateral displacement, velocity or acceleration amplitudes over time.

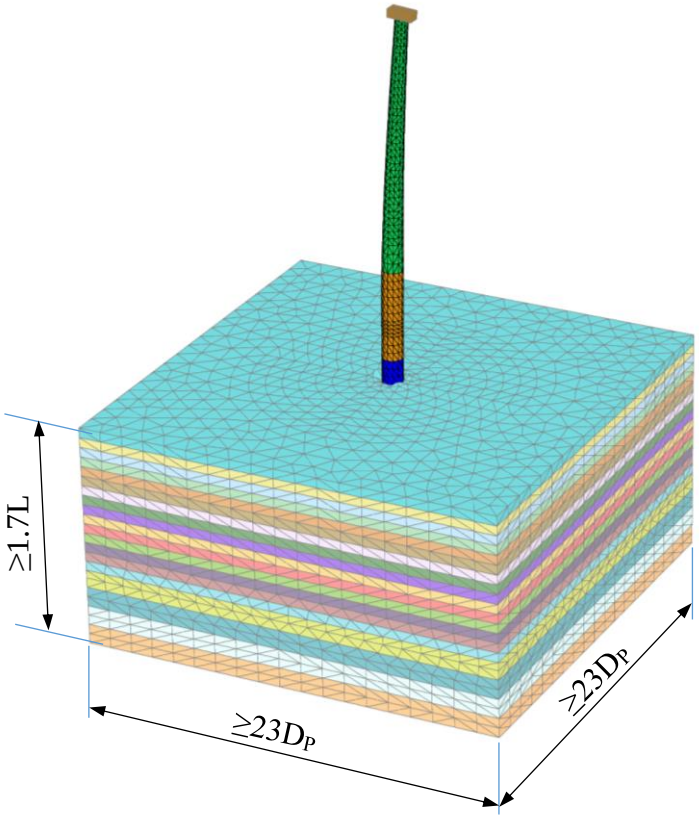

Figure 3.8. Typical model for dynamic analysis

System damped first frequency, $f_{1,d}$, which corresponds to total damping ratio, ξ, is obtained by equation 3-42. $f_{1,d}$ is taken into comparison with measured operational frequency. Alternatively, $f_{1,d}$ is expressed as a fraction of natural frequency of fixed base system, $f_{1,FB}$, by using foundation rigidity coefficient λ as in equation 3-43

$$A_x(t) = A_o \exp(-\xi_{fdn}\omega_{1,S}t) \quad (3\text{-}41)$$

$$f_{1,d} = f_{1,S}\sqrt{\frac{1-\xi^2}{1-\xi_{fdn}^2}} \quad (3\text{-}42)$$

$$\lambda = \frac{f_{1,d}}{f_{1,FB}} \qquad (3\text{-}43)$$

where: A_x (t) and A_o is the function and maximum acceleration/displacement amplitude for determining ξ_{fdn}, and $\omega_{1,S} = 2\pi f_{1,S}$.

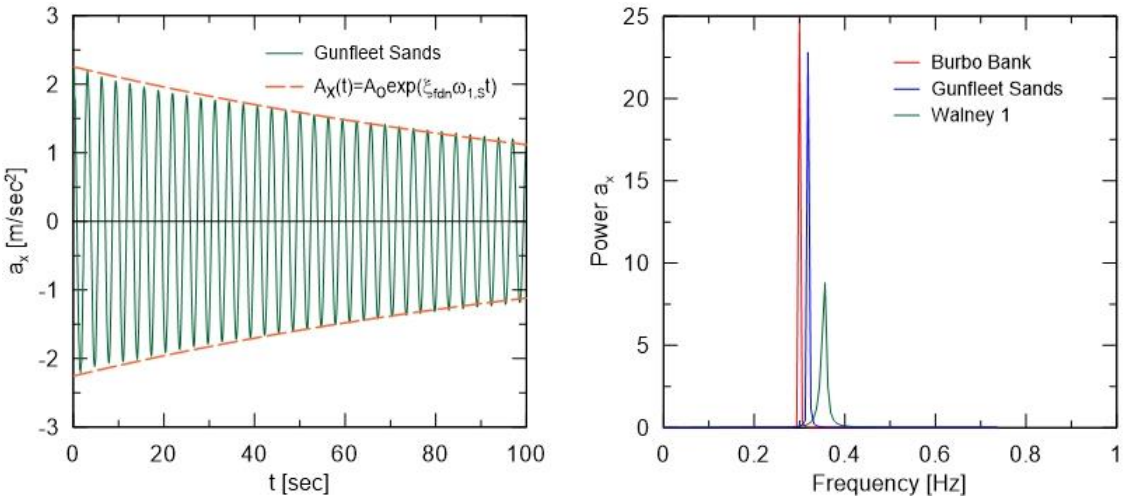

Figure 3.9. Time history of lateral acceleration at turbine level of Gunfleet Sands (left) and determination of $f_{1,S}$ by power energy spectrum of lateral acceleration for 3 projects (right).

3.7. Model calibration results

3.7.1. Model Calibration.

The results of dynamic analyses for model calibration are presented in Table 3.6. Foundation damping ratios are in range reported by Arany, et al. (2016) and Chen and Duffour (2018). By using average values recommended for other damping components, total damping is approximated as $\xi = 5\% + \xi_{fdn}$. The values of system damped frequency obtained from numerical analyses and equation 3-42 are less than 3% difference in magnitude from the measured values reported for the projects in literature.

3.7.2. Effect of ground loading history assumption

Assumption on ground loading history affects the input of soil properties, initial stress condition, and thus outcomes of numerical analyses (as described in Chapter 2). To assess impact of this factor to dynamic characteristics, another set of analyses are performed on the wind turbines for calibration with assumption of that the ground is normally consolidated

(NC). OCR=1 and K_0=0.4 is chosen for NC assumption while the calibration is done with assumption of that the ground is overconsolidated (OC) at relative density of 75% and 100%, and OCR and K_0 at depths are computed by equations 3-28 and 3-29.

Table 3.6. Results of simulations for model calibration.

Parameter	Symbol	Unit	Burbo Bank	Walney 1	Gunfleet Sands
First frequency by analysis	$f_{1,S}$	Hz	0.300	0.353	0.319
Foundation damping	ξ_{fdn}	%	0.56	0.45	0.35
Total damping	ξ	%	5.2	6.2	5.35
System damped frequency	$f_{1,d}$	Hz	0.299	0.352	0.318
Measured frequency	f_{meas}	Hz	0.292	0.350	0.314
Error	-	%	+2.7	+0.9	+1.6

The differences in input of G_o^{ref} and σ'_3 are shown in Figure 3.10a. The outcomes show that analyses with NC soil generally yield larger natural frequency and foundation damping ratio that those resulted from OC assumptions (Table 3.8 and Figure 3.10b). These results also lead to larger errors in comparison with measured data. Therefore, it can be concluded that simulations with consideration of soil stress history (OC assumption) provide more accurate results for three selected projects.

Table 3.7. Results of simulations with NC soil.

Parameter	Unit	Burbo Bank	Walney 1	Gunfleet Sands
First frequency by analysis	Hz	0.300	0.356	0.325
Foundation damping	%	0.8	1.2	0.8

3.8. Parametric study results

3.8.1. Natural frequency of fixed base system

The first natural frequency of fixed base system is determined by modal analysis in SAP2000 software. The numerical results are compared with analytical values obtained from

equations 3-3 to 3-5 by Arany, et al. (2016). Change in values of the frequencies with various pile diameters resulted from two methods is presented in Table 3.8. The results show that using monopile diameter D_P in equation 3-6 underestimates $f_{1,FB}$ and more accurate values are obtained by using D_S for calculation.

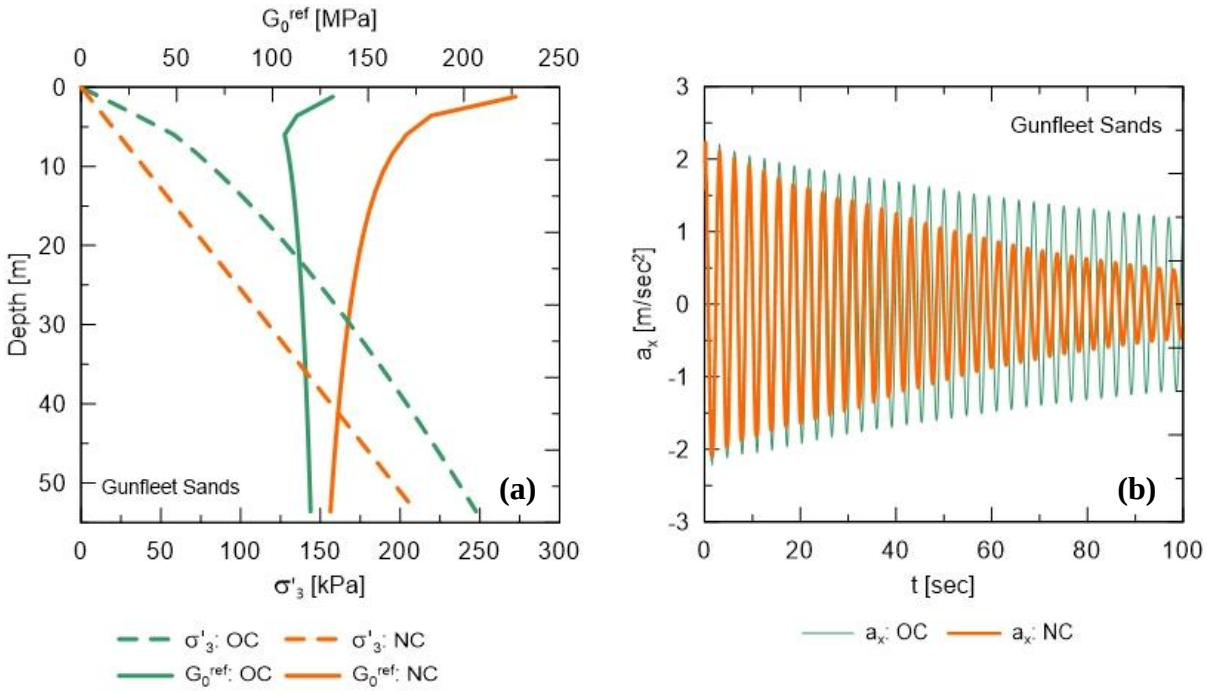

Figure 3.10. Comparison of input and output of analyses with NC and OC soil: (a) - G_o^{ref} , and initial σ_3' and (b) - obtained a_x.

Table 3.8. Fixed base system first natural frequency, $f_{1,FB}$

Method	Unit	D_P=5.0m	D_P=4.7m	D_P=4.4m	D_P=4.0m
FEM	Hz	0.369	0.353	0.335	0.308
Eq. 3-6 with D_P	Hz	0.333	0.319	0.304	0.282
Eq. 3-6 with D_S	Hz	0.348	0.337	0.324	0.304

3.8.2. Impact of pile embedded length on natural frequency and foundation damping

Effect of L_P (or ratio of L_P/D_P) on values of $f_{1,d}$ and foundation rigidity coefficient $\lambda=f_{1,d}/f_{1,FB}$ is illustrated in Figure 3.11. In general, as L_P decrease by about a half, from 38m to 19.2m, insignificant decline in $f_{1,d}$ and λ (by up to 2.2%) is observed. An opposite trend,

with higher rate, is shown for foundation damping with the same decline in L_P (Figure 3.12). The variations in $f_{1,d}$ and ξ_{fdn} are larger in soil with lower D_R. The changes are at a greater rate when L_P drops below a certain value of L_P for every case, indicating a shift in pile behavior. That value is associate with critical embedded length for constant displacement.

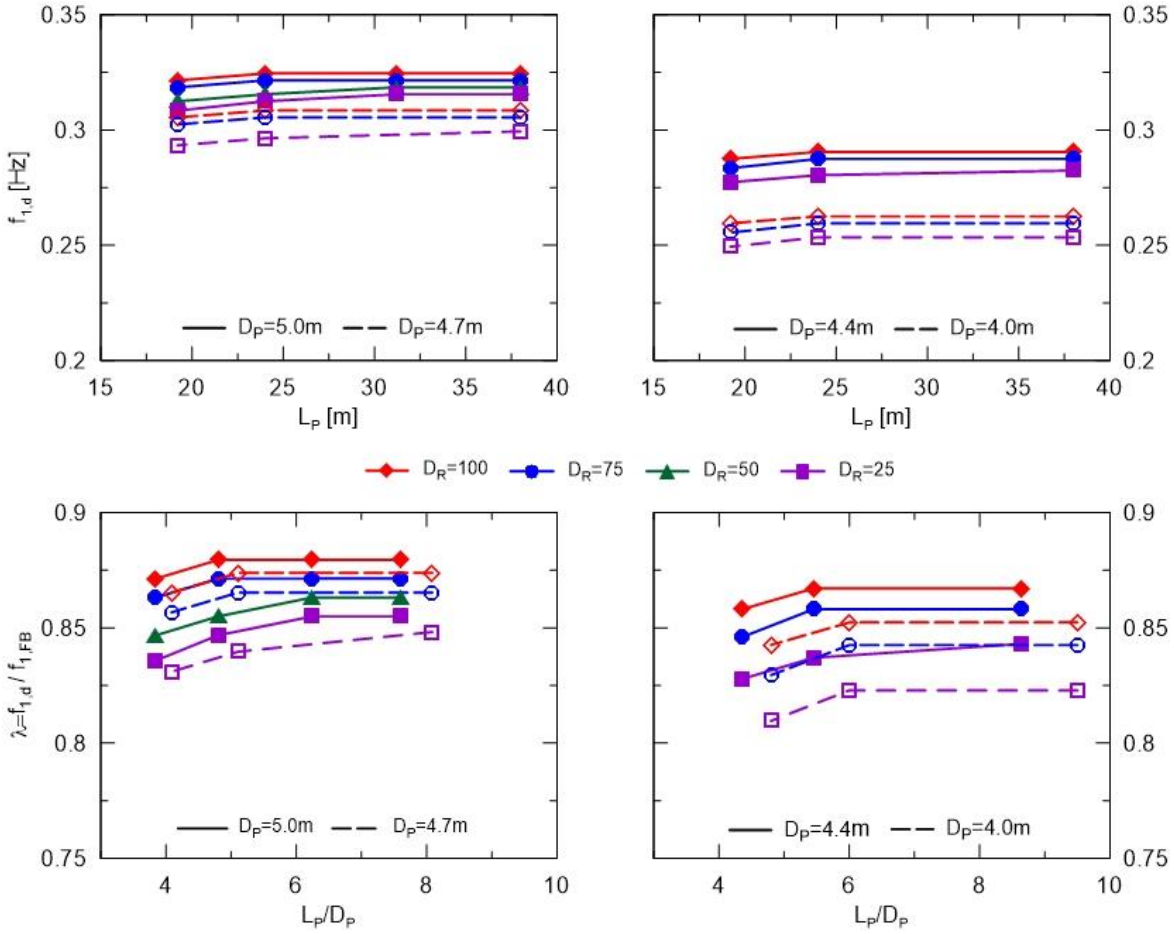

Figure 3.11. Effect of monopile embedded length on system first natural frequency.

3.8.3. Impact of pile diameter on natural frequency and foundation damping

Monopile diameter, D_P, appears to be more influential to natural frequency, $f_{1,d}$,and foundation damping ratio, ξ_{fdn} (Figure 3.13 and Figure 3.14). For a certain embedded length, as D_P decreases from 5.0m to 4.0m, $f_{1,d}$ drops by up to 20%, and the response is almost linear, especially for soil at relative densities of 100% and 75%. The change is slightly larger for stiffer soil. However, this change includes the variations in stiffness of the superstructure, which is reflected in reduction in values of $f_{1,FB}$ as D_P declines, and foundation rigidity. Coefficient λ only comes down by up to 3.3% with the same decrease in

D_P, and the decrease is greater for pile embedded in denser soil.

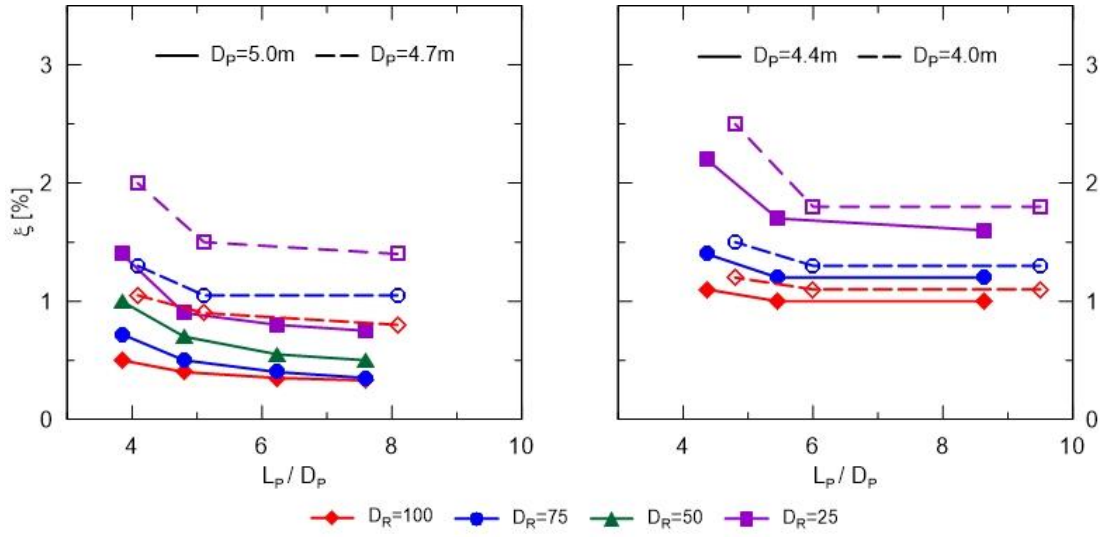

Figure 3.12. Effect of monopile embedded length on foundation damping

ξ_{fdn} appears to be more sensitive than $f_{1,d}$ to change in monopile diameter. In all cases, ξ_{fdn} increases at higher rate when D_P decreases from 5.0 to 4.7m and then more gradually with D_P declining further. For piles with L_P of 38m to 24m in soil with D_R from 75% to 100% ξ_{fdn} rises from less than 0.5% to about 1.5%. Change in ξ_{fdn} is larger in softer soil.

3.8.4. Comparison of obtained results with previous studies' outcomes

The parametric study's results have some finding in agreement with previous studies by Arany, et al. (2016) and Álamo, et al. (2018)

- ξ_{fdn} is more sensitive to changes in pile dimensions than $f_{1,d}$,
- Pile embedment, L_P, is less impactful than pile diameter, D_P, on $f_{1,d}$ and ξ_{fdn},

Another set of $f_{1,d}$ are determined for the monopiles analyzed in parametric study by the equations (3.2) to (3-16) developed by Arany, et al. (2016). The input for the calculation including unit weight and coefficient of lateral subgrade reaction k_h are presented in Table 3.9. The values of saturated unit weight, γ_{sat}, at chosen D_R are identical to those in numerical analysis. Effective unit weight, γ', is used in computing k_h per recommendation of (Terzaghi, 1955). The natural frequency is calculated for monopiles that are categorized as non-rigid ($\beta L_P \geq 1.5$). Frequency of fixed base system, $f_{1,FB}$, is shown in Table 3.8, while foundation

rigidity coefficient is computed as C_L x C_R. The results are compared with finite element simulation outcomes in Figure 2.13.

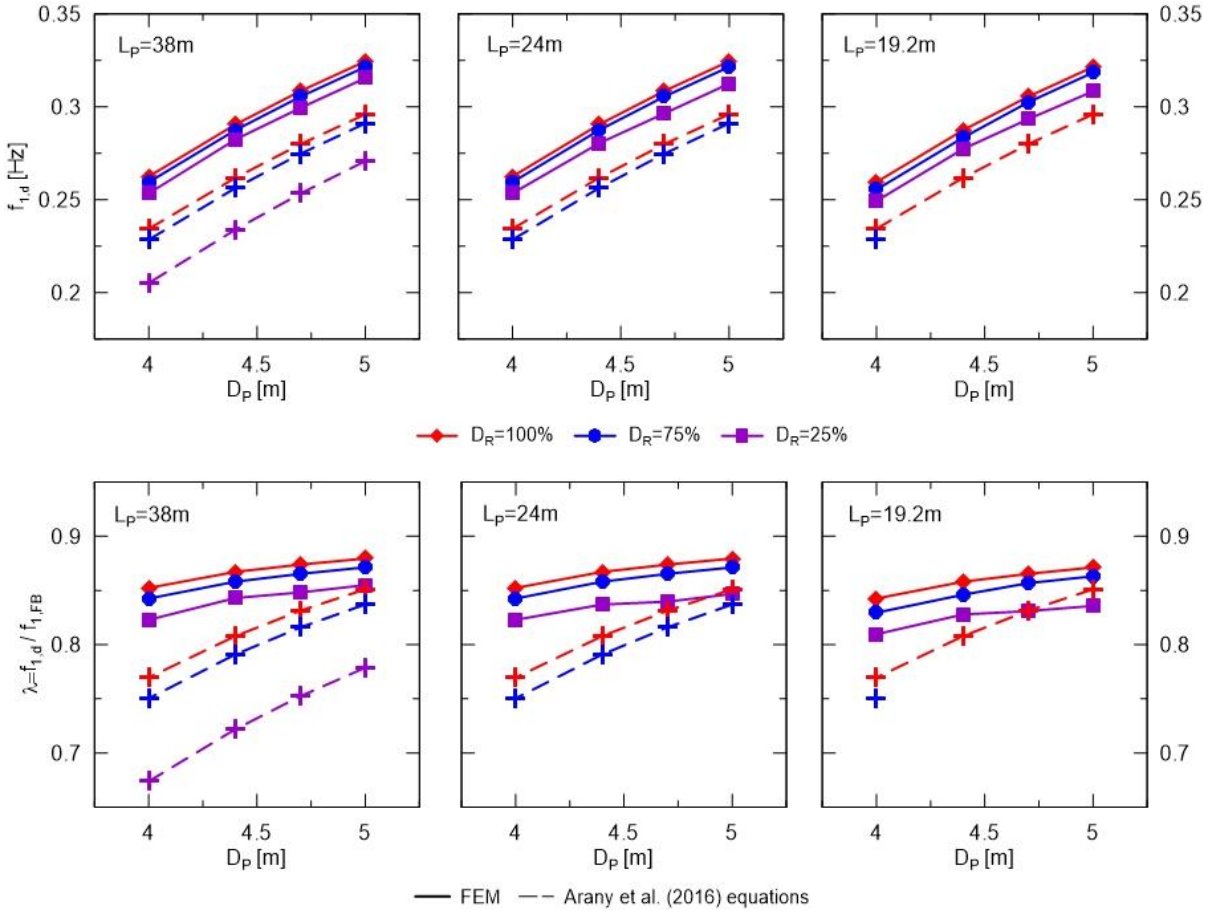

Figure 3.13. Effect of monopile diameter on system first natural frequency resulted from FEM and equations by Arany, et al. (2016).

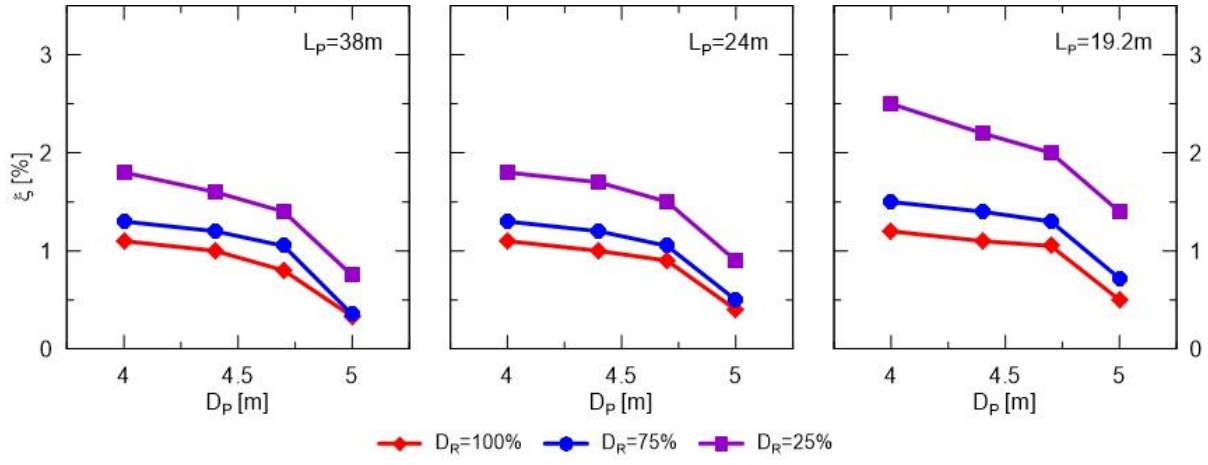

Figure 3.14. Effect of monopile diameter on foundation damping

Arany, et al. (2016) equations yield $f_{1,d}$ consistently lower than FE analyses results. The D_P- $f_{1,d}$ relationship obtained in both methods are almost linear with similar slope. The difference results from lower values of $f_{1,FB}$ and λ by Arany, et al. (2016) equations. In term of λ, both methods have similar values at D_P=5m, and D_R=100% and 75%, which is the conditions for model validation. But the results differ from each other when pile dimensions and soil properties move away from calibrated states.

Since in the chosen set of equations for non-rigid pile, embedded length has no role in calculation of λ and $f_{1,d}$, the results are the same as long as the embedded length yields $\beta L_P \geq 1.5$. The change in $f_{1,d}$ is dependent on variations in D_P (in form of pile section E_PI_P) and soil D_R (in forms of γ' and k_h). The k_h at D_R=100% is about 9 times as many as value at D_R=25% (Table 3.9) while the level of difference in Go for numerical analysis is not as many (Figure 3.4). That is likely the reason for narrower gap in natural frequency in FE results than in Arany, et al. (2016) method as soil D_R drops from 100% to 25%.

Table 3.9. Soil parameters for closed-form solution for natural frequency

D_R	**25%**	**50%**	**75%**	**100%**
γ_{sat} (kN/m^3)	19.4	19.8	20.2	20.6
γ' (kN/m^3)	9.59	9.99	10.39	10.79
k_h (kN/m^3)	1,787	4,888	9,734	15,985

3.9. Discussion on obtained results

3.9.1. Obtained results in design context

It is important to examine the results of parametric study in context of monopile design. The monopile dimensions for the offshore wind turbine at Gunfleet Sands wind farm, L_P=38m, D_P=5m were likely selected based on ULS and SLS criteria and critical load combinations (extreme wind or extreme wave). The dynamic analyses for natural frequency are performed with the excitation loads corresponding to normal and operational condition. Therefore, the monopile foundations in parametric study with smaller dimensions yield the results showing that the foundations are still considered as stiff. The foundation rigidity coefficient is in range from 0.81 to 0.88, of which the pile with D_P=5m and L_P=38m has λ=0.85-0.88 in soil with D_R=25%-100%.

The obtained minimum $f_{1,d}$ = 0.25Hz is larger than $f_{3P,min}$=0.231Hz while maximum value of 0.325Hz is lower than $f_{3P,max}$=0.6Hz. That means for this wind turbines, $f_{1,d}$ is in the frequency range of the dynamic load caused by passing blades (3P) and the system operates in the interval between soft-stiff and stiff-stiff (see Figure 3.1). It is obviously outside the soft-stiff zone recommended by DNV (2002). Change in tower dimensions is required to bring the $f_{1,d}$ to the recommended soft-stiff region.

3P loading has little contribution in total lateral load and bending moment at mudline (Arany, et al., 2015b). Moreover, since the priority is to avoid resonance and amplification of wave load, which has significantly larger impact, in cross-wind direction that has much lower damping, the upper limit of $0.9f_{3P,min}$ for $f_{1,d}$ seems not necessary and, in fact, could be impractical. The requirement of $f_{1,d} \geq 1.1f_{1P,max}$ is more suitable and of necessity.

3.9.2. Dynamic amplification factor of wave load

The system natural frequency and damping affect the dynamic interaction between the structure and each of the dynamic load acting on it. Amplitude of a dynamic load is amplified as natural frequency of the wind turbines is getting closer to frequency of excitation load. System damping, in contrast, dissipates the vibration energy and hinders the amplification and resonance. Dynamic amplification factor (DAF) is computed as in equation 3-44 (Gil-Martín, et al., 2012)

$$DAF = \frac{1}{\sqrt{\left(1-(f/f_{1,d})^2\right)^2 + \left(2\xi f/f_{1,d}\right)^2}} \qquad (3\text{-}44)$$

where f is frequency of excitation load, $f_{1,d}$ and ξ are system natural frequency and damping ratio, respectively.

Figure 3.15 compares values of DAF for normal and operational loading scenario at various pile dimensions and soil relative density that are considered in the parametric study, and values of wave load with and without DAF in those cases. It can be seen that D_P has larger influence on DAF than L_P and soil D_R. DAF is also larger in system with lower $f_{1,d,}$ which has smaller diameter and/or embedment. Therefore, when system natural frequency is underestimated, not only larger dimensions of monopile are selected but also larger wave load on the structure is used in analyses. The actual monopile will have surplus capacity as

the demand is lower than that in design. It is noteworthy that values of DAF are smaller in extreme wave and extreme wind conditions listed in Table 3.1 as wave periods in those scenarios are larger (smaller excitation frequency) (Table 3.3).

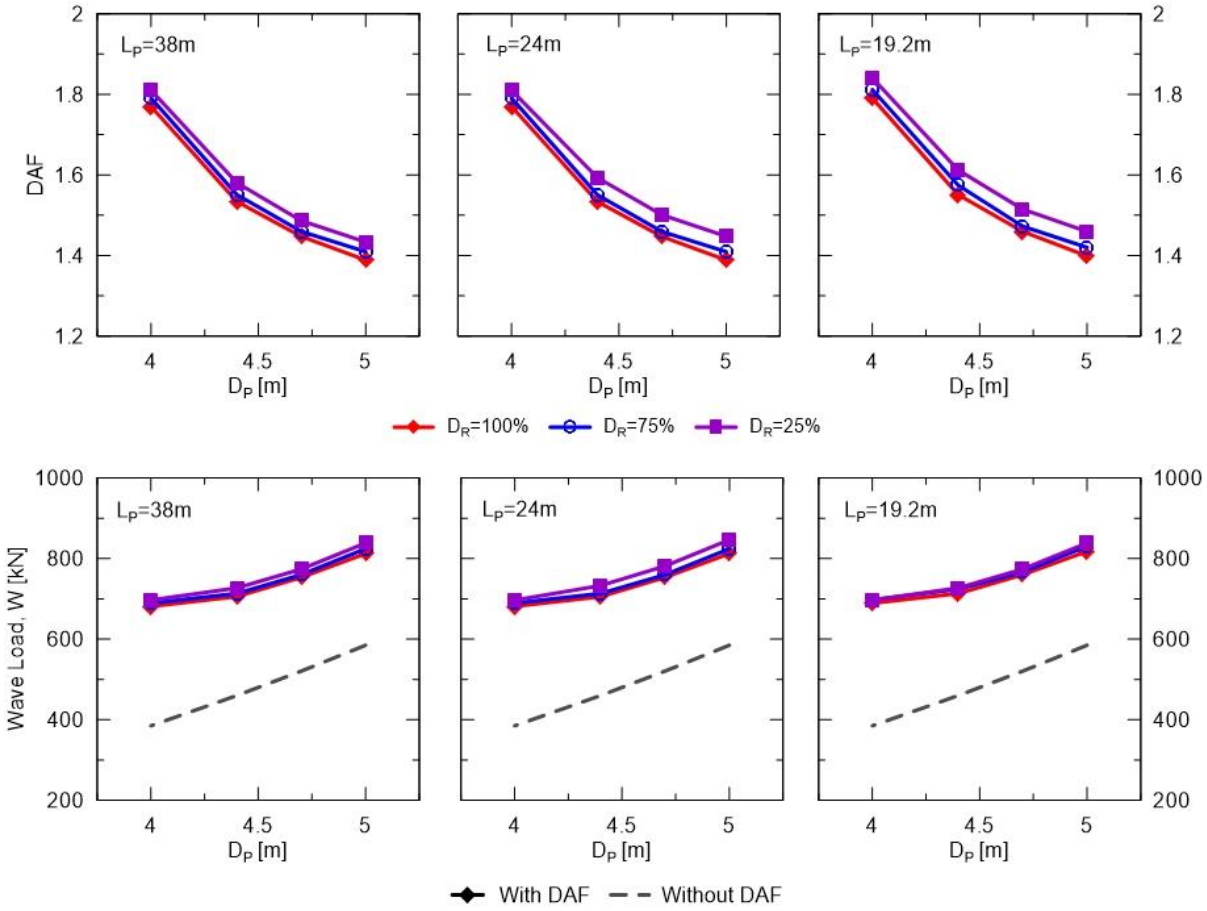

Figure 3.15. DAF and magnitude of wave load in normal and operational condition on monopile wind turbine at various pile diameter, embedded length, and soil D_R.

3.9.3. Role of critical embedment

The effect of embedded length on natural frequency $f_{1,d}$ can be reasoned by assessing the pile displacement profiles under the excitation (Figure 3.16). For pile with D_P=5m, the embedment of 38m is larger than zero toe-kick length ($L_{c,ztk}$) and $L_{c,cont}$ is about 24m in soil with D_R=100% and 75%. Therefore, when L_P decreases from 38m to 24m in soil with D_R=100% and 75%, displacement profile changes slightly and mostly occurs below rotational point, resulting in similar values of $f_{1,d}$ (Figure 3.11). Change in $f_{1,d}$ is only significant when $L_P < L_{c,cont}$ and corresponds to a profile that has consistently larger

displacement along pile length. Similar pattern is observed in soil with D_R=50% and 25% where $L_{c,cont}$ is in between 24m and 38m and $L_{c,ztk}$ is larger than 38m. The level of change in displacement profile regarding to decreasing L_P is greater with looser sand which is consistent to the observed larger change in $f_{1,d}$ in softer soil.

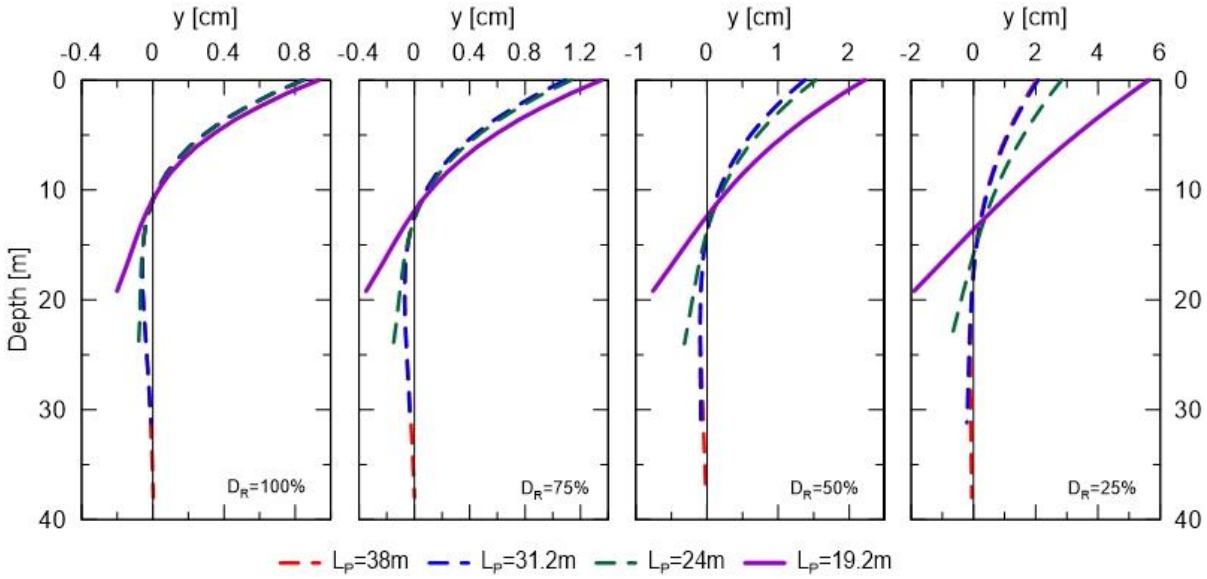

Figure 3.16. Displacement profiles caused by excitation loads for pile with D_P=5m and various lengths of embedment in different soil relative densities

3.10. Conclusions

The influences of monopile dimensions and soil condition on offshore wind turbine natural frequency and foundation damping are addressed in this paper. Numerical dynamic analyses are performed on three existing projects on sandy ground to validate the soil model parameters. Parametric study then is conducted on one project with varied pile embedment and diameter, and soil relative density. Soil properties are computed from empirical correlations with CPT cone resistance, q_c, generated by q_c-D_R relation by Jamiolkowsky, et al. (1985). Soil loading history parameters are included simulation and the selected soil constitutive model (HSsmall) captures soil hysteretic behavior. Natural frequency is determined by generating Fourier Transformation-based energy spectral density of the lateral acceleration time series. The foundation damping is defined by the decay in amplitude in the obtained acceleration record. Conclusions drawn from this study are presensented as follows:

- The simulations successfully estimate natural frequency of three existing offshore

wind turbines with the errors less than 3% of measured data. The obtained foundation damping ratios for the projects are within the common range reported by previous studies.

- Simulations that consider soil loading history (OCR, K_0) appear to provide more accurate prediction of natural frequency for calibrated projects.
- Parametric study with pile diameter D_P=5m, 4.7m, 4.4m, and 4.0m, pile embedded length L_P=38m, 31.2m, 24m, and 19.2, and soil relative density D_R=100%, 75%, 50% and 25% yields natural frequency in range of 0.252 to 0.325, which is within the frequency range of blades passing load 3P and outside the recommended soft-stiff zone for design. $f_{1,d}$ of monopile wind turbines is from 82% to 88% of $f_{1,FB}$ of the corresponding fixed-base structure.
- To reach the frequency of soft-stiff zone, reduction in dimensions of the tower is needed. The results imply that the upper frequency limit of 0.9 $f_{3P,min}$ could be impractical and unnecessary based on the influences of 3P and wave loads and the larger risk of fatigue damages in cross-wind direction.
- Overall, natural frequency decrease by up to 2.2% as L_P drops from 38m to 19,2m, while D_P and soil D_R are constant. In most cases, majority of the reduction occurs when L_P changes from 24m to 19.2m. Larger change is observed in softer soil. L_P=38 is closed to zero toe-kick ($L_{c,ztk}$) of the D_P=5m diameter pile in all selected soil conditions, while L_P=25 is approximate and just lower the constant displacement depth ($L_{c,const}$) for dense (D_R=100% and 75%) and medium to loose sand (D_R=50% and 25%), respectively. Therefore, larger rate of change in $f_{1,d}$ is observed when L_P is shorter than $L_{c,const}$. Similar pattern is observed in ξ_{fdn}.
- Change in pile diameter has larger impact on $f_{1,d}$ and ξ_{fdn} than variation of embedded length. The D_P-$f_{1,d}$ relation appears to be almost linearly proportional as D_P increase from 4.0m to 5.0m. The variation in $f_{1,d}$ comprises of changes in $f_{1,B}$ and foundation rigidity and the former has larger contribution. For a certain embedment L_P and soil D_R, λ increases by up to 4.2% within that range of D_P, and larger change is recorded in denser soil.

- Dynamic amplification factor (DAF) of wave load increases with decreasing $f_{1,d}$ and pile D_P appears to be the most influential element on change in DAF. DAF of wave load varies from about 1.4 to 1.8 as D_P decreases from 5.0m to 4.0m for in normal and operational loading scenario.

CHAPTER 4: APPROACHES FOR DETERMINING NATURAL FREQUENCY AND FOUNDATION DAMPING OF MONOPILE-SUPPORTED WIND TURBINE AND HYBRID WIND WAVE SYSTEM.

Abstract

Two approaches to correlate pile lateral displacement, y_o, and rotation, θ_o, at seabed level to offshore wind turbine natural frequency $f_{1,d}$, and foundation damping, ξ_{fnd}, are developed in this study. Regression analysis shows that foundation rigidity coefficient $\lambda = f_{1,d}/f_{1,FB}$ are best correlated to normalized displacement y_o/D_P while ξ_{fnd} has strongest correlation to θ_o. The derived relationships estimate well natural frequency of existing wind turbines and results of numerical dynamic simulation of monopile-supported wind turbines with presence of local scour and hybrid system. Impacts on local scour and added hydrokinetic (MHK) devices on system dynamic characteristics are evaluated. Role of critical embedment for constant displacement, $L_{c,const}$, on effect of local scour and recommendation on value of soil modulus in established formulae for foundation stiffness, K_L, K_R, and K_{RL}, are discussed.

4.1. Introduction

Developing diversity and combination across marine energy resources is necessary for sustainable development offshore renewable energy. Integrated systems can be attractive deployment options since they optimize exploitation of wave and wind energies in same marine area and the costs for infrastructure (Pérez-Collazo, et al., 2015). As such, the levelized cost of electricity (LCOE) of combined marine energy system can be significantly improved in comparison with stand-alone wind and wave energy farms (Astariz, et al., 2015). Therefore, the opportunity to deploy wave and current devices integrated with offshore wind farms can enhance economic viability of wave energy and propel the MHK industry into expedient deployment and operation of full-scale arrays.

A hybrid system combines wind turbine and wave and/or current converters on shared structure and anchoring. Since monopile has been the most common foundation selection for wind turbines, forming hybrid system by mounting wave or/and tidal energy converters on existing or new monopile wind turbines is a reasonable concept (Pérez-Collazo, et al., 2015, Perez and Iglesias, 2012). However, there have been no studies on engineering aspects of the hybrid structures

Monopile wind turbine is a dynamically sensitive structure. It its due to its form as a slender column with a rotating mass on top and dynamic nature of the loads acting on monopile (wind, wave, operating rotor, and passing blades). Since the loads have varying frequency in range from 0.01Hz to 1Hz (Bhattacharya, et al., 2011) and recommended design frequency in the narrow *soft-stiff* zone by DNV (2002), resonance and load amplification are primary concerns (Figure 3.1). Accuracy of f_1 and system damping estimations, therefore, is crucial for evaluations of load ampilification/resonance and consequent risk of fatigue damages in structure.

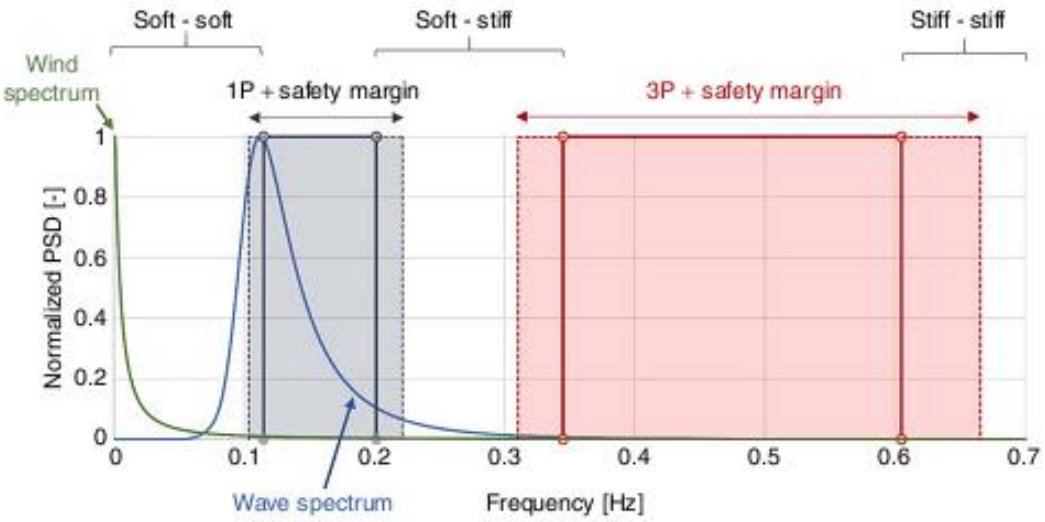

Figure 4.1. Normalized power spectral density (PSD) and frequency ranges of loads acting on offshore wind turbine system (Bhattacharya, 2019).

Predicting long-term dynamic performance is one of the biggest challenge in offshore monopile wind turbines design (Bhattacharya, 2014). It comes from many factors, such as change of soi properties under large number of cyclic load and/or development of global and local scour over time due to wave and current activities (Zanke, et al., 2011). There have been numerous studies on effect of scour on wind turbine natural frequency (Prendergast, et al., 2015, Prendergast, et al., 2013, Sørensen and Ibsen, 2013); however, impact on foundation damping is not adequately investigated.

Natural frequency is determined by finding Eigen value solutions for the system of discrete lumped masses, beam elements and springs for soil stiffness. Soil domain can be described as distributed springs (Cook and Vandiver, 1982, Damgaard, et al., 2013,

Prendergast, et al., 2015, Sørensen and Ibsen, 2013). Alternatively, whole the foundation, consisting of embedded pile and soil, is lumped as a set of springs at mudline level (Arany, et al., 2016, Bhattacharya, et al., 2013, Carswell, et al., 2015, Zaaijer, 2006, Zania, 2014, Zuo, et al., 2018). Foundation damping components are typically described as viscous dashpots.

Damgaard, et al. (2014) and Kallehave, et al. (2015a) find that f_1 of monopile wind turbines and is generally underpredicted. Moreover, it is reported by Germanischer Lloyd (2005), Damgaard, et al. (2013), Tarp-Johansen, et al. (2009), Versteijlen, et al. (2011) and Shirzadeh, et al. (2013) that foundation damping defined by existing literature has poor agreement with values back-calculated from measurements on full-scale wind turbines. That likely results from the facts of that soil damping for wind turbine foundation is insufficiently studied and of that soil damping, being hysteretic strain-dependent material damping (Carswell, et al., 2015, Cook and Vandiver, 1982), is normally described as constant or frequency-dependent viscous dashpots in common analyses (Álamo, et al., 2018, Carswell, et al., 2015, Chen and Duffour, 2018, Damgaard, et al., 2013, Shirzadeh, et al., 2013, Tarp-Johansen, et al., 2009, Versteijlen, et al., 2011, Zania, 2014).

Another approach is performing numerical dynamic analysis to capture system vibration following removal of load or displacement excitation. Natural frequency and damping can be defined by conducting spectral analysis on the lateral displacement, velocity, or acceleration response and curve-fitting the decay of the signal amplitudes, respectively (Đilas, 2018). This method requires an advanced soil constitutive model capturing soil cyclic behavior and hysteretic damping. However, the biggest challenge is the demand of significant computational resources.to achieve the desired accuracy.

This study, therefore, explores approaches to bridge the results on pile lateral displacement and rotation at seabed level caused by excitation load in static analyses to natural frequency and foundation damping obtained from dynamic analyses. The correlations are established based on the parametric study performed in Chapter 3 on impacts of soil relative density, and pile diameter and embedment on vibration characteristics. The correlations are applied to estimate natural frequency and foundation damping for monopile-supported wind turbines with local scour and hybrid systems. Outcomes by the correlations and FE simulations are compared to evaluate applicability the approaches.

4.2. Determination of natural frequency of monopile wind turbines

4.2.1. Numerical approaches for determining natural frequency of monopile wind turbines

Natural frequency of wind turbines can be estimated numerically, experimentally with scaled models, and by measurements on full-scale structure. The numerical modal analysis is commonly performed by finding Eigen value solutions for the system with discrete lumped masses. Soil domain is described as distributed springs (for stiffness) (Cook and Vandiver, 1982, Damgaard, et al., 2013, Prendergast, et al., 2015, Sørensen and Ibsen, 2013). American Petroleum Institute (API) p-y curves are widely used in this approach. Alternatively, in a simplified approach, the combined effect of in-ground portion of pile and soil domain is lumped as a set of springs at mudline level (Arany, et al., 2016, Bhattacharya, et al., 2013, Carswell, et al., 2015, Zaaijer, 2006, Zania, 2014, Zuo, et al., 2018). The springs represent foundation lateral (swaying) stiffness, K_L, rotational (rocking) stiffness, K_R, couple swaying-rocking stiffness, K_{LR}, and vertical stiffness, K_V. Vertical stiffness is not considered in natural frequency calculation; therefore, the approach is referred as 3-spring model. Foundation damping components are typically described as dashpots in addition to the springs to consider energy loss during vibration.

Major drawback of the approach using API p-y curves is underestimating f_1 (Kallehave, et al., 2015a, Kallehave, et al., 2012). The main reasons are that API p-y curves underestimate soil initial stiffness and have not been validated for piles with large diameter as of offshore monopiles (Kallehave, et al., 2012). For 3-spring model, several formulas for K_L, K_R, and K_{LR} have been proposed (Gazetas, 1984, Pender, 1993, Poulos and Davis, 1980, Randolph, 1981, Shadlou and Bhattacharya, 2016), however, evaluation of springs stiffnesses is not straightforward due to following reasons:

- The formulae are developed for homogeneous ground with constant or linearly distributed or parabolically distributed soil modulus and pile behavior of either flexible or rigid. Spring stiffnesses for heterogeneous or layered ground are not defined.
- For flexible pile, out of pile dimensions, K_L, K_R, and K_{LR} depend utterly on pile

diameter, D_P. Meanwhile, K_L, K_R, and K_{LR} depend only on pile embedment, L_P, in case of rigid pile. Arany, et al. (2016) conclude that formulations for flexible pile are more suitable for monopiles, which are normally categorized as neither flexible nor rigid by the definitions by Poulos and Davis (1980) or by Randolph (1981) and Carter and Kulhawy (1992). More comprehensive descriptions of K_L, K_R, and K_{LR} including impacts of both D_P and L_P that cover all pile behaviors are needed.

- Soil stiffness used for K_L, K_R, and K_{LR} formulas is either lateral coefficient of subgrades reaction, k_h (Poulos and Davis, 1980), or Young modulus at depth of $1D_P$ below mudline, E_{S0} (Gazetas, 1984, Pender, 1993, Randolph, 1981, Shadlou and Bhattacharya, 2016). However, there are uncertainties in selecting E_{S0} by empirical correlation with in-situ tests data, such as SPT, CPT, and pressuremeter test – PMT (Shadlou and Bhattacharya, 2016)

Dynamic analysis to capture system vibration following removal of load or displacement excitation is another approach to determine system natural frequency. Spectral analysis on the lateral displacement, velocity, or acceleration response to determine the frequency peaks for the natural frequencies of modes of vibration (Đilas, 2018). Chapter 3 illustrates the capability of numerical dynamic analyses in estimating and examining natural frequency and foundation damping of monopile offshore wind turbines in various soil conditions and monopile configurations. However, this method requires an advanced soil constitutive model that can describe soil cyclic behavior and hysteretic damping, and significant computational resources.

4.2.2. Closed-formed solution for Eigen frequency by Arany, et al. (2016)

Arany, et al. (2016) developed a closed-form equation to estimate first natural frequency using a 3-spring model by applying foundation flexibility coefficients into the natural frequency of the same structure with fixed base. First natural frequency of an offshore wind turbines, which is supported by monopile foundations as described by Figure 3.3, can be estimated by equations from 3-45 to 3-56 (Arany, et al., 2016):

$$f_1 = C_L C_R f_{1,FB} = C_L C_R (C_S f_{FB,T}) \quad (3\text{-}45)$$

where: $f_{1,FB}$ is the fixed-base first natural frequency of the wind turbine structure, $f_{FB,T}$

is the fixed-base first natural frequency of the tower structure only, C_L and C_R are lateral and rotational foundation flexibility coefficients, and C_S is the substructure flexibility coefficient.

$$f_{FB,T} = \frac{1}{2\pi}\sqrt{\frac{3E_T I_T}{\left(m_{RNA} + \frac{33}{140}m_T\right)L^3}} \qquad (3\text{-}46)$$

where: m_{RNA} is the mass of rotor-nacelle assembly, m_T is the mass of the tower, L is the distance from tower bottom to rotor center, and

$$I_T = \frac{1}{8}\pi D_T^3 t_T \text{ is average tower section area moment of inertia} \qquad (3\text{-}47)$$

with t_T is the average tower wall thickness and $D_T=0.5(D_t+D_b)$ is the average tower diameter.

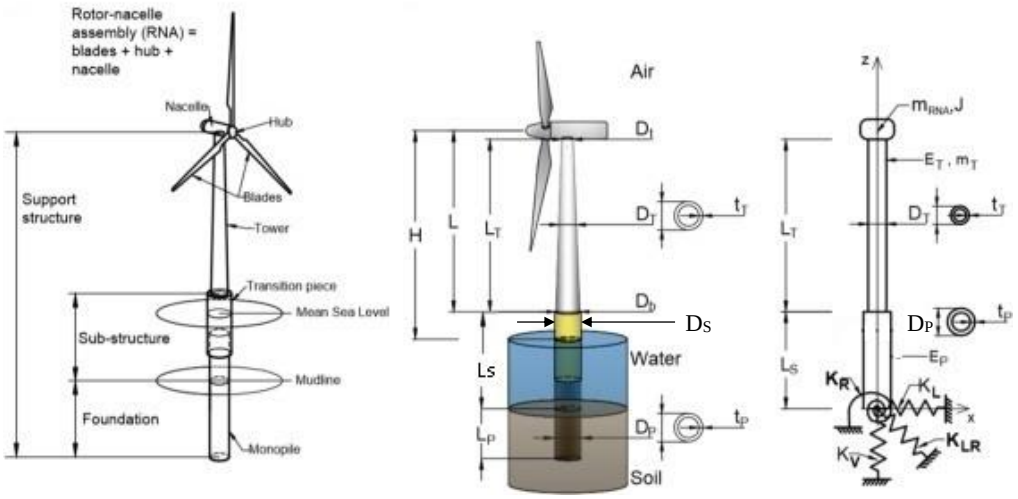

Figure 4.2. Terminology of wind turbine components and model (Arany, et al., 2016).

C_S reflects the effect of transition piece dimensions. C_L and C_R are formulated from K_L, K_R, and K_{LR}, which incorporate soil stiffness, pile embedded length and diameter, and tower flexural rigidity and dimensions.

$$C_S = \sqrt{\frac{1}{1+(1+\psi)^2\chi-\chi}} \qquad (3\text{-}48)$$

$$C_L(\eta_L,\eta_R,\eta_{LR}) = 1 - \frac{1}{1+0.5\left(\eta_L - \frac{\eta_{LR}^2}{\eta_R}\right)} \quad (3\text{-}49)$$

$$C_R(\eta_L,\eta_R,\eta_{LR}) = 1 - \frac{1}{1+0.6\left(\eta_R - \frac{\eta_{LR}^2}{\eta_L}\right)} \quad (3\text{-}50)$$

where: $\chi = \frac{E_T I_T}{E_P I_P}$ is bending stiffness ratio (3-51)

$\psi = \frac{L_S}{L_T}$ is transition piece/tower length ratio (3-52)

$\eta_L, \eta_R, \eta_{LR}$ are non-dimensional foundation stiffness

$$\eta_L = \frac{K_L L_T^3}{E_T I_\eta} \qquad \eta_{LR} = \frac{K_{LR} L_T^2}{E_T I_\eta} \qquad \eta_R = \frac{K_R L_T}{E_T I_\eta} \quad (3\text{-}53)$$

where: $E_P I_P$ is pile section flexural rigidity, L_T is length of the tower and $E_T I_\eta$ is the tower equivalent flexural rigidity considering change in tower cross section (diameter and wall thickness) over its length. For a tower that has linearly declining from D_b at bottom to D_t at top:

$$E_T I_\eta = f(q) E_T I_{top} \quad (3\text{-}54)$$

where:

$I_{top} = \frac{1}{8}\pi D_t^3 t_t$ is the moment of inertia of the section at tower top (3-55)

$$q = \frac{D_b}{D_t}; \qquad f(q) = \frac{2q^2(q-1)^3}{3(2q^2 \ln q - 3q^2 + 4q - q)} \quad (3\text{-}56)$$

This set of equations (3-45 to 3-56) is only suitable for monopiles that are categorized as non-rigid Arany, et al. (2016). Pile rigidity can be evaluated by slenderness parameter β recommended by Poulos and Davis (1980) (equation 3-57).

$$\beta = \sqrt[4]{\frac{k_h D_P}{4E_P I_P}} \tag{3-57}$$

where: D_P is pile outside diameter, and k_h is soil lateral subgrade reaction coefficient. Terzaghi's (1955) equation (3-58) for k_h is used in the study by Arany, et al. (2016)

$$k_h = A\frac{\gamma'}{1.35} \tag{3-58}$$

where: γ' is soil effective unit weight and A=100-300 for loose sand, A=300-1000 for medium sand, and A=1000-2000 for dense sand.

4.2.3. Monopile foundation stiffness

Under static load, pile displacement, y_o, and rotation, θ_o, at mudline can be determined from lateral load and overturning moment ($H_{y,o}$ and $M_{x,o}$) calculated at the same level, and foundation stiffness by equation 3-59.

$$\begin{bmatrix} H_{y,o} \\ M_{x,o} \end{bmatrix} = \begin{bmatrix} K_L & K_{LR} \\ K_{RL} & K_R \end{bmatrix} \begin{bmatrix} y_o \\ \theta_o \end{bmatrix} \tag{3-59}$$

where: K_L is foundation lateral stiffness (swaying), K_R is rotational stiffness (rocking), and $K_{LR} = K_{RL}$ is couple swaying-rocking stiffness.

For dynamic loads, the foundation is described by dynamic impedances in complex form (Gazetas, 1984)

$$K_{dyn} = K_{static}\left[k(\omega) + 2i\xi\right] \tag{3-60}$$

where: K_{static} is static stiffness in particular mode, k(ω) is frequency-dependent dynamic stiffness coefficient and ξ is foundation damping.

K_L, K_R, and K_{LR} incorporate soil stiffness, pile embedded length and diameter. The formulation for K_L, K_R, and K_{LR} is based on assumption on distribution of soil stiffness over depth (constant, linear or parabolic) and classification of pile behavior (flexible or rigid) (Carter and Kulhawy, 1992, Gazetas, 1984, Pender, 1993, Poulos and Davis, 1980, Randolph, 1981, Shadlou and Bhattacharya, 2016). For homogenous soil with parabolic soil modulus profile, the expressions for flexible and rigid piles by previous studies are

summarized in Table 4.1. The formulae show that K_L, K_R, and K_{LR} for flexible and rigid piles depend entirely on D_P and L_P, respectively. The soil modulus appearing in the equation is Young modulus at $1D_P$ below the mudline level, E_{S0}, and the modulus profile is defined by equation 3-61.

$$E_S(z) = E_{S0}\left(z/D_P\right)^{0.5} \tag{3-61}$$

Table 4.1. Established foundation static stiffness formulae for parabolic soil modulus profile

Author	Flexible pile	Rigid Pile
Gazetas, 1984	$K_L = 0.79 D_P E_{S0}\left(\frac{E_{eq}}{E_{S0}}\right)^{0.28}$ $K_{LR} = -0.24 D_P^2 E_{S0}\left(\frac{E_{eq}}{E_{S0}}\right)^{0.53}$ (3-62) $K_R = 0.15 D_P^3 E_{S0}\left(\frac{E_{eq}}{E_{S0}}\right)^{0.77}$	
Pender, 1993	$K_L = 0.735 D_P E_{S0}\left(\frac{E_{eq}}{E_{S0}}\right)^{0.33}$ $K_{LR} = -0.27 D_P^2 E_{S0}\left(\frac{E_{eq}}{E_{S0}}\right)^{0.55}$ (3-63) $K_R = 0.172 D_P^3 E_{S0}\left(\frac{E_{eq}}{E_{S0}}\right)^{0.776}$	
Shadlou and Bhattacharya, 2016	$K_L = \frac{1.02 D_P E_{S0}}{1+\lvert\nu_S - 0.25\rvert}\left(\frac{E_{eq}}{E_{S0}}\right)^{0.27}$ $K_{LR} = \frac{-0.29 D_P^2 E_{S0}}{1+\lvert\nu_S - 0.25\rvert}\left(\frac{E_{eq}}{E_{S0}}\right)^{0.52}$ (3-64) $K_R = \frac{0.17 D_P^3 E_{S0}}{1+\lvert\nu_S - 0.25\rvert}\left(\frac{E_{eq}}{E_{S0}}\right)^{0.76}$	$K_L = \frac{2.66 D_P E_{S0}}{1+\lvert\nu_S - 0.25\rvert}\left(\frac{L_P}{D_P}\right)^{1.07}$ $K_{LR} = \frac{-1.8 E_{S0}}{1+\lvert\nu_S - 0.25\rvert} L_P^2$ (3-65) $K_R = \frac{1.63 E_{S0}}{1+\lvert\nu_S - 0.25\rvert} L_P^3$
Definitions: • $E_{eq} = \frac{E_P I_P}{\left(\pi D_P^4 / 64\right)}$ (3-66) • $E_P I_P$ is pile section flexural rigidity, D_P is pile diameter • E_{S0} is soil Young modulus at depth of D_P; ν_S is soil Poisson ratio		

Using static K_L, K_R, and K_{LR} for determining Eigen frequency is reasonable. The level of accuracy depends on how well the representative value of soil modulus and the distribution of soil over depth are selected. For piles embedded in layered soil profile or in soil with presence of local scour, using the established equations for homogenous soil likely leads to many uncertainties and requires modification. An alternative option, which is explored in this paper, is to directly find K_L, K_R, and K_{LR} by solving a set of equations consisting of equation 3-59 and an assumption on relationship among K_L, K_R, and K_{LR}. The values of $H_{y,o}$ and $M_{x,o}$ are determined from excitatory wind thrust and wave load. Meanwhile y_o, and rotation θ_o are obtained from numerical simulation of the monopile wind turbines subjected to those loads prior to dynamic analysis for natural frequency and foundation damping.

4.2.4. Effects of soil relative density, pile embedded length, and pile diameter on monopile wind turbine natural frequency and foundation damping

In Chapter 3, numerical dynamic simulations are performed to study impacts of soil conditions and monopile configurations on natural frequency and foundation damping ratio of offshore monopile-supported wind turbines. The study is summarized as follows:

Firstly, the model is calibrated by matching analyses results on first natural frequency with measured data for three wind turbines at Burbo Bank, Walney 1 and Gunfleet Sands wind farms located in England. Obtained foundation damping is compared with commonly reported range as the measured data on damping is unavailable.

Subsequently, the parametric study is performed for the Gunfleet Sands wind turbine in many settings that are resulted from various combinations of pile diameter (D_P = 5.0m, 4.7m, 4.4m, and 4.0m), pile embedded length, and soil relative density. For each diameter, simulations are initially performed with L_P=38.0m, 24m, and 19.2m, and D_R=100%, 75%, and 25%. The largest changes in obtained natuaral frequency are -4.1% (from 0.315 to 0.308) when D_R declines from 100% to 25%, and -2.2% (from 0.322 to 0.308) when L_P decreases from 38m to 19.2m. Both largest variations happen with D_P=5.0m. Simulations at D_R=50% and L_P=31.2m are added to examine wether additional configurations are required. The additional results show that natual frequency for L_P=31.2m is almost identical to that at L_P=38.0m, and valuea for D_R=50% are very close to either those at D_R=75% or the mean of

values at D_R=75% and 25%. Therefore, simulations at L_P=31.2m and D_R=50% are not performed to other diameters.

Impacts of soil relative density, pile embedded length and pile diameter on natural frequency and foundation damping are presented in Figures 4.3 to 4.6. Foundation rigidity coefficient, λ, is introduced to describe how stiff the foundation system compared to perfectly fixed base structure (equation 3-67):

$$\lambda = f_{1,d} / f_{1,FB} \quad (3\text{-}67)$$

where: $f_{1,d}$ is the damped natural frequency of the monopile wind turbine resulted from simulation and $f_{1,FB}$ is the natural frequency of the wind turbine with fixed restraint at level of mudline.

The effects of soil D_R, and pile D_P and L_P are summarized below:

- For piles with certain D_P, decline in natural frequency happens when L_P falls below the critical embedded length for constant deformation, $L_{c,const}$. The decline is greater in softer soil since soil with lower D_R has larger value of $L_{c,const}$
- Foundation damping increases with declining system natural frequency. However. similar patterns in rate of change are recorded for foundation damping regrading to L_P and D_R as for natural frequency.
- For piles with certain L_P, as natural frequency increases with increasing pile D_P. The change in $f_{1,d}$ is lower in softer soil. This change is majorly contributed by the variation in $f_{1,FB}$ as D_P increases from 4.0m to 5.0m. λ increases while ξ_{fdn} decreases consistently as D_P rises from 4.0m to 5.0m.

The obtained data suggests that there is a correlation between λ and ξ_{fdn}. Moreover, as presented in equation 3-59, foundation stiffness depends on level of soil strains caused by lateral load and bending moment and is reflected in values of pile lateral displacement, y_o, and rotation, θ_o, at mudline. Establishing λ - ξ_{fdn}, y_o – λ, θ_o – λ, y_o – ξ_{fdn}, and θ_o – ξ_{fdn} relationships is the next step and they will be the baseline for finding the relations for wind turbines with presence of scour depth and monopole-supported hybrid systems.

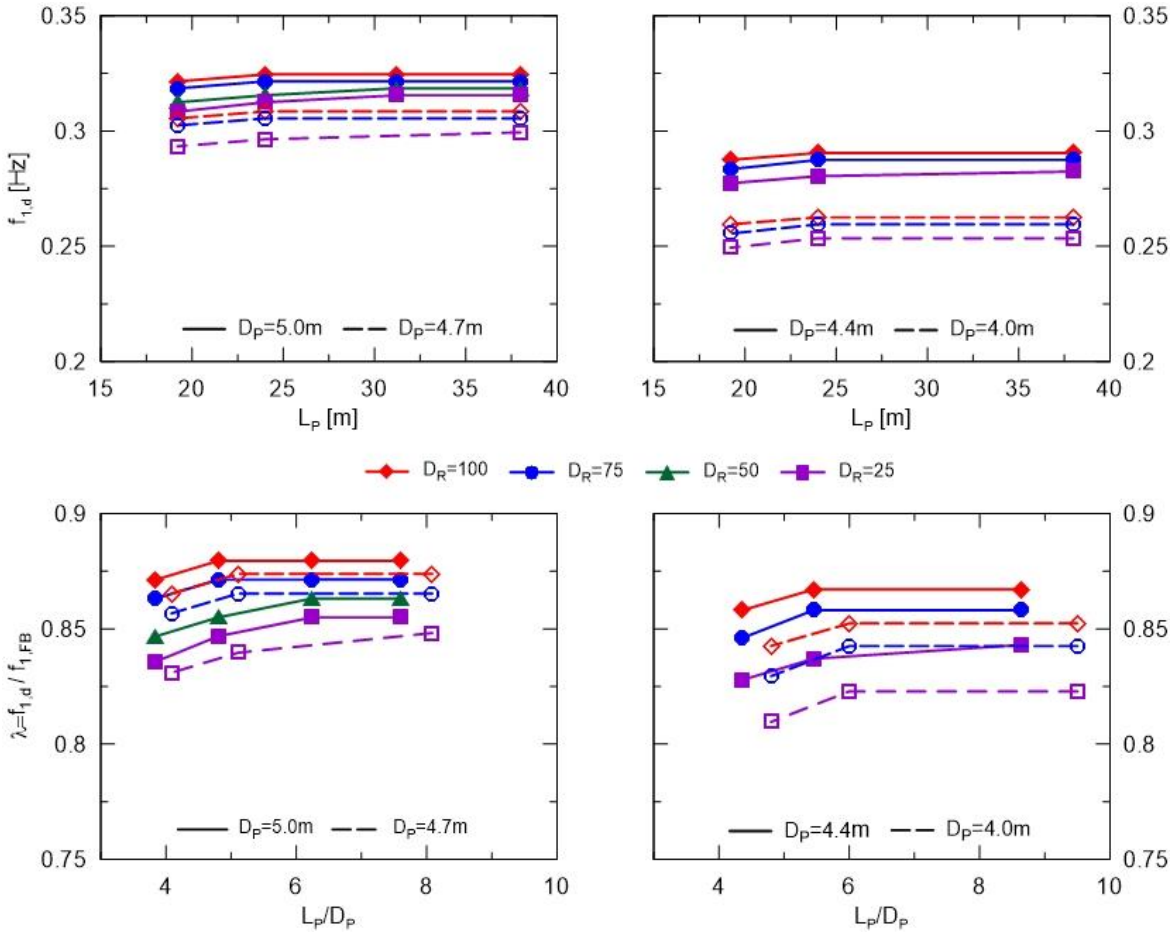

Figure 4.3. Effect of monopile embedded length on system first natural frequency

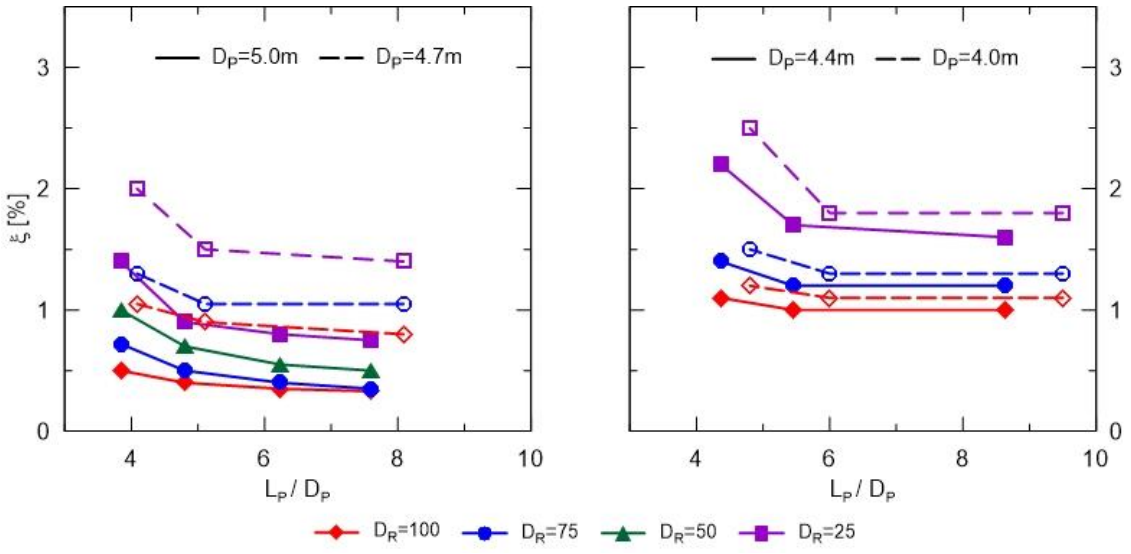

Figure 4.4. Effect of monopile embedded length on foundation damping

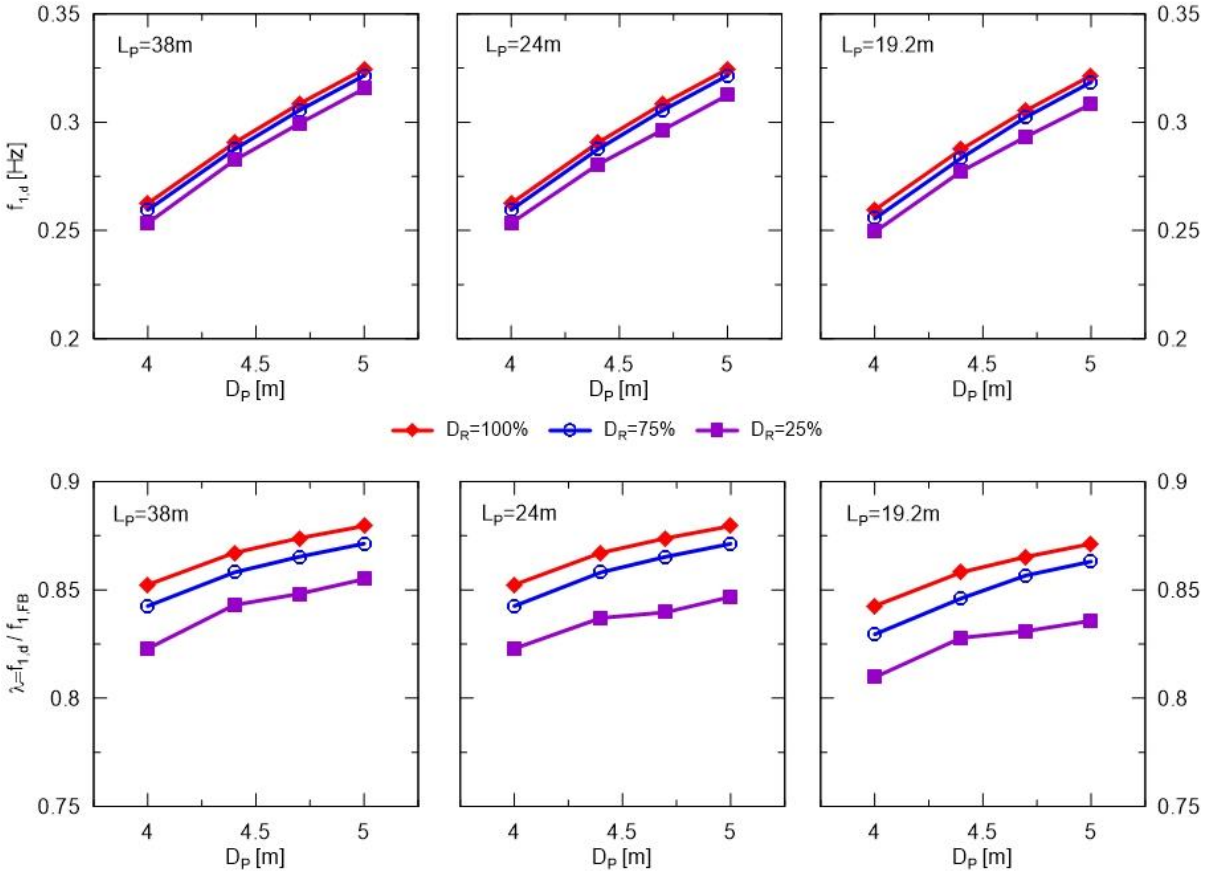

Figure 4.5. Effect of monopile diameter on system first natural frequency

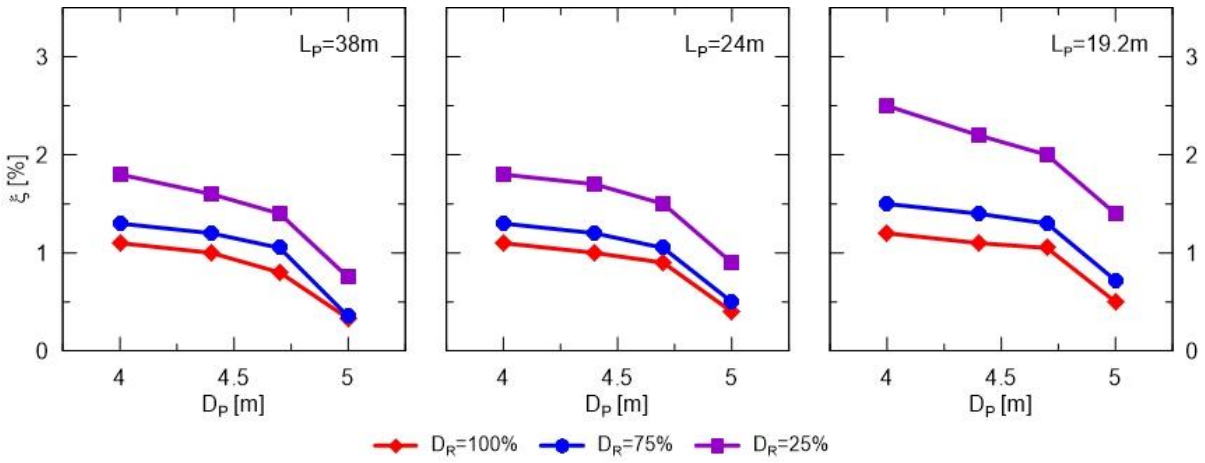

Figure 4.6. Effect of monopile diameter on foundation damping.

4.2.5. Effect of scour on natural frequency of monopile wind turbine

Foundation overall stiffness and thus system natural frequency vary over time with

development of global and/or local scour. Offshore wind turbine design code DNV (2014) recommends checking for local scour depth of $1.3D_P$ when scour protection layer is unavailable. For p-y curves, API (2008) uses reduced vertical effective stress due to global and local scour in calculating p_u (Figure 4.7) and reduced soil reaction modulus due to global scour. Lin, et al. (2010) take into consideration the influence of soil overconsolidation due to scour development on reaction modulus and p_u. However, in both approaches the ground is considered normally consolidated before the scour taking place. Furthermore, there have not been any recommendations on modifications of foundation stiffness, K_L, K_R, and K_{LR}, in 3-spring model with scour effects.

Sørensen and Ibsen (2013) and Prendergast, et al. (2015) apply API (2008) and Lin, et al. (2010) approaches, respectively, to examine impact of local scour depth on monopile wind turbine first natural frequency. In the former study, f_1 decreases by 5% as scour develops to the code-recommended depth of $1.3D_P$. The latter suggests a larger decline in f_1 than in Sørensen and Ibsen (2013) study, and that the level of reduction is greater in softer soil (Figure 4.8). However, effect of scour depth on foundation damping has not been investigated. In this paper, stress history of the ground prior to pile installation and change in soil OCR due to scour development are considered to examine the influence of local scour on system natural frequency and foundation damping.

This study is aimed to explore approaches to use lateral deflection and pile rotation at mudline level in determining natural frequency and foundation damping of monopile-supported wind turbines and hybrid system. The deformation at mudline, y_o and θ_o are resulted from numerical static analyses of the wind turbines under the excitation loads induced by wind and wave activities. One approach is to find the correlations by linking static and dynamic analyses outcomes. The other is to determine K_L, K_R, and K_{LR} for corresponding to y_o and θ_o and use those stiffnesses in equation by Arany, et al. (2016) to compute natural frequency. The correlations are determined for monopile-supported typical offshore wind turbine, turbine with presence of local scour, and hybrid wind-wave systems.

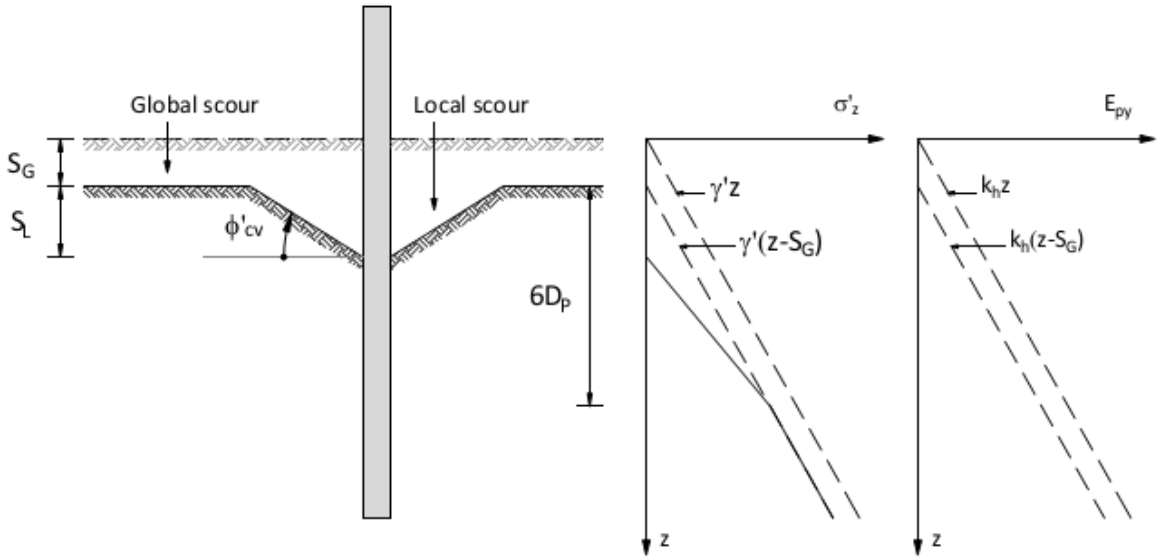

Figure 4.7. Modified vertical effective stress and reaction modulus E_{py} for API p-y curves in analyses with presence of global and local scour (API, 2008)

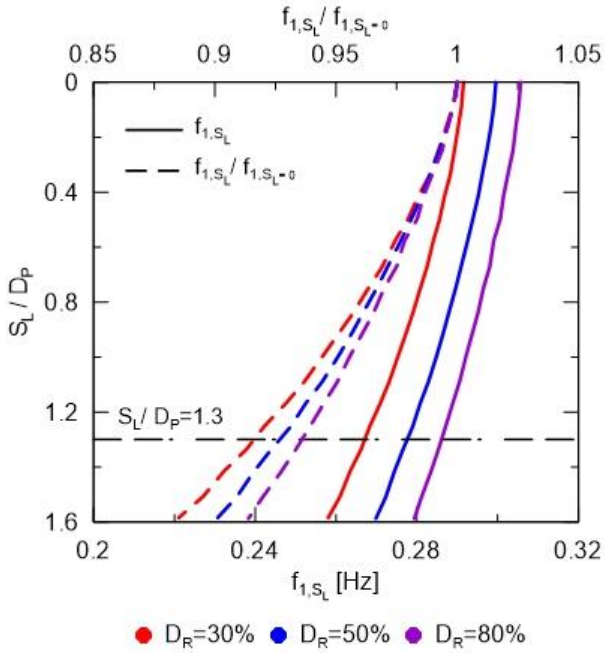

Figure 4.8. Influence of scour depth on offshore wind turbine supported by monopile in different soil conditions (Prendergast, et al., 2015)

4.3. Approach 1: Estimating system natural frequency and foundation damping by correlations with pile deformations at mudline level derived from numerical analyses.

This approach bases on results of the parametric study summarized section 4.2.4. Pile lateral displacement, y_o, and rotation, θ_o, caused by excitation loads are correlated with foundation rigidity coefficient, λ, and foundation damping, ξ_{fdn}, resulted from subsequent dynamic analyses.

4.3.1. Procedure of establishing the relationships

The λ - ξ_{fdn}, $y_o - \lambda$, $\theta_o - \lambda$, $y_o - \xi_{fdn}$, and $\theta_o - \xi_{fdn}$ relationships are established by following steps:

- Step 1: Plotting the data points for each soil relative density on a separate graph,
- Step 2: Plotting the data again for each pile diameter altogether on one graph,
- Step 3: Plotting the data altogether on one graph

While Step 1 provides the concept on the evolution of data, Step 2 facilitates back-calculating λ - ξ_{fdn}, $y_o - \lambda$, $\theta_o - \lambda$, $y_o - \xi_{fdn}$, and $\theta_o - \xi_{fdn}$ responses for each pile diameter and Step 3 is aimed for the relationships for whole set of data. For fixed base condition, the data is set as $\lambda = 1$, ξ_{fdn} =0.001%. y_o/D_P=0.00001, θ_o = 0.00001 and is added to data pool as upper bound or lower bound in regression analysis for λ - ξ_{fdn}, $y_o - \lambda$, $\theta_o - \lambda$, $y_o - \xi_{fdn}$, and $\theta_o - \xi_{fdn}$ relations.

4.3.2. Pile deformations – foundation rigidity coefficient relationships

A consistent and apparent trend is reported in $y_o - \lambda$ and $\theta_o - \lambda$ correlations (Figure 4.9 and Figure 4.10). Normalized lateral displacement, y_o/D_P, and pile rotation, θ_o, illustrate strong correlations between y_o/D_P and λ, and between θ_o and λ at different soil relative densities and pile diameters. The data shows that λ has stronger correlation with y_o/D_P (Table 4.2 and Table 4.3)

4.3.3. Pile deformations – foundation damping ratio relationships

Similar approach is utilized to determine $y_o - \xi_{fdn}$ and $\theta_o - \xi_{fdn}$ correlations (Figure 4.11). The linear regression shows good correlations with the data and ξ_{fdn} is better correlated with θ_o (Table 4.4 and Table 4.5).

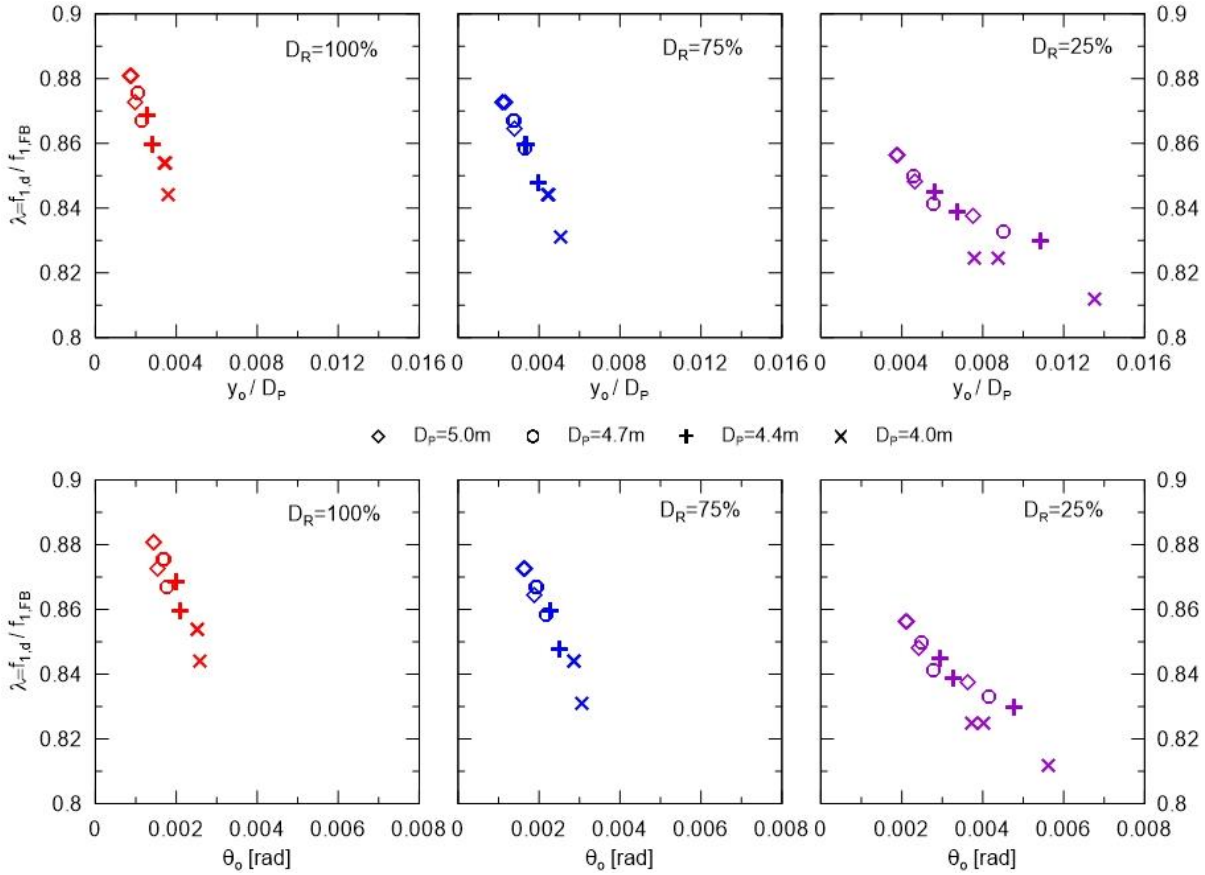

Figure 4.9. Relationships between y_o/D_P and λ (top), and between θ_o and λ (bottom) at different soil D_R.

Table 4.2. y_o/D_P – λ relationship

D_P (m)	Curve-fitting equation	R^2	Compatibility
5.0	$\lambda = -0.025 \cdot \ln(y_o / D_P) + 0.72$ (3-68)	0.989	$0 < y_o/D_P < 0.008$
4.7 & 4.4	$\lambda = -0.025 \cdot \ln(y_o / D_P) + 0.72$ (3-69)	0.991	$0 < y_o/D_P < 0.011$
4.0	$\lambda = -0.026 \cdot \ln(y_o / D_P) + 0.70$ (3-70)	0.995	$0 < y_o/D_P < 0.014$
Overall	$\lambda = -0.026 \cdot \ln(y_o / D_P) + 0.71$ (3-71)	0.961	$0 < y_o/D_P < 0.014$

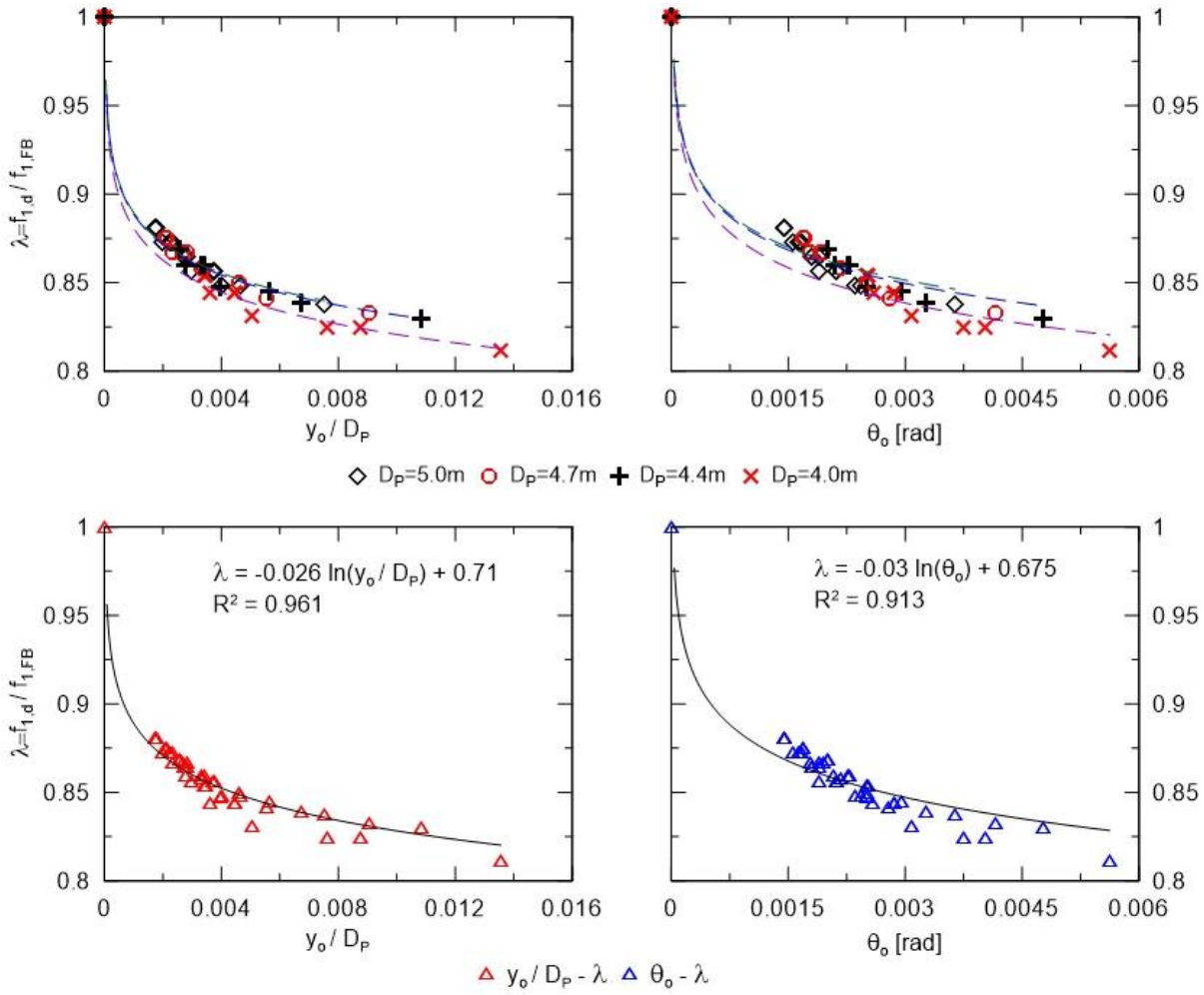

Figure 4.10. Relationships between y_o/D_P and λ, and between θ_o and λ.

Table 4.3. θ_o– λ relationship

D_P (m)	**Curve-fitting equation**		**R^2**	**Compatibility**
5.0	$\lambda = -0.027 \cdot \ln(\theta_o) + 0.70$	(3-72)	0.963	$0 < \theta_o < 0.004$ rad
4.7 & 4.4	$\lambda = -0.027 \cdot \ln(\theta_o) + 0.69$	(3-73)	0.965	$0 < \theta_o < 0.005$ rad
4.0	$\lambda = -0.029 \cdot \ln(\theta_o) + 0.67$	(3-74)	0.982	$0 < \theta_o < 0.006$ rad
Overall	$\lambda = -0.03 \cdot \ln(\theta_o) + 0.675$	(3-75)	0.913	$0 < \theta_o < 0.006$ rad

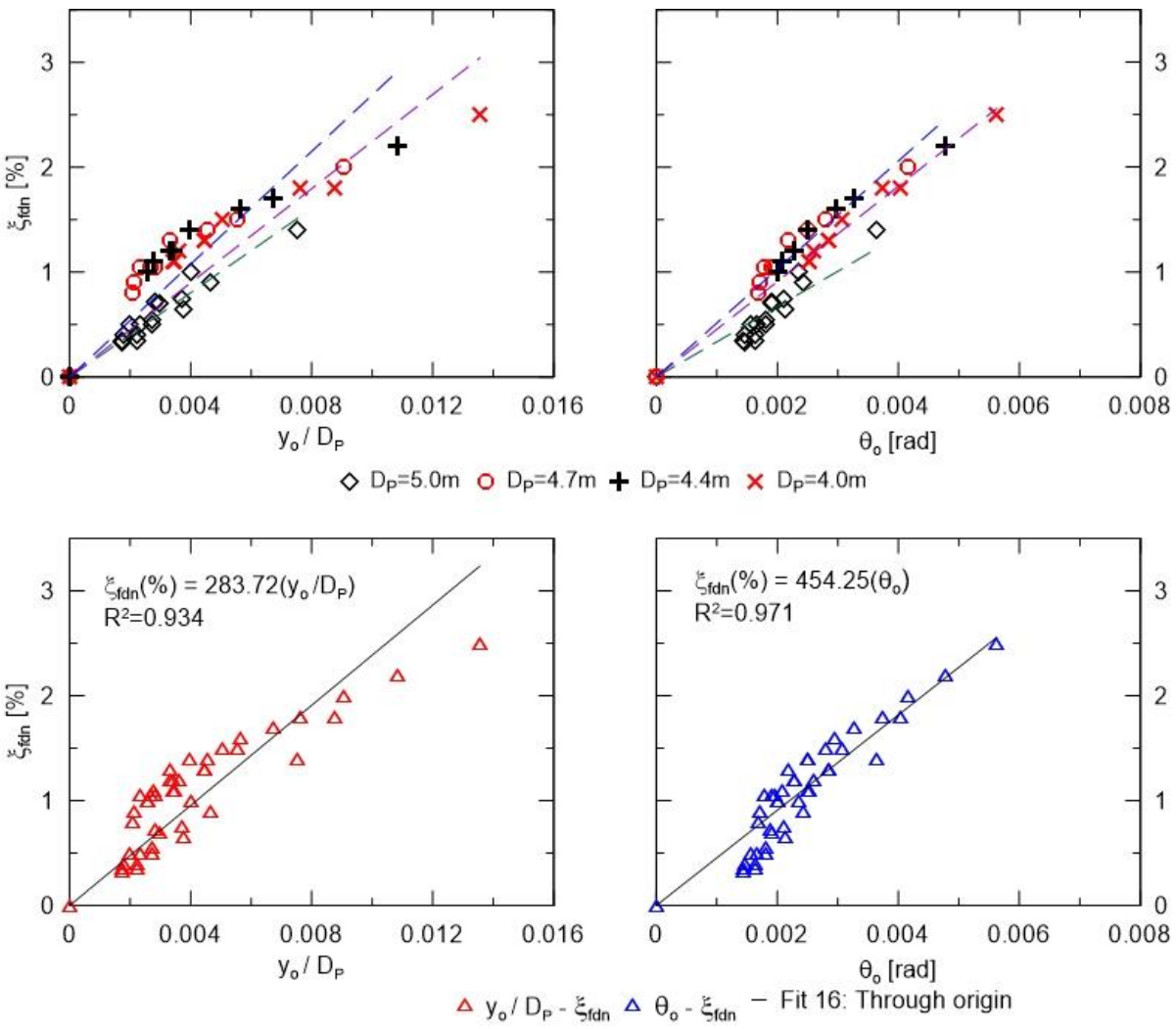

Figure 4.11. Relationships between y_o/D_P and ξ_{fdn}, and between θ_o and ξ_{fdn}.

Table 4.4. y_o/D_P – ξ_{fdn} relationship

D_P (m)	**Curve-fitting equation**		**R^2**	**Compatibility**
5.0	$\xi_{fdn}[\%] = 200.79 \cdot (y_o / D_P)$	(3-76)	0.983	$0< y_o/D_P <0.008$
4.7 & 4.4	$\xi_{fdn}[\%] = 268.88 \cdot (y_o / D_P)$	(3-77)	0.938	$0< y_o/D_P <0.011$
4.0	$\xi_{fdn}[\%] = 224.50 \cdot (y_o / D_P)$	(3-78)	0.955	$0< y_o/D_P <0.014$
Overall	$\xi_{fdn}[\%] = 238.72 \cdot (y_o / D_P)$	(3-79)	0.934	$0< y_o/D_P <0.014$

Table 4.5. $\theta_o - \xi_{fdn}$ relationship

D_P (m)	Curve-fitting equation		R^2	Compatibility
5.0	$\xi_{fdn}[\%] = 336.04 \cdot (\theta_o)$	(3-80)	0.969	$0 < \theta_o < 0.004$ rad
4.7 & 4.4	$\xi_{fdn}[\%] = 515.00 \cdot (\theta_o)$	(3-81)	0.994	$0 < \theta_o < 0.005$ rad
4.0	$\xi_{fdn}[\%] = 455.05 \cdot (\theta_o)$	(3-82)	0.999	$0 < \theta_o < 0.006$ rad
Overall	$\xi_{fdn}[\%] = 454.25 \cdot (\theta_o)$	(3-83)	0.971	$0 < \theta_o < 0.006$ rad

4.3.4. Foundation rigidity coefficient – foundation damping relationship

The λ - ξ_{fdn} responses at analyzed pile configurations and soil conditions are plotted in Figure 4.12. A consistent trend is shown that foundation damping decreases with increasing foundation rigidity coefficient. Curve-fitting suggests power trendline is most appropriate for the data points obtained from analyses for D_P=5m, 4.7 and 4.4m, and 4.0m (

Table 4.6). However, the overall λ - ξ_{fdn} relationship for all data points has lower level of correlation, reflecting in value of coefficient of determination, R^2, than that of $y_o/D_P - \lambda$, $\theta_o - \lambda$, $y_o/D_P - \xi_{fdn}$, and $\theta_o - \xi_{fdn}$ responses. Therefore, it is recommended to use $y_o/D_P - \lambda$ and $\theta_o - \xi_{fdn}$ relationships to find system dynamic properties.

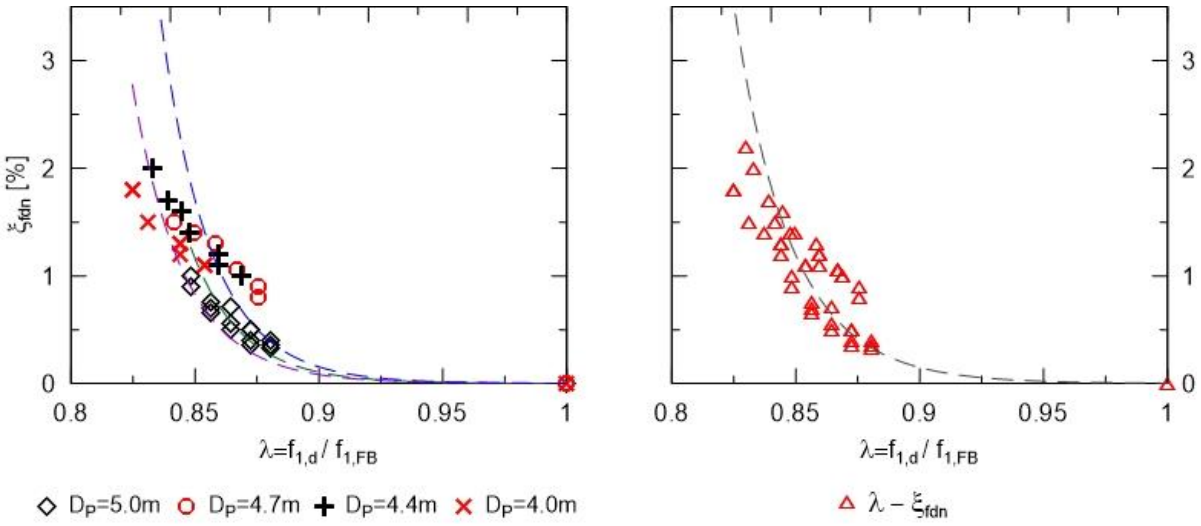

Figure 4.12. $\lambda - \xi_{fdn}$ relationships at various pile diameters (left) and in general (right)

Table 4.6. $\lambda - \xi_{fdn}$ relationship

D_P (m)	Curve-fitting equation	R^2	Compatibility
5.0	$\xi_{fdn}[\%] = 0.0014(\lambda)^{-41.1}$ (3-84)	0.934	$0.84 \leq \lambda \leq 1$
4.7 & 4.4	$\xi_{fdn}[\%] = 0.0021(\lambda)^{-40.8}$ (3-85)	0.840	$0.83 \leq \lambda \leq 1$
4.0	$\xi_{fdn}[\%] = 0.0014(\lambda)^{-38.9}$ (3-86)	0.835	$0.81 \leq \lambda \leq 1$
Overall	$\xi_{fdn}[\%] = 0.0039(\lambda)^{-35.0}$ (3-87)	0.710	$0.81 \leq \lambda \leq 1$

4.4. Approach 2: Estimating natural frequency by computing K_L, K_R, and K_{LR} from pile deformations at mudline level caused by excitation load

In this this approach, lateral displacement, y_o, and rotation, θ_o, caused by excitation loads are used to solve for foundation stiffnesses K_L, K_R, and K_{LR}. Natural frequency is subsequently calculated by implementing the stiffnesses in Arany, et al. (2016) equations. This method allows finding K_L, K_R, and K_{LR} for layered ground, for foundation with presence of local scour or for monopile with additional load from hydrokinetic devices. Distribution and values of soil modulus along pile length are reflected in K_L, K_R, and K_{LR} values.

4.4.1. Calculation procedure

Estimation of natural frequency undergoes following steps:

- Step1: Running static analysis with excitation loads of wind thrust and wave loading and determining y_o and θ_o from analyzed outcomes,
- Step 2: Computing lateral load, $H_{y,o}$ and bending moment, $M_{x,o}$, at ground level caused by wind thrust and wave distributed load. Additional moment induced by self-weight of the rotor should be included as the lateral displacement at rotor level can be determined in Step 1.
- Step 3: Solving following equations for K_L, K_R, and K_{LR}

$$\begin{cases} H_{y,o} = K_L y_o + K_{LR}\theta_o \\ M_{x,o} = K_{RL} y_o + K_R \theta_o \\ K_{LR} = K_{RL} = -\sqrt{0.5 K_L K_R} \end{cases} \quad (3\text{-}88)$$

where the first two equations are derived from equation 3-59, while the last one is an assumption based on formulea for K_L, K_R, and K_{LR} suggested by Gazetas (1984), Pender (1993) and Shadlou and Bhattacharya (2016) for flexible pile embedded in soil with parabolic modulus profile.

- Step 4: Computing foundation rigidity coefficient, λ, and natural frequency using (Arany, et al., 2016) procedure described by equations 3-45 to 3-56

$$\lambda = C_L \cdot C_R \quad (3\text{-}89)$$

where C_L and C_R are defined by equations 3-49 and 3-50, respectively.

4.4.2. Results on foundation rigidity coefficient

Foundation rigidity coefficient, λ_K, is calculated by Approach 2 procedure for all the wind turbines in the parametric study. Obtained values are compared with those resulted from numerical dynamic analyses, λ_{FEM} (Figure 4.13). 11 out of 43 values of λ_K/λ_{FEM} ratio are less than 0.95, and all of them are in conditions either having the lowest D_R=25%, the shortest L_P=19.2m, or the smallest D_P=4.0m. In such cases, soil around pile develop enough inelastic deformations under action of $H_{y,o}$ and $M_{x,o}$ and soil equivalent secant modulus is significantly lower than the effective modulus during vibration after the excitation is removed. As a result, K_L, K_R, and K_{LR} are underestimated. This approach in general tend to not overestimate natural frequency.

4.4.3. Recommendation on soil modulus, E_{S0}, in established equations for K_L, K_R, and K_{LR}

Selecting proper value of Young modulus, E_{S0}, for established formulae of K_L, K_R, and K_{LR} presented in Table 4.1 is very important for determining the natural frequency by 3-spring model. Figure 4.14 compares values of K_L and K_R obtained by solving equations 3-88 for piles in the parametric study and by Shadlou and Bhattacharya (2016) formulae with $E_{S0}=E_{ur}$ and $E_{S0}=E_{50}$. The E_{ur} and E_{50} values are computed for depth of $1D_P$ using the G_0 profiles at D_R = 100%, 75%, and 25% for numerical simulations.

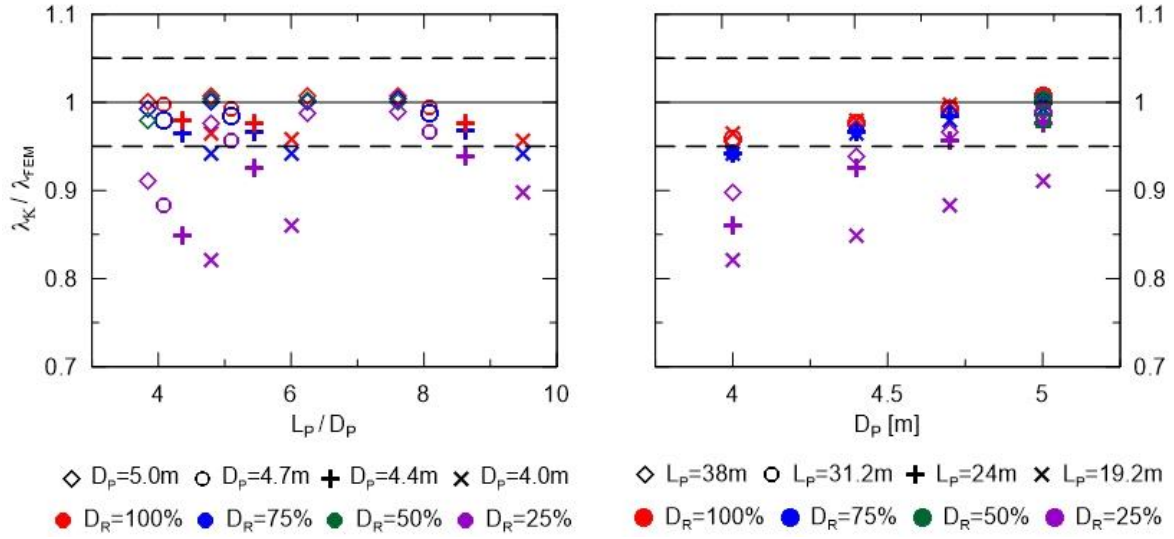

Figure 4.13. Comparison of λ resulted from FE analyses and Approach 2 by soil relative density, pile diameter, and embedded length.

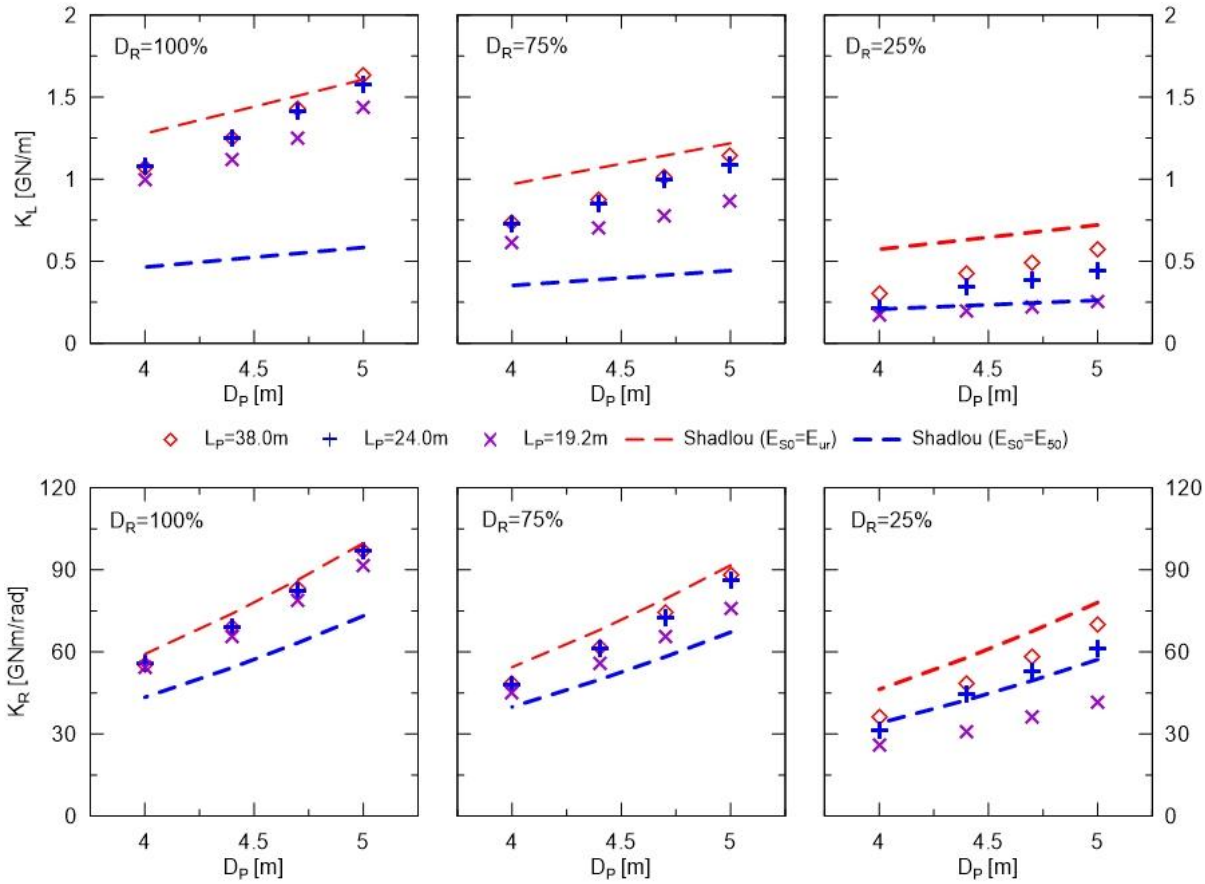

Figure 4.14. Comparisons of K_L (top) and K_R (bottom) resulted from solving equations 3-88 and Shadlou and Bhattacharya (2016) formulae.

Figure 4.13 and Figure 4.14 show that the cases that have λ_K/λ_{FEM} ratio in between 0.95 and 1.05 have K_L and K_R close to values computed by Shadlou and Bhattacharya (2016) equation with $E_{S0}=E_{ur}$. On contrary, cases having K_L and K_R approaching or below the curves defined by $E_{S0}=E_{50}$ have increasingly less accurate prediction of λ. Therefore $E_{ur} = 0.3E_{0,}$ where E_0 is maximum modulus, is recommended for Young modulus E_{S0} in established formulae by Gazetas (1984), Pender (1993) and Shadlou and Bhattacharya (2016).

Using $E_{S0}=E_{50}$ in Shadlou and Bhattacharya (2016) equations for K_L, K_R, and K_{LR} leads to better prediction of natural frequency (Figure 4.15). λ is computed by Arany, et al. (2016) closed form equations. This implementation, however, tend to overestimate λ at $L_P < L_{c,const}$. Therefore, a modification for embedded length for this condition is recommended in further study.

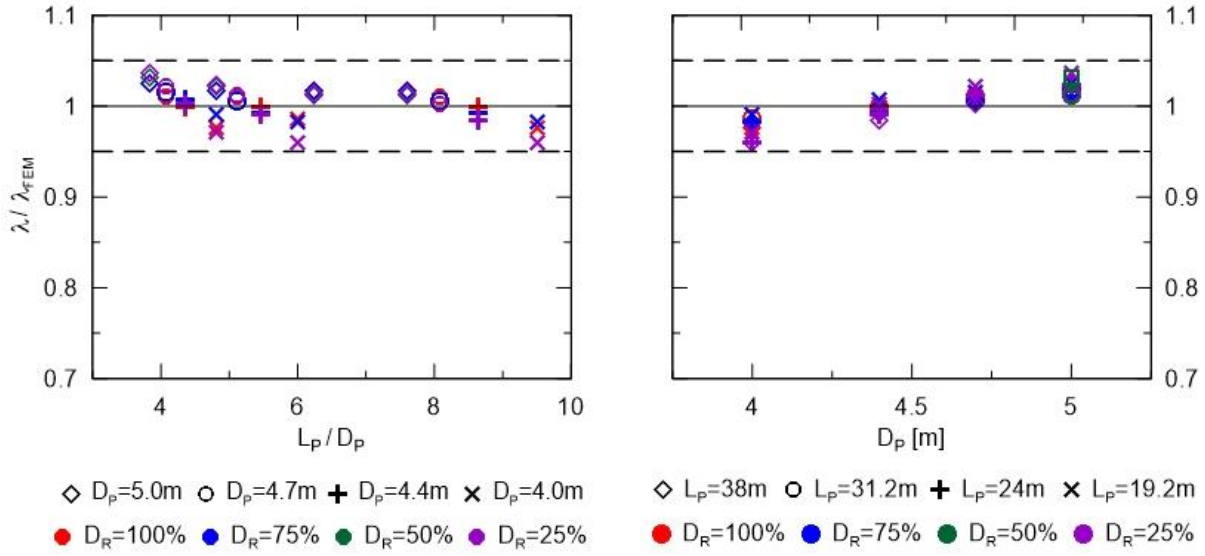

Figure 4.15. λ/λ_{FEM} ratio with λ computed by Shadlou and Bhattacharya (2016) formulae using $E_{S0}=E_{ur}$.

4.5. Applying developed approaches to estimate natural frequency and foundation damping of existing monopiles offhore winf turbines

Natural frequency and damping of Burbo Bank and Walney 1 wind turbines are re-calculated by Approaches 1 and 2. These projects are part of model calibration in Chapter 3 but their configurations on pile dimensions and loading are not incldued in the parametric study. The values of $H_{y,o}$ and $M_{x,o}$ are computed fromexcitation loads of wind thrust and

distributed wave load, and y_o and θ_o are obtained from static analyses of the wind turbines subjected to the the excitation. These parameters are subsequenly used to computed λ and ξ_{fdn} by regressed correlations by Approach 1, and the steps of Approach 2.

Outcomes are compared to FE simulation results and available field measurements in Table 4.8 and Table 4.9 . FE, Approach 1, Approach 2 all overestimated λ with the error less than 5%. Approach 1 appears to have better accuracy than Approach 2 and is in better agreement with FE results and field measurements.

Table 4.7. Data for computing λ and ξ_{fdn} for Burbo Bank and Walney 1 projects

Project	**D_P (m)**	**$H_{y,o}$ (kN)**	**$M_{x,o}$ (kNm)**	**θ_o (rad)**	**y_o (m)**	**y_o/D_P**	**$f_{1,FB}$ (Hz)**
Burbo Bank	4.7	917	59,503	0.0013	0.0077	0.00164	0.343
Walney 1	6.0	1,817	82,084	0.0011	0.0095	0.00159	0.398

Table 4.8. λ obtained from different methods for Burbo Bank and Walney 1 projects

Method	**Measurement**	**FEM**	**Approach 1**		**Approach 2**
			Eq. 4-27	**Eq. 4-31**	
Burbo Bank	0.851	0.872	0.877	0.876	0.89
Walney 1	0.878	0.883	0.878	0.879	0.92

Table 4.9. ξ_{fdn} obtained from different methods for Burbo Bank and Walney 1 projects

Method	**Measurement**	**FEM**	**Approach 1**		**Approach 2**
			Eq. 4-35	**Eq. 4-39**	
Unit	%	%	%	%	%
Burbo Bank	N/A	0.56	0.50	0.52	N/A
Walney 1	N/A	0.45	0.49	0.46	N/A

4.6. Natural frequency and foundation damping of monopile offshore wind turbine with presence of local scour

4.6.1. Numerical simulation of monopile with local scour

Similar numerical model and analyzing stages as in the parametric study in Chapter 3 are deployed for investigating effect of local scour depth. An additional step of soil excavation is added into the model to describe the development of the scour and its consequential impact on stress-strain state in soil surrounding the pile (Figure 4.16). Excitation loads is applied after soil removal for subsequent dynamic analysis for natural frequency and damping.

The analyses are performed for pile with D_P=5.0m. Values pile embedment, L_P, soil relative density, D_R, and scour depth, S_L, are presented in Table 4.10. Soil properties are determined by correlations with CPT q_c, which is correlated with soil D_R. Soil stress history parameters (OCR, K_0) are computed by empirical relationships with q_c profile and are included in soil model. Hardening soil with small strain (HSsmall) constitutive model is employed for the analyses. Descriptions on soil properties, constitutive model and simulation procedure are detailed in Chapter 3.

The removal of soil has influence on values of y_o and θ_o caused by excitation load. The pile deformations then are used for calculation of λ and ξ_{fdn} by Approach 1. The results are compared with outcomes of FE simulations to examine compatibility of the Approach 1's equations in finding λ and ξ_{fdn} for monopile wind turbines with local scour.

Table 4.10. Matrix of analyses of monopile with local scour

D_R(%) / **L_P (m)**	**100**	**75**	**50**	**25**
38	S_L = 4.8, 7.2m	S_L = 4.8, 7.2m	S_L = 4.8, 7.2m	S_L = 4.8, 7.2m
24	S_L = 4.8, 7.2m	S_L = 4.8, 7.2m	S_L = 4.8, 7.2m	S_L = 4.8, 7.2m

4.6.2. Simulation outcomes for monopile with local scour

Impacts of local scour depth, SL, on system natural frequency and foundation damping are presented in Figure 4.17 and Figure 4.18. Natural frequency has increasing rate of decline as S_L increases. The relative reduction is greater in softer deposits and at the scour depth of 1.3D_P natural frequency reduce by over 5% in all analyzed cases. L_P=24m is close to critical embedment for constant displacement, $L_{c,const}$; therefore, as S_L develops $f_{1,SL}$ drops faster than in piles with L_P=38m. This confirms the important role of $L_{c,const}$ to natural

frequency and damping suggested in results of the parametric study in Chapter 2. Foundation damping has also an increased degree of change in piles with initial L_P=24m. It is not recommended to have local scour depth that reduces the effective embedment below $L_{c,const}$.

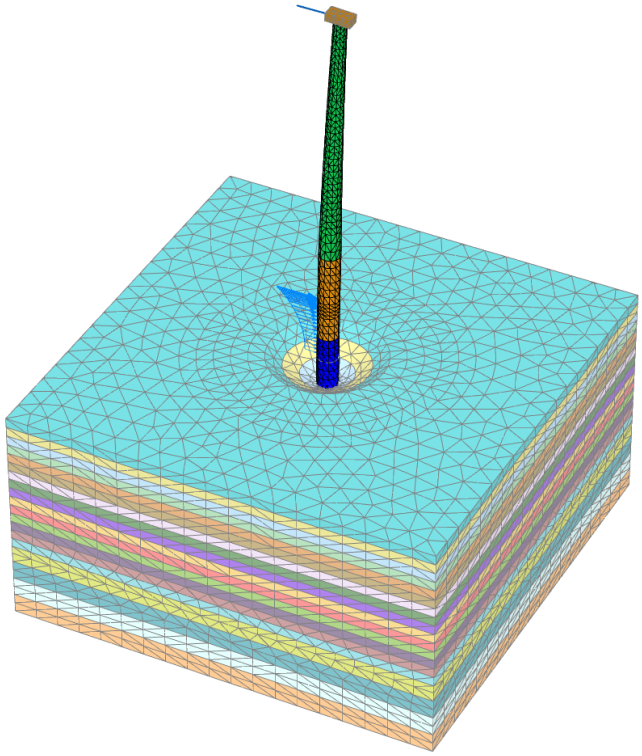

Figure 4.16. Numerical model for dynamic analyses with presence of local scour

Development of local scour results in increased cantilever arm of the above-ground structure, decreased effective pile embedded length, and removal of the overconsolidated soil nearing the mudline. Therefore, its impact on natural frequency is significant. For comparison, the parametric study in Chapter 3 shows that as L_P decreases from 38.0m to 19.2m, natural frequency decreases by just up to 2.2%. Scour protection thus is very important for offshore monopile wind turbines in preventing the evolving of global and local scour due to wave and current activities.

4.6.3. Estimating impacts of scour on $f_{1,d}$ and ξ_{fdn} by Approach 1

Foundation rigidity coefficient, λ_A, and foundation damping, ξ_{fdn}, for the monipile wind turbines listed in Table 4.10 by equations 3-71, 3-75, 3-79, and 3-83 developed by the Approach 1. λ_A and ξ_{fdn} are determined by following sets of pile deformations to figure out if

using deformations at mudline or bottom of scour depth is more appropriate:

- Pile lateral displacement and rotation at initial mudline (y_o, θ_o). Fixed based frequency, $f_{1,FBo}$, is calculated for the structure fixed at mudline level. $f_{1,d}=\lambda_{A,o}\ f_{1,FBo}$
- Pile lateral displacement and rotation at bottom of the scour (y_s, θ_s). Fixed based frequency, $f_{1,FBs}$, is calculated for the structure fixed at scour depth S_L. $f_{1,d}=\lambda_{A,s}\ f_{1,FBs}$

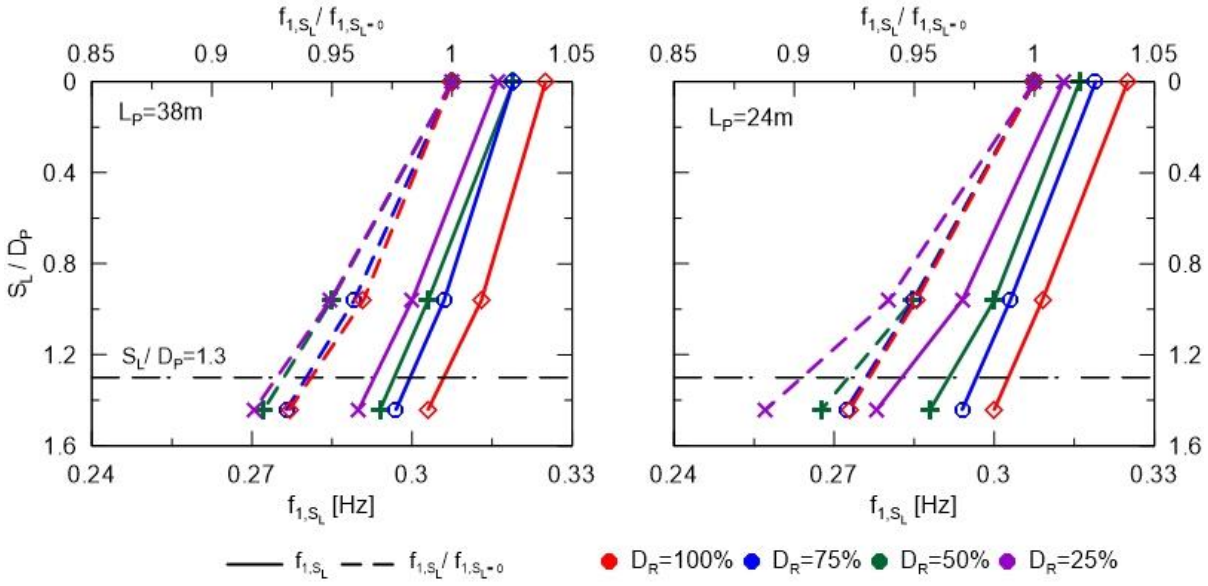

Figure 4.17. Influence of local scour depth on natural frequency at various soil D_R and L_P.

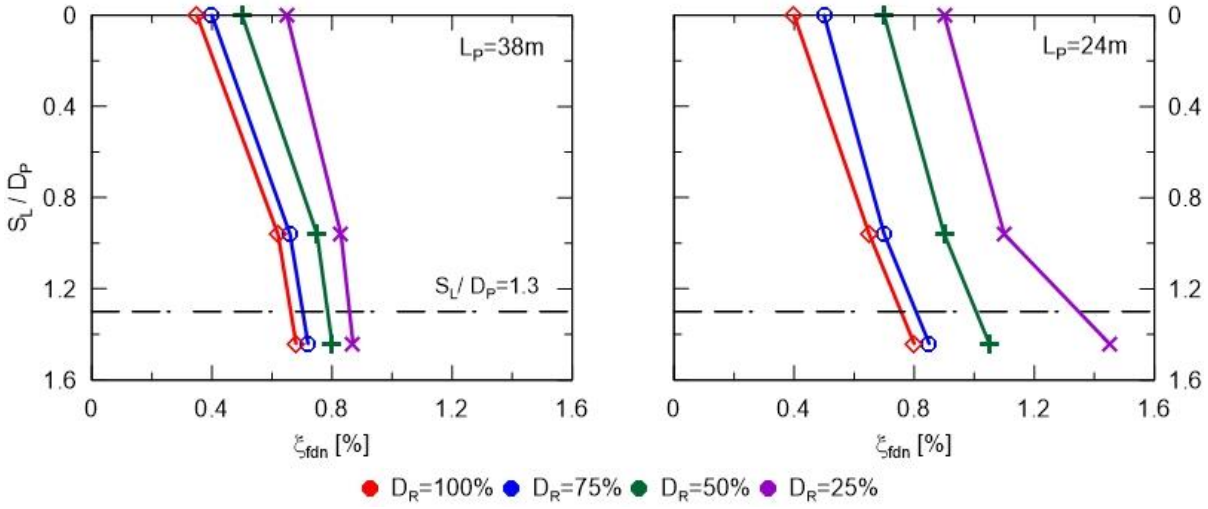

Figure 4.18. Influence of local scour depth on ξ_{fdn} at various soil D_R and L_P.

Foundation rigidity coefficient by FE simulation, λ_{FEM}, is also computed with respect to $f_{1,FB}$ at both scenarios to be compared with λ_A. $\lambda_{FEM,o} = f_{FEM}/ f_{1,FBo}$ and $\lambda_{FEM,s} = f_{FEM}/ f_{1,FBs}$

with f_{FEM} is natural frequency obtained by performing numerical simulations. Modal analyses are performed in SAP 2000 for wind turbine superstructure with fixed restraint assigned at mudline and bottom of scour depth to determined $f_{1,FB}$ (Table 4.11).

Figure 4.19 compare results on λ and ξ_{fdn} for piles obtained from two above mentioned methods. Full data is included in the Appendix C. It appears that λ and ξ_{fdn} resulted from $f_{1,FBs}$ and pile deformation at scour depth level, (y_s, θ_s), are in better agreement with FE outcomes Therefore, when using Approach 1 to find λ and ξ_{fdn} with presence of local scour, the monopile should be treated as it has the ground surface at bottom of the scour hole.

Computation of λ by both methods have good agreement. The results show that correlation 3-71 (between $\lambda - y_o/D_P$) has better prediction than 3-75 (between $\lambda - \theta_o$). Meanwhile, the correlation 3-83 (between ξ_{fdn} and θ_o) yield better agreement with FE results than equations 3-79 (between ξ_{fdn} and y_o/D_P). However, correlation 3-83 shows higher level of variance with numerical results than 3-71 and the difference could be up to $\pm$ 10%; therefore, further work is recommended to improve ξ_{fdn} - θ_o and ξ_{fdn} - y_o/D_P relationships.

Table 4.11. $f_{1,FB}$ computed at different locations of fixed restraint

Fixation location	**At mudline**	**At S_L=4.8m**	**At S_L=7.2m**
$f_{1,FB}$ (Hz)	0.369	0.345	0.334

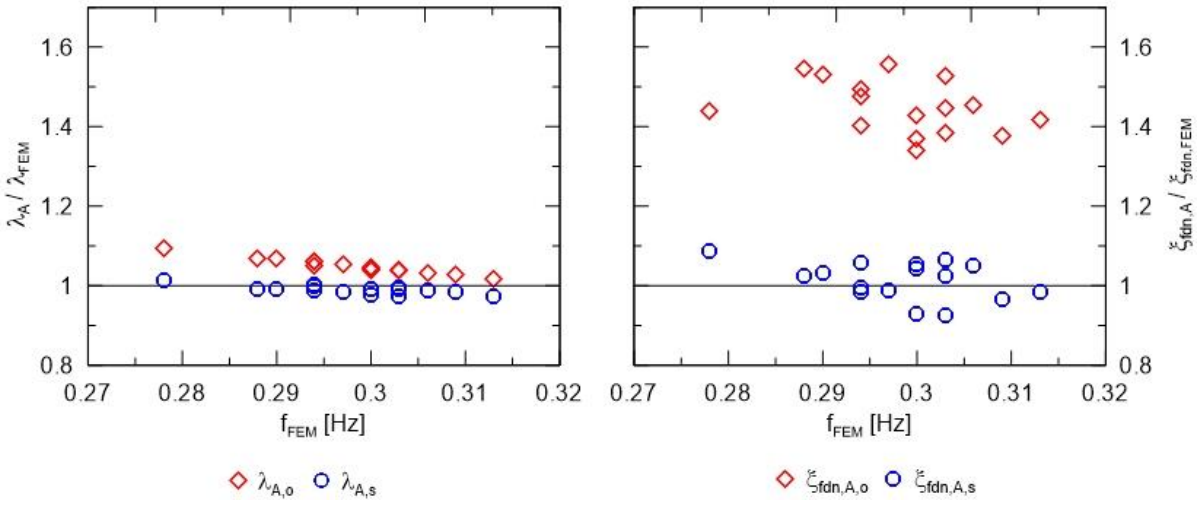

Figure 4.19. Comparisons of λ (left) and ξ_{fdn} (right) by FE simulations and Approach 1 for monopile with local scour.

4.7. Natural frequency and foundation damping of monopile-supported hybrid system.

4.7.1. Numerical simulation of hybrid system

A monopile-supported hybrid system comprises of a monopile wind turbine, and hydrokinetic (MHK) devices mounted on the wind turbine. MHK devices provide additional mass participating in system vibration and additional loads caused by wave, current or tide to the structure. The value and location of the added mass and loads depend on type and size of MHK device and met-ocean condition of the site.

MHK is described as an annulus plate around monopile perimeter (Figure 4.20). This description does not increase flexural rigidity of the transition piece. Outside diameter of the plate is 10m and its thickness in 0.2m. The mass of MHK device is controlled by assigning unit weight of the plate's material. A point load is applied to the monopile at the plate level, assuming this load coaligned with wave load and acting along centerline of monopile's section.

The main aim of hybrid system simulation is to evaluate the influence of MHK device location. The analyses are performed for pile with D_P=5.0m and two values of L_P of 38m, and 31.2m. The mass of MHK device, M_{MHK} =234.5 tons, which is equal to the mass of wind turbine's rotor-nacelle assembly, is selected. Wave load on MHK device, W_{MHK} =590 kN, is chosen to be equal to total wave load on the monopile (Table 4.12). By placing the plate at 15m and 8m from mudline level, impacts of MHK device level on system natural frequency and foundation damping is determined. MHK devices at 15m represents wave energy converters fluctuating around mean sea level while the ones at 8m above the mudline to describe underwater tidal energy turbines.

Table 4.12. Data for simulations of hybrid system

L_P (m)	**M_{MHK} (tons)**	**H_{MHK} (m)**	**D_R**	**W_{MHK} (kN)**
38.0	234.5	15m, 8m	100%, 75%, 25%	590.0
31.2	234.5	15m, 8m	100%, 75%, 25%	590.0

Dynamic analyses are performed after removal of excitation loads, including wind thrust on rotor, wave distributed load and wave load on MHK device, to find natural

frequency and foundation damping. The outcomes are compared with that computed by Approach 1.

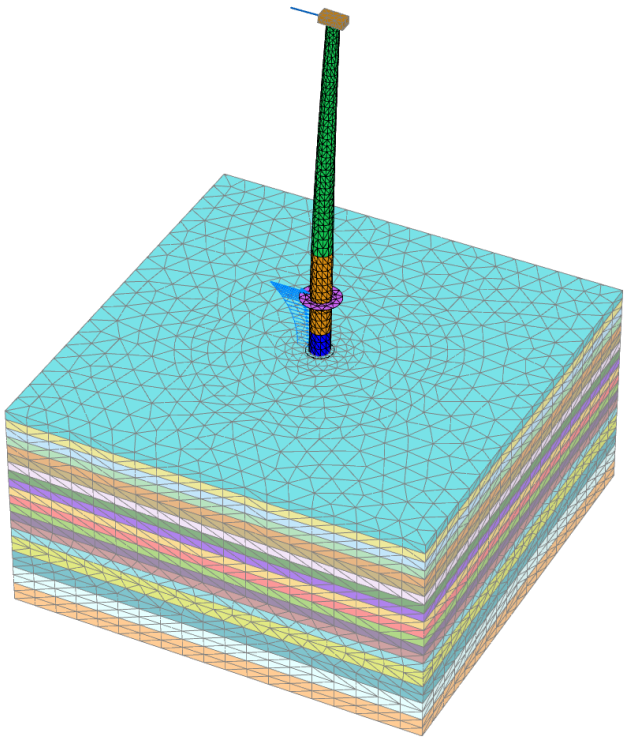

Figure 4.20. Numerical model for hybrid wind-wave system.

4.7.2. Simulation outcomes for monopile with local scour

Modal analyses by SAP2000 show that M_{MHK} placed at either 15.0m or 8.0m has insignificant impact of $f_{1,FB}$ (Table 4.13). Dynamic analyses by Plaxis also show no changes in system natural frequency across the soil relative density values due to added selection of M_{MHK} and W_{MHK} (Table 4.14). However, in term of foundation damping, there is a remarkable increase (Table 4.15 and Table 4.16). For comparison, the changes in ξ_{fdn} that happen to piles with L_P=38.0m are comparable to the increase obtained in the parametric study when the embedment decreases from 38.0m to 19.2m. Relocation of MHK device from 8m to 15m above mudline level yield similar results on ξ_{fdn}.

4.7.3. Estimating $f_{1,d}$ and ξ_{fdn} of hybrid system by Approach 1

Similar to analyses with scour, Approach 1 provides good estimation on λ compared to FE but not as good for ξ_{fdn} (Figure 4.21). Correlations 3-71 ($\lambda - y_o/D_P$) and 3-83 ($\xi_{fdn} - \theta_o$) appear to yield better agreement with FE results than equations 3-75 ($\lambda - \theta_o$), and 3-79 (ξ_{fdn} -

y_o/D_P), respectively.

Table 4.13. $f_{1,FB}$ computed with different M_{MHK}

M_{MHK} (tons)	234.5	469.0	938.0
$f_{1,FB}$ (Hz)	0.369	0.369	0.368

Table 4.14. Change in $f_{1,d}$ caused by selected MHK device for monopiles with L_P=38m and 31.2m

M_{MHK} (tons)	**H_{MHK} (m)**	**$f_{1,d}$ (D_R=100%)**	**$f_{1,d}$ (D_R=75%)**	**$f_{1,d}$ (D_R=25%)**
0	-	0.325	0.319	0.316
234.5	15.0	0.325	0.319	0.316
234.5	8.0	0.325	0.319	0.316

Table 4.15. Change in ξ_{fdn} caused by selected MHK device for monopiles with L_P=38m

M_{MHK} (tons)	**H_{MHK} (m)**	**ξ_{fdn} (%)**		
		D_R=100%	**D_R=75%**	**D_R=25%**
0	-	0.35	0.40	0.65
234.5	15.0	0.80	1.00	1.40
234.5	8.0	0.70	0.90	1.30

Table 4.16. Change in ξ_{fdn} caused by selected MHK device for monopiles with L_P=31.2m

M_{MHK} (tons)	**H_{MHK} (m)**	**ξ_{fdn} (%)**		
		D_R=100%	**D_R=75%**	**D_R=25%**
0	-	0.40	0.50	0.90
234.5	15.0	0.90	1.10	1.50
234.5	8.0	0.80	1.00	1.40

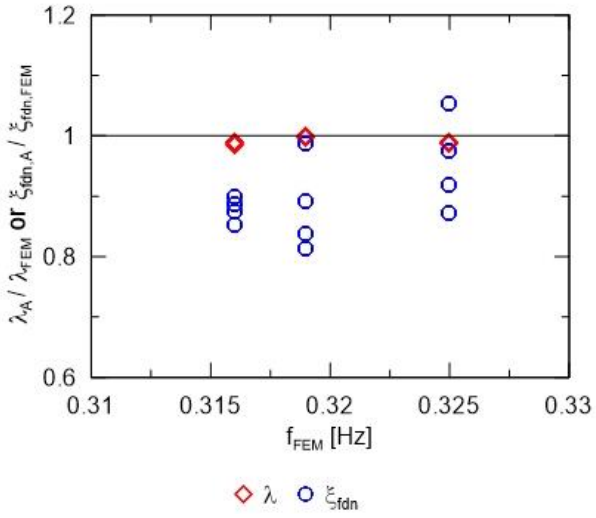

Figure 4.21. Comparisons of λ (left) and ξ_{fdn} (right) by FE simulations and Approach 1 for hybrid system.

4.8. Conclusions

Establishing connections between pile deformations at mudline level and system natural frequency and foundation damping is the focus of this study. Two approaches are proposed based on the parametric study results in Chapter 3. Approach 1 works on establishing correlations between pile lateral displacement, y_o, and rotation, θ_o, at mudline caused by the excitation loads and characteristics of the vibration ($f_{1,d}$ and ξ_{fdn}) that happens after the excitation is removed. Approach 2 is staged to solve for foundation stiffness, K_L, K_R, and K_{RL} before calculating $f_{1,d}$ following the procedure suggested by Arany, et al. (2016). Natural frequency is represented by foundation rigidity coefficient λ to show its proportion to frequency of the same structure but with a fixed restraint at muddling level. Additional numerical simulations are performed to evaluate effects local scour and presence of MHK devices to $f_{1,d}$ and ξ_{fdn} of monopile-supported wind turbine and hybrid system, respectively. Conclusions drawn from this study are presensented as follows:

- There are strong correlations between y_o and λ, θ_o and λ, y_o and ξ_{fdn}, and θ_o and ξ_{fdn}. The most correlated relationships are y_o/D_P – λ and θ_o - ξ_{fdn}. It is not only shown in the determination coefficient, R^2, in the curve-fitting line but also in the estimations of λ and ξ_{fdn} for monopile with scour and hybrid system. Natural frequency and

foundation damping of an offshore monopile wind turbine can be estimated by following equations by Approach 1:

$$\lambda = -0.026 \cdot \ln(y_o / D_p) + 0.71$$

$$\xi_{fdn}[\%] = 454.25 \cdot (\theta_o)$$

- Natural frequency and foundation damping of an offshore wind turbine can be predicted by following steps:
    1. Finding natural frequency of the structured fixed at mudline level, $f_{1,FB}$.
    2. Performing static analysis of the structure subjected to excitation loads to determine deformations at mudline level, y_o and θ_o.
    3. Calculating λ and ξ_{fdn} by above equations
    4. Computing natural frequency of the wind turbine: $f_{1,d} = \lambda f_{1,FB}$
- Overall, Approach 1 is more accurate than Approach 2 in estimating λ for the wind turbines in the parametric study. Results by Approach 2 are more erroneous for piles that have sufficient plastic deformations developed in surrounding soil under excitation loads. For piles that have $D_P \geq 4.4$m and $L_P \geq 24.0$m installed in soil with $D_R \geq 75\%$, Approach 2 provides results within 5% offset from FE outcomes.
- The correlations developed by Approach 1 estimate natural frequency for two existing wind turbines at Burbo Banks and Walney 1 with less than 3% error compared to measurement data.
- The simulation successfully describe the impact of local scour depth on $f_{1,d}$ and ξ_{fdn}. Degree of change is larger in softer deposits and increases as the scour depth develops and reduces pile effective embedment below critical depth for constant displacement.
- Local, and likely global scour as well, has significant impacts on dynamic behavior of monopile wind turbines. For monopile with D_P=5m and L_P=38m, scour depth S_L=7.2m causes a reduction in natural frequency that is about 3 times as much as decreasing L_P from 38m to 19.2m does, according to results of the parametric study

and simulations for monopile with scour.

- While using Approach 1 to predict $f_{1,d}$ and ξ_{fdn} for wind turbine with presence of scour, the structure should be treated as if the ground surface is at the bottom of the scour hole. That means the reference level of the scour bottom should be used for the level of fixed connection, and pile deformations in calculation of $f_{1,FB,}$ $f_{1,d,}$ and ξ_{fdn} .
- Adding mass of MHK devices and load acting the MHK devices to monopile wind turbine system does not change natural frequency, per analyzed results with selected values of the mass and load. However, foundation damping of the hybrid system is 1.5 to some 2 times higher than that of the monopile wind turbine.
- Correlations by Approach 1 estimate natural frequency of monopile wind turbine with scour and hybrid system with excellent agreement with FE results. However, correlation of foundation damping tends to have wide margin of error. For hybrid system, the error could be up to 20%. Therefore, further work is recommended to improve the accuracy of θ_o - ξ_{fdn} relationship.
- It is recommended to check the obtained $y_o/D_P - \lambda$ and θ_o - ξ_{fdn} for monopile in layered ground.

CHAPTER 5. SUMMARY OF CONCLUSIONS, CONTRIBUTIONS, AND RECOMMENDATIONS

The study undertaken in this dissertation is aimed at improving reliability and facilitating computation of natural frequency, $f_{1,d}$ and foundation damping, ξ_{fn}, of offshore monopole-supported wind turbine and hybrid wind-wave system. Three-dimensional numerical analyses are performed to determine dynamic characteristics of the wind turbine structure assuming several configurations of soil conditions and monopile dimensions. The correlations between pile lateral displacement and rotation at seabed level caused by excitation load and natural frequency and foundation damping obtained from dynamic analyses are established. Following are conclusions drawn from results of this study, its contributions, and recommendations for future work

5.1. Summary of Conclusions

Ground stress history plays an important role in lateral behavior of single pile. Consideration of overconsolidation ratio (OCR) and coefficient of lateral earth pressure at rest (K_0) in numerical simulation can improve accuracy of the analyses although impacts of pile installation are not investigated. The overconsolidation ratio OCR is concluded to have pivotal role in analyses of lateral loaded pile. It affects the magnitude of soil shear modulus, constitutive stress-strain response of soil elements and consequently the outcome of the analyses

Extracted soil reactions from numerical simulation output show that distributed moment m(z) and base shear H_b resulted from analysis with normally consolidated soil (OCR=1) have larger contributions in resisting driving force and overturning moment than those in analysis considering soil stress history (OCR>1). The soil reaction components of of m(z) and H_b should not be negelected in analyses of short pile.

Simulations that consider soil loading history (OCR, K_0) appear to provide more accurate estimations of load-displacement response and natural frequency for the pile tests and offshore monopole wind turbines, respectively, used for model calibration.

Pile diameter, D_P, is found to have a larger impact on wind turbine natural frequency, $f_{1,d}$, and foundation damping, ξ_{fdn}, than pile embedment, L_P. The variations in $f_{1,d}$ and ξ_{fdn}

due to change in L_P mostly happens when the embedment falls below the critical length for constant displacement, $L_{c,const}$. This trend also happens when local scour developed deep enough that the pile effective embedded length becomes lower than $L_{c,const}$.

Development of local scour decreases natural frequency at higher rate than when reducing pile embedment without scour at seabed level. Simulation results show that the decline caused by scour depth of 7.2m is three times as much as reducing L_P from 38m to 19.22m.

Simulations of hybrid systems, with selected mass of hydrokinetic devices equal to mass of the rotor-nacelle assembly and additional wave load on rotor being equal to total wave load on wind turbine, show no changes to natural frequency of the system with L_P=38.0m and 31.2m. However, reported increase in foundation damping is approximate to that resulted from reducing L_P from 38.0m to 19.2m.

There are strong correlations between dynamic characteristics ($f_{1,d}$ and ξ_{fdn}) and pile deformations at mudline level (y_o, θ_o). The most correlated relationships established from the parametric outcome are $y_o/D_P - \lambda$ and $\theta_o - \xi_{fdn}$. It is not only shown in the determination coefficient, R^2, in the curve-fitting line but also in the estimations of λ and ξ_{fdn} for monopile with scour and hybrid system.

Natural frequency and foundation damping of an offshore wind turbine can be estimated by following steps:

1. Finding natural frequency of the structured fixed at mudline level, $f_{1,FB}$.
2. Performing static analysis of the structure subjected to excitation loads to determine deformations at mudline level, y_o and θ_o.
3. Calculating λ and ξ_{fdn}

   $$\lambda = -0.026 \cdot \ln(y_o / D_P) + 0.71$$

   $$\xi_{fdn}[\%] = 454.25 \cdot (\theta_o)$$
4. Computing natural frequency of the wind turbine: $f_{1,d} = \lambda f_{1,FB}$

Natural frequency estimated by $y_o/D_P - \lambda$ correlation is very close to that obtained by numerical analyses for monopile wind turbine with presence of local scour and monopile-

supported hybrid system. The θ_o - ξ_{fdn} relationship, however, shows lower degree of agreement with numerical dynamic analyses outcome.

5.2. Summary of Contributions

Two modifications factors, F_{OCR} and F_σ, accounting for overconsolidation ratio and effective stress are proposed to add to empirical correlation between q_c and G_o by Baldi, et al. (1989).

A framework to determine soil model parameters, including the consideration of OCR and K_0 of existing ground, from existing empirical correlations to q_c profile is developed for numerical simulation of laterally loaded pile. The ratios of $G_{ur}^{ref} / G_o^{ref} = 0.3$ and $E_{ur}^{ref} / E_{50}^{ref} = 4$ for model modulus parameters are recommended for Hardening Soil with small strain (HSSsmall) constitutive model in both static and dynamic analyses.

A framework to correlate natural frequency and foundation damping to pile lateral displacement and rotation at seabed level caused by excitation loads is developed for monopile-supported wind turbine and hybrid system. Correlations between y_o/D_P and λ, and between θ_o and ξ_{fdn} are established. These relationships can be straightforwardly used for estimating natural frequency and foundation damping of monopile wind turbine once the frequency of fixed base system, $f_{1,FB}$, is known and pile deformations at mudline are found by static analysis.

5.3. Summary of Recommendations for Future Research

OCR and K_0 are determined from q_c based on Mayne and Kulhawy (1982) OCR-K_0 relationship. However, it is still unclear if the relationship is still valid for sandy soils, whose volume change are sensitive to shear vibration. Therefore, studies on impact of shear wave propagation on soil K_0 and OCR is highly recommended. The suggestion of using soil relative density as an indication of soil stress history also needs to be investigated.

Further research is recommended on effect of suitable pile-wall friction angle (postive and negative) on the shape of the failure surface for determining soil ultimate reaction, p_u, above and below pile's point of rotation for p-y curves.

The lack of information on geotechnical condition and measured natural frequency

and damping of existing offshore monopile wind turbines is a limitation of this study. It is recommended to validate and improve the derived $y_o/D_P - \lambda$ and θ_o - ξ_{fdn} relationships with real world data.

Further study on $y_o/D_P - \lambda$ and θ_o - ξ_{fdn} correlations for monopile wind turbine founded in layered ground is recommended as well.

Hybrid system natural frequency and foundation damping should be further examined with higher level of load that is sufficient to increase the critical embedment for constant displacement, $L_{c,const}$. Further study is needed on whether change in $L_{c,const}$ could also be added as a criterion for limiting values of load transmitted from wave and tidal energy converter to the monopile (or quantity or sizes of those devices) besides the ultimate limit state, serviceability limit state and fatigue limit state criteria.

REFERENCES

Aasen, S., Page, A. M., Skjolden Skau, K., and Nygaard, T. A. (2017). "Effect of foundation modelling on the fatigue lifetime of a monopile-based offshore wind turbine." *Wind Energy Science*, 2(2), 361-376.

Achmus, M., Kuo, Y.-S., and Abdel-Rahman, K. (2009). "Behavior of monopile foundations under cyclic lateral load." *Computers and Geotechnics*, 36(5), 725-735.

Aguirre, D. A., Kowalsky, M. J., Nau, J. M., Gabr, M., and Lucier, G. (2018). "Seismic performance of reinforced concrete filled steel tube drilled shafts with inground plastic hinges." *Engineering Structures*, 165, 106-119.

Álamo, G. M., Aznárez, J. J., Padrón, L. A., Martínez-Castro, A. E., Gallego, R., and Maeso, O. (2018). "Dynamic soil-structure interaction in offshore wind turbines on monopiles in layered seabed based on real data." *Ocean Engineering*, 156, 14-24.

Álamo, G. M., Martínez-Castro, A. E., Padrón, L. A., Aznárez, J. J., Gallego, R., and Maeso, O. (2016). "Efficient numerical model for the computation of impedance functions of inclined pile groups in layered soils." *Engineering Structures*, 126, 379-390.

API (2008). "API RP 2A-WSD: Errata and Supplement 3 for Recommended Practice for Planning, Designing and Constructing Fixed Offshore Platforms-Working Stress Design." American Petroleum Institute, Washington D.C.

API (2020). "API RP 2A-WSD 22nd Ed (R 2020) - Planning, Designing, and Constructing Fixed Offshore Platforms—Working Stress Design." American Petroleum Institute, Washinton DC, USA.

Arany, L., Bhattacharya, S., Adhikari, S., Hogan, S., and Macdonald, J. (2015a). "An analytical model to predict the natural frequency of offshore wind turbines on three-spring flexible foundations using two different beam models." *Soil Dynamics and Earthquake Engineering*, 74, 40-45.

Arany, L., Bhattacharya, S., Macdonald, J., and Hogan, S. (2017). "Design of monopiles for offshore wind turbines in 10 steps." *Soil Dynamics and Earthquake Engineering*, 92, 126-152.

Arany, L., Bhattacharya, S., Macdonald, J., and Hogan, S. J. (2015b). "Simplified critical mudline bending moment spectra of offshore wind turbine support structures." *Wind Energy*, 18(12), 2171-2197.

Arany, L., Bhattacharya, S., Macdonald, J. H., and Hogan, S. J. (2016). "Closed form solution of Eigen frequency of monopile supported offshore wind turbines in deeper waters incorporating stiffness of substructure and SSI." *Soil Dynamics and Earthquake Engineering*, 83, 18-32.

Astariz, S., Perez-Collazo, C., Abanades, J., and Iglesias, G. (2015). "Co-located wave-wind farms: Economic assessment as a function of layout." *Renewable Energy*, 83, 837-849.

Baldi, G., Belloti, R., Ghionna, V. N., Jamiolkowski, M., and Lo Presti, D. C. "Modulus of sands from CPTs and DMTs." *Proc., 12th International Conference on Soil Mechanics and Foundation Engineering*, A A Balkema, P165–170.

Baldi, G., Bellotti, R., Ghionna, V., Jamiolkowski, M., Marchetti, S., and Pasqualini, E. "Flat dilatometer tests in calibration chambers." *Proc., In-Situ '86, ASCE Special Conference on Use of in situ tests in geotechnical engineering*, ASCE Geotechnical Special Publication No. 6, 431-446.

Bhattacharya, S. (2014). "Challenges in design of foundations for offshore wind turbines." *Engineering & Technology Reference*, 1(1), 922.

Bhattacharya, S. (2019). *Design of foundations for offshore wind turbines*, Wiley Online Library.

Bhattacharya, S., Cox, J. A., Lombardi, D., and Wood, D. M. (2013). "Dynamics of offshore wind turbines supported on two foundations." *Proceedings of the Institution of Civil Engineers - Geotechnical Engineering*, 166(2), 159-169.

Bhattacharya, S., Lombardi, D., and Muir Wood, D. (2011). "Similitude relationships for physical modelling of monopile-supported offshore wind turbines." *International Journal of Physical Modelling in Geotechnics*, 11(2), 58-68.

Brinkgreve, R., Engin, E., and Engin, H. (2010). "Validation of empirical formulas to derive model parameters for sands." *Numerical methods in geotechnical engineering*, 137-142.

Brinkgreve, R., Kappert, M., and Bonnier, P. "Hysteretic damping in a small-strain stiffness model." *Proc., Proc. of the 10th International Symposium on Numerical Models in Geomechanics (NUMOG X)*, Taylor & Francis Group.

Brinkgreve, R. B. J. (2005). "Selection of Soil Models and Parameters for Geotechnical Engineering Application." *Soil Constitutive Models*, 69-98.

Brinkgreve, R. B. J., Zampich, L. M., and Mnoj, R. N. (2019a). *PLAXIS 3D Connect Edition V20 Material Models*.

Brinkgreve, R. B. J., Zampich, L. M., and Mnoj, R. N. (2019b). *PLAXIS 3D Connect Edition V20 Scientific Manual*.

Byrne, B., McAdam, R., Burd, H., Houlsby, G., Martin, C., Zdravkovic, L., Taborda, D., Potts, D., Jardine, R., and Sideri, M. (2015). "New design methods for large diameter piles under lateral loading for offshore wind applications." *Frontiers in offshore geotechnics III*, 705-710.

Carswell, W., Johansson, J., Løvholt, F., Arwade, S., Madshus, C., DeGroot, D., and Myers, A. (2015). "Foundation damping and the dynamics of offshore wind turbine monopiles." *Renewable energy*, 80, 724-736.

Carter, J. P., and Kulhawy, F. H. (1992). "Analysis of laterally loaded shafts in rock." *Journal of Geotechnical Engineering*, 118(6), 839-855.

Chen, C., and Duffour, P. (2018). "Modelling damping sources in monopile-supported offshore wind turbines." *Wind Energy*, 21(11), 1121-1140.

Chow, F. (1996). "Investigations into the behaviour of displacement piles for offshore foundations." PhD Thesis, Imperial College, University of London.

Cook, M. F., and Vandiver, J. K. "Measured and predicted dynamic response of a single pile platform to random wave excitation." *Proc., Offshore Technology Conference*, Offshore Technology Conference, 637-646.

Cox, W. R., Reese, L. C., and Grubbs, B. R. "Field testing of laterally loaded piles in sand." *Proc., Offshore Technology Conference*, Offshore Technology Conference.

D'Appolonia, D. J., and D'Appolonia, E. "Determination of the maximum density of cohesionless soils." *Proc., The Third Regional Conference On Soil Mechanics and Foundation Engineering*, 266- 268.

D'Appolonia, E. (1970). "Dynamic loadings." *Journal of Soil Mechanics & Foundations Divisison*, 96, No. SM I, 49-72.

Damgaard, M., Andersen, L. V., and Ibsen, L. B. (2015). "Dynamic response sensitivity of an offshore wind turbine for varying subsoil conditions." *Ocean engineering*, 101, 227-234.

Damgaard, M., Bayat, M., Andersen, L. V., and Ibsen, L. B. (2014). "Assessment of the dynamic behaviour of saturated soil subjected to cyclic loading from offshore monopile wind turbine foundations." *Computers and Geotechnics*, 61, 116-126.

Damgaard, M., Ibsen, L. B., Andersen, L. V., and Andersen, J. K. F. (2013). "Cross-wind modal properties of offshore wind turbines identified by full scale testing." *Journal of Wind Engineering and Industrial Aerodynamics*, 116, 94-108.

GAI Consultants, Inc., Monroeville, PA (1982). "Laterally loaded drilled pier research. Volume 2: Research documentation. ."Electric Power Research Institte (EPRI).

Devriendt, C., Jordaens, P. J., De Sitter, G., and Guillaume, P. (2013). "Damping estimation of an offshore wind turbine on a monopile foundation." *IET Renewable Power Generation*, 7(4), 401-412.

Đilas, L. D. (2018). "Estimation of Soil Damping Contribution on Offshore Monopiles Using Plaxis 3D Approach." Master of Science, Delft University of Technology.

DNV (2002). "Offshore Standard DNV-OS-J101: Design of Offshore Wind Turbine Structures." Det Norske Veritas, Hovik, Norway.

DNV (2009). " Offshore Standard DNV-OS-J101 Design of Offshore Wind Turbine Structures." Det Norske Veritas, Hovik, Norway.

DNV (2014). "Offshore Standard DNV-OS-J101: Design of Offshore Wind Turbine Structures." Det Norske Veritas, Hovik, Norway.

Dos Santos, J., and Correia, A. "Reference threshold shear strain of soil. Its application to obtain an unique strain-dependent shear modulus curve for soil." *Proc., Proceedings of the Fifteenth International Conference on Soil Mechanics and Geotechnical Engineering, Istanbul, Turkey, 27-31 August 2001. Volumes 1-3*, AA Balkema, 267-270.

University of California, Berkeley. Report no. UCB/GT/80-01 (1980). "Strength, stress-strain and bulk modulus parameters for finite element analyses of stresses and movements in soil masses."

Duncan, J. M., and Chang, C.-Y. (1970). "Nonlinear analysis of stress and strain in soils." *ASCE Journal of the Soil Mechanics and Foundation Division*, 96(5), 1629-1653.

Fan, C.-C., and Long, J. H. (2005). "Assessment of existing methods for predicting soil response of laterally loaded piles in sand." *Computers and Geotechnics*, 32(4), 274–289.

Fontana, C. M., Carswell, W., Arwade, S. R., DeGroot, D. J., and Myers, A. T. (2015). "Sensitivity of the dynamic response of monopile-supported offshore wind turbines to structural and foundation damping." *Wind Engineering*, 39(6), 609-627.

Frohboese, P., Schmuck, C., and Hassan, G. G. "Thrust coefficients used for estimation of wake effects for fatigue load calculation." *Proc., European Wind Energy Conference*, 1-10.

Gavin, K. G., and Lehane, B. M. (2003). "The shaft capacity of pipe piles in sand." *Canadian Geotechnical Journal*, 40(1), 36-45.

Gazetas, G. (1984). "Seismic response of end-bearing single piles." *International Journal of Soil Dynamics and Earthquake Engineering*, 3(2), 82-93.

Gil-Martín, L. M., Carbonell-Márquez, J. F., Hernández-Montes, E., Aschheim, M., and Pasadas-Fernández, M. (2012). "Dynamic magnification factors of SDOF oscillators under harmonic loading." *Applied mathematics letters*, 25(1), 38-42.

Georgia Tech Research Corporation (2013). "Assessment of energy production potential from ocean currents along the United States coastline."

Georgia Tech Research Corporation, Atlanta, GA (United States) (2011). "Assessment of energy production potential from tidal streams in the United States."

Hald, T., Mørch, C., Jensen, L., Bakmar, C., and Ahle, K. "Revisiting monopile design using py curves. Results from full scale measurements on Horns Rev." *Proc., Proceedings of European Offshore Wind 2009 Conference*.

Hansen, M. H., Thomsen, K., Fuglsang, P., and Knudsen, T. (2006). "Two methods for estimating aeroelastic damping of operational wind turbine modes from experiments." *Wind Energy*, 9(1-2), 179-191.

Hardin, B. O., and Black, W. L. (1966). "Sand Stiffness Under Various Triaxial Stresses." *Journal of the Soil Mechanics and Foundations Division*, 92(2), 27-42.

Hardin, B. O., and Black, W. L. (1968). "Vibration Modulus of Normally Consolidated Clay." *Journal of the Soil Mechanics and Foundations Division*, 94(2), 353-369.

Hardin, B. O., and Drnevich, V. P. (1972). "Shear modulus and damping in soils: measurement and parameter effects." *Journal of Soil Mechanics & Foundations Div*, 98(sm6).

Hardin, B. O., and Richart Jr, F. (1963). "Elastic wave velocities in granular soils." *Journal of Soil Mechanics & Foundations Division*, 89(Proc. Paper 3407).

IEC (2005). "International Standard IEC-61400-1. Wind turbines-Part 1: Design requirements, Third Edition ", International Electrotechnical Commission.

IEC (2009). "International Standard IEC-61400-3. Wind Turbines-Part 3: Design Requirements for Offshore Wind Turbines, First Edition." International Electrotechnical Commission.

International Renewable Energy Agency (2019). "Renewable Power Generation Costs in 2018."Abu Dhabi.

Electric Power Research Institute (2011). "Mapping and assessment of the United States ocean wave energy resource."

Jaky, J. (1944). "The Coefficient Of Earth Pressure At Rest." *Journal for Society of Hungarian Architects and Engineers*, 355-358.

Jalbi, S., Arany, L., Salem, A., Cui, L., and Bhattacharya, S. (2019). "A method to predict the cyclic loading profiles (one-way or two-way) for monopile supported offshore wind turbines." *Marine Structures*, 63, 65-83.

Jamiolkowsky, M., Ladd, C., Germaine, J., and Lancellotta, R. "New Developments In Field and Laboratory Testing Of Soils." *Proc., Proceedings Of the 11th International Conference On Soil Mechanics And Foundation Engineering*.

Janbu, N. "Soil compressibility as determined by odometer and triaxial tests." *Proc., Proc. Europ. Conf. SMFE*, 19-25.

Jardine, R., Chow, F., Overy, R., and Standing, J. (2005). *ICP design methods for driven piles in sands and clays*, Thomas Telford London.

Jensen, J. L. (1990). "Full-Scale Measurements of Offshore Platforms." *Fracture and Dynamics*(17).

Kallehave, D., Byrne, B. W., LeBlanc Thilsted, C., and Mikkelsen, K. K. (2015a). "Optimization of monopiles for offshore wind turbines." *Philosophical Transactions of the Royal Society A: Mathematical, Physical and Engineering Sciences*, 373(2035), 20140100.

Kallehave, D., Thilsted, C. L., and Liingaard, M. "Modification of the API py formulation of initial stiffness of sand." *Proc., Offshore site investigation and geotechnics: integrated technologies-present and future*, Society of Underwater Technology.

Kallehave, D., Thilsted, C. L., and Troya, A. "Observed variations of monopile foundation stiffness." *Proc., Frontiers in Offshore Geotechnics III: Proceedings of the 3rd International Symposium on Frontiers in Offshore Geotechnics (ISFOG 2015)*, Taylor & Francis Books Ltd, 717-722.

Kelly, R. B., Houlsby, G. T., and Byrne, B. W. (2006). "A comparison of field and laboratory tests of caisson foundations in sand and clay." *Géotechnique*, 56(9), 617-626.

Kim, Y., and Jeong, S. (2011). "Analysis of soil resistance on laterally loaded piles based on 3D soil–pile interaction." *Computers and Geotechnics*, 38(2), 248-257.

Ko, J., and Jeong, S. (2014). "Plugging effect of open-ended piles in sandy soil." *Canadian Geotechnical Journal*, 52(5), 535-547.

U.S. Department of Energy (DOE), Office of Energy Efficiency & Renewable Energy (EERE) (2020). "2018 Renewable Energy Data Book."

Kühn, M. J. (2001). "Dynamics and design optimisation of offshore wind energy conversion systems." DUWIND, Delft University Wind Energy Research Institute.

Electric Power Research Institute. EL-6800. Research Project 1493-06 (1990). "Manual on Estimating Soil Properties for Foundation Design."

Kuo, Y.-S., Achmus, M., and Abdel-Rahman, K. (2012). "Minimum Embedded Length of Cyclic Horizontally Loaded Monopiles." *Journal of Geotechnical and Geoenvironmental Engineering*, 138(3), 357-363.

Lam, I., and Law, H. "Soil-foundation-structure-interaction analytical considerations by empirical p-y methods." *Proc., Proc., 4th Caltrans Seismic Research Workshop*, California Dept. of Transportation, Engineering Service Center.

Laws, N. D., and Epps, B. P. (2016). "Hydrokinetic energy conversion: Technology, research, and outlook." *Renewable and Sustainable Energy Reviews*, 57, 1245-1259.

LeBlanc, C., Houlsby, G., and Byrne, B. (2010). "Response of stiff piles in sand to long-term cyclic lateral loading." *Géotechnique*, 60(2), 79-90.

Lin, C., Bennett, C., Han, J., and Parsons, R. L. (2010). "Scour effects on the response of laterally loaded piles considering stress history of sand." *Computers and Geotechnics*, 37(7), 1008-1014.

Lloyd, G. (2005). "Guideline for the Certification of Offshore Wind Turbines." Germanischer Lloyd Wind Energie.

Lunne, T., and Christoffersen, H. P. "Interpretation of cone penetrometer data for offshore sands." *Proc., Offshore Technology Conference*, Offshore Technology Conference, 181-192.

Magalhães, F., Cunha, Á., Caetano, E., and Brincker, R. (2010). "Damping estimation using free decays and ambient vibration tests." *Mechanical Systems and Signal Processing*, 24(5), 1274-1290.

Marchetti, S. "Sensitivity of CPT and DMT to stress history and aging in sands for liquefaction assessment." *Proc., Proc., 2nd Int. Symp. on Cone Penetration Testing (CPT'10)*, Technical Committee TC-16 of the ISSMGE in collaboration with California …, 3-50.

National Highway Institute, National Highway Institute (2001). "Manual on Subsurface Investigations."

Mayne, P. W., and Kulhawy, F. H. (1982). "Ko-OCR relationships in soil." *Journal of the Geotechnical Engineering Division*, 108(6), 851-872.

McAdam, R. A., Byrne, B. W., Houlsby, G. T., Beuckelaers, W. J., Burd, H. J., Gavin, K. G., Igoe, D. J., Jardine, R. J., Martin, C. M., and Muir Wood, A. (2019). "Monotonic laterally loaded pile testing in a dense marine sand at Dunkirk." *Géotechnique*, 1-13.

Center for Highway Research, University of Texas at Austin TX (1979). "Analysis of single piles under lateral loading."

Mitchell, J. K., and Soga, K. (2005). *Fundamentals of soil behavior*, John Wiley & Sons New York.

Morison, J., Johnson, J., and Schaaf, S. (1950). "The force exerted by surface waves on piles." *Journal of Petroleum Technology*, 2(05), 149-154.

Murchison, J. M., and O'Neill, M. W. "Evaluation of py relationships in cohesionless soils." *Proc., Analysis and design of pile foundations*, ASCE, 174-191.

Murphy, G., Igoe, D., Doherty, P., and Gavin, K. (2018). "3D FEM approach for laterally loaded monopile design." *Computers and Geotechnics*, 100, 76-83.

National Renewable Energy Lab.(NREL), Golden, CO (United States) (2016). "2016 Offshore Wind Energy Resource Assessment for the United States."

National Renewable Energy Lab.(NREL), Golden, CO (United States) (2019). "2018 Offshore Wind Technologies Market Report."

Paik, K., and Salgado, R. (2004). "Effect of pile installation method on pipe pile behavior in sands." *Geotechnical Testing Journal*, 27(1), 78-88.

Pender, M. (1993). "Aseismic pile foundation design analysis." *Bulletin of the New Zealand Society for Earthquake Engineering*, 26(1), 49-160.

Pérez-Collazo, C., Greaves, D., and Iglesias, G. (2015). "A review of combined wave and offshore wind energy." *Renewable and Sustainable Energy Reviews*, 42, 141-153.

Perez, C., and Iglesias, G. "Integration of wave energy converters and offshore windmills." *Proc., http://www. icoe-conference. com.*

Poulos, H. G., and Davis, E. H. (1980). *Pile foundation analysis and design*.

Prendergast, L. J., Gavin, K., and Doherty, P. (2015). "An investigation into the effect of scour on the natural frequency of an offshore wind turbine." *Ocean Engineering*, 101, 1-11.

Prendergast, L. J., Hester, D., Gavin, K., and O'sullivan, J. (2013). "An investigation of the changes in the natural frequency of a pile affected by scour." *Journal of Sound and Vibration*, 332(25), 6685-6702.

Randolph, M. F. (1981). "The response of flexible piles to lateral loading." *Géotechnique*, 31(2), 247-259.

Reese, L. C., Cox, W. R., and Koop, F. D. "Analysis of laterally loaded piles in sand." *Proc., 6th Offshore Technology Conference*, 473-483.

Reese, L. C., and Van Impe, W. F. (2011). *Single piles and Pile groups under lateral loading, 2nd Edition*, CRC Press.

Rezaei, R., Fromme, P., and Duffour, P. (2018). "Fatigue life sensitivity of monopile-supported offshore wind turbines to damping." *Renewable Energy*, 123, 450-459.

University of California, Berkeley. Report no. EERC 70-10 (1970). "Soil moduli and damping factors for dynamic response analysis."Earthquake Engineering Research Centre.

Shadlou, M., and Bhattacharya, S. (2016). "Dynamic stiffness of monopiles supporting offshore wind turbine generators." *Soil Dynamics and Earthquake Engineering*, 88, 15-32.

Shirzadeh, R., Devriendt, C., Bidakhvidi, M. A., and Guillaume, P. (2013). "Experimental and computational damping estimation of an offshore wind turbine on a monopile foundation." *Journal of Wind Engineering and Industrial Aerodynamics*, 120, 96-106.

Silver, M. L., and Seed, H. B. (1971). "Volume Changes in Sands during Cyclic Loading." *Journal of the Soil Mechanics and Foundations Division*, 97(9), 1171-1182.

Sørensen, S. P. H., and Ibsen, L. B. (2013). "Assessment of foundation design for offshore monopiles unprotected against scour." *Ocean Engineering*, 63, 17-25.

Taborda, D. M. G., Zdravković, L., Potts, D. M., Burd, H. J., Byrne, B. W., Gavin, K. G., Houlsby, G. T., Jardine, R. J., Liu, T., Martin, C. M., and McAdam, R. A. (2019). "Finite-element modelling of laterally loaded piles in a dense marine sand at Dunkirk." *Géotechnique*, 0(0), 1-16.

Tarp-Johansen, N. J., Andersen, L., Christensen, E. D., Mørch, C., Frandsen, S., and Kallesøe, B. "Comparing sources of damping of cross-wind motion." *Proc., European Offshore Wind 2009: Conference & Exhibition: 14-16 September, Stockholm, Sweden*, The European Wind Energy Association.

Terzaghi, K. (1955). "Evaluation of Coefficients of Subgrade Reaction." *Géotechnique*, 5(4), 297-326.

Terzaghi, K., and Peck, R. B. (1967). *Soil mechanics in engineering practice*, John Wiley & Sons.

Vardhanabhuti, B., and Mesri, G. (2007). "Coefficient of earth pressure at rest for sands subjected to vibration." *Canadian geotechnical journal*, 44(10), 1242-1263.

Versteijlen, W. G., Metrikine, A., Hoving, J., Smidt, E., and de Vries, W. (2011). "Estimation of the vibration decrement of an offshore wind turbine support structure caused by its interaction with soil." *Knowledge, Technology & Policy*.

Vo, L. H. (2016). "Determination of P-y Curves for Sand by Laboratory Experiments and Three-dimensional Numerical Analyses of Laterally Loaded Piles." Master of Science, North Carolina State University, Raleigh.

Wallace, J. W., Fox, P. J., Stewart, J. P., Janoyan, K., Tong, Q., and Lermitte, S. P. (2002). "Cyclic large deflection testing of shaft bridges part II: analytical studies." *Report from California Dept. of Transportation*.

Whitman, R. V., and Ortigosa, P. O. "Densification of Sand by Vertical Vibrations." *Proc., The 4th World Conference on Earthquake Engineering*.

Wiser, R., Lantz, E., Mai, T., Zayas, J., DeMeo, E., Eugeni, E., Lin-Powers, J., and Tusing, R. (2015). "Wind vision: A new era for wind power in the United States." *The Electricity Journal*, 28(9), 120-132.

Wroth, C. (1979). "A review of the engineering properties of soils with particular reference to the shear modulus." *OUEL Report 1523/84, Univ. of Oxford*.

Wroth, C., and Houlsby, G. (1985). "Soil mechanics-property characterization and analysis procedures."

Yan, L., and Byrne, P. M. (1992). "Lateral pile response to monotonic pile head loading." *Canadian Geotechnical Journal*, 29(6), 955-970.

Yang, Z. X., Jardine, R. J., Zhu, B. T., and Rimoy, S. (2014). "Stresses Developed around Displacement Piles Penetration in Sand." *Journal of Geotechnical and Geoenvironmental Engineering*, 140(3), 04013027.

Youd, T. L. (1972). "Compaction of Sands by Repeated Shear Straining." *Journal of the Soil Mechanics and Foundations Division*, 98(7), 709-725.

Zaaijer, M. (2006). "Foundation modelling to assess dynamic behaviour of offshore wind turbines." *Applied Ocean Research*, 28(1), 45-57.

Zania, V. (2014). "Natural vibration frequency and damping of slender structures founded on monopiles." *Soil dynamics and Earthquake engineering*, 59, 8-20.

Zanke, U. C., Hsu, T.-W., Roland, A., Link, O., and Diab, R. (2011). "Equilibrium scour depths around piles in noncohesive sediments under currents and waves." *Coastal Engineering*, 58(10), 986-991.

Zdravković, L., Jardine, R. J., Taborda, D. M. G., Abadias, D., Burd, H. J., Byrne, B. W., Gavin, K. G., Houlsby, G. T., Igoe, D. J. P., Liu, T., Martin, C. M., McAdam, R. A., Wood, A. M.,

Potts, D. M., Gretlund, J. S., and Ushev, E. (2019). "Ground characterisation for PISA pile testing and analysis." *Géotechnique*, 0(0), 1-16.

Zhang, L., Silva, F., and Grismala, R. (2005). "Ultimate Lateral Resistance to Piles in Cohesionless Soils." *Journal of Geotechnical and Geoenvironmental Engineering*, 131(1), 78-83.

Zuo, H., Bi, K., and Hao, H. (2018). "Dynamic analyses of operating offshore wind turbines including soil-structure interaction." *Engineering Structures*, 157, 42-62.

APPENDICES

7.1. Appendix A. Data on natural frequency and foundation damping resulted from dynamic analyses

Table 7.1. Natural frequency of D_P=5.0m monopile

D_R(%) / L_P (m)	100	75	50	25
38	0.325	0.319	0.319	0.316
31.2	0.325	0.319	0.319	0.316
24	0.325	0.319	0.316	0.313
19.2	0.322	0.316	0.313	0.309

Table 7.2. Natural frequency of D_P=4.7m monopile

D_R(%) / L_P (m)	100	75	50	25
38	0.309	0.306	-	0.300
31.2	-	-	-	-
24	0.309	0.306	-	0.297
19.2	0.306	0.303	-	0.294

Table 7.3. Natural frequency of D_P=4.4m monopile

D_R(%) / L_P (m)	100	75	50	25
38	0.291	0.288		0.283
31.2	-	-	-	-
24	0.291	0.288		0.281
19.2	0.288	0.284		0.278

Table 7.4. Natural frequency of D_P=4.0m monopile

D_R(%) / L_P (m)	100	75	50	25
38	0.263	0.260		0.254
31.2	-	-	-	-
24	0.263	0.26		0.254
19.2	0.26	0.256		0.250

Table 7.5. Foundation damping of D_P=5.0m monopile

D_R(%) / L_P (m)	100	75	50	25
38	0.330	0.35	0.5	0.75
31.2	0.35	0.4	0.55	0.65
24	0.4	0.5	0.7	0.9
19.2	0.5	0.72	1	1.4

Table 7.6. Foundation damping of D_P=4.7m monopile

D_R(%) / L_P (m)	100	75	50	25
38	0.800	1.050		1.400
31.2	-	-	-	-
24	0.900	1.050		1.500
19.2	1.050	1.300		2.000

Table 7.7. Foundation damping of D_P=4.4m monopile

D_R(%) / L_P (m)	100	75	50	25
38	1.00	1.20		1.60
31.2	-	-	-	-
24	1.00	1.20		1.70
19.2	1.10	1.40		2.20

Table 7.8. Foundation damping of D_P=4.0m monopile

D_R(%) / L_P (m)	100	75	50	25
38	1.1	1.3		1.80
31.2	-	-	-	-
24	1.1	1.3		1.8
19.2	1.2	1.5		2.5

7.2. Appendix B. Data on pile deformations at mudline and dynamic properties resulted from numerical simulations.

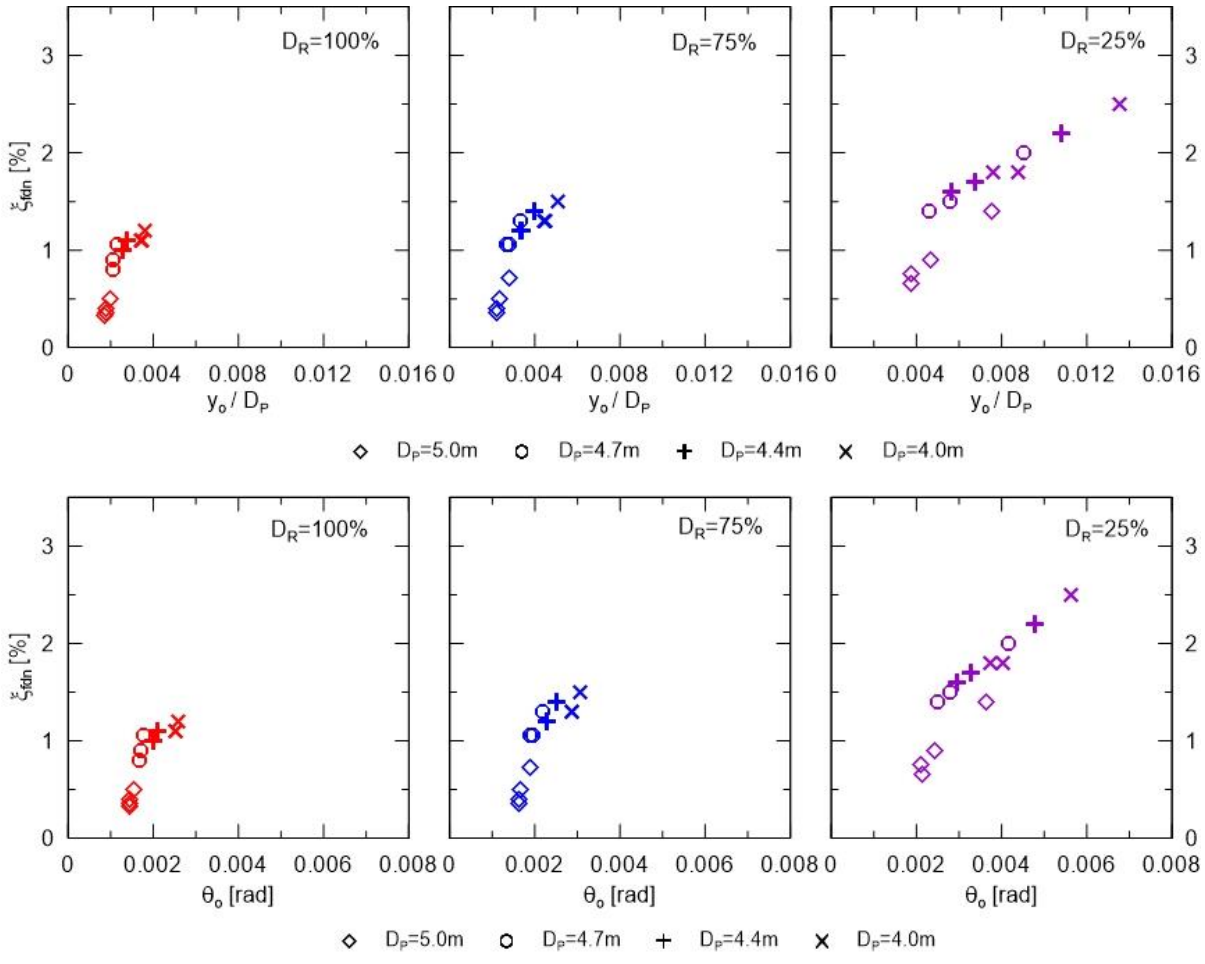

Figure 7.1. Data points of (y_o/D_P, ξ_{fdn}) (top), and (θ_o, ξ_{fdn}) (bottom) at different soil D_R.

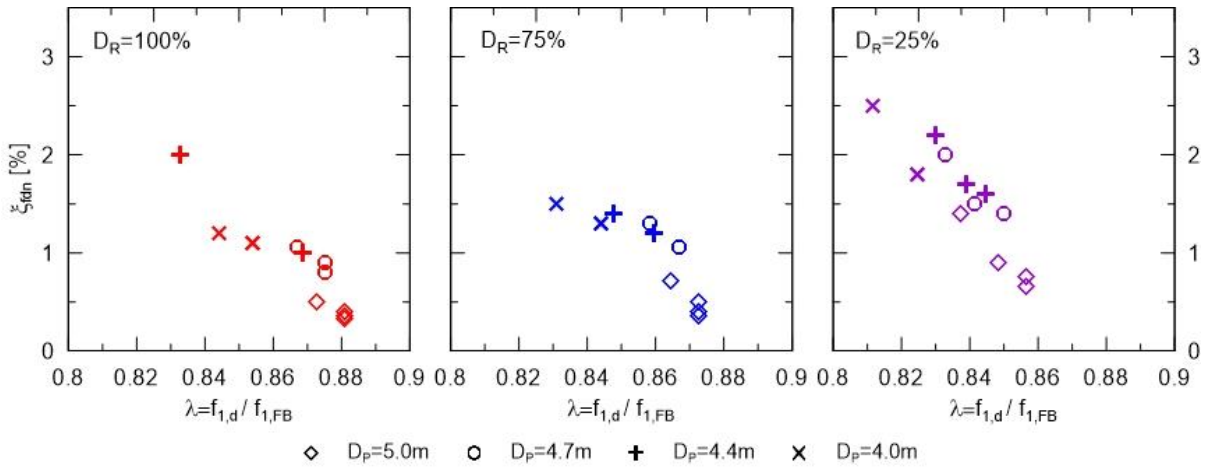

Figure 7.2. Data points of (λ, ξ_{fdn}) at different soil D_R

7.3. Appendix C. Data natural frequency and foundation damping resulted from numerical simulations for monopile with presence of local scour

Table 7.9. λ obtained from FE simulations and Approach 1 for monopile with L_P=38.0m and presence of local scour.

Pile	**S_L (m)**	**f_{FEM} (Hz)**	**$\lambda_{FEM,o}$ (f_{FEM}/ $f_{1,FBo}$)**	**$\lambda_{FEM,s}$ (f_{FEM}/ $f_{1,Fbo}$)**	**$\lambda_{A,o}$ (Eq. 4.27)**	**$\lambda_{A,s}$ (Eq. 4-27)**
L_P38-D_R100	4.8	0.313	0.848	0.907	0.861	0.882
	7.2	0.303	0.821	0.907	0.853	0.881
L_P38-D_R75	4.8	0.306	0.829	0.886	0.857	0.875
	7.2	0.297	0.805	0.889	0.849	0.875
L_P38-D_R50	4.8	0.303	0.821	0.878	0.853	0.869
	7.2	0.294	0.797	0.880	0.846	0.869
L_P38-D_R25	4.8	0.300	0.813	0.869	0.846	0.860
	7.2	0.290	0.786	0.868	0.841	0.862

Table 7.10. λ obtained from FE simulations and Approach 1 for monopile with L_P=24.0m and presence of local scour.

Pile	**S_L (m)**	**f_{FEM} (Hz)**	**$\lambda_{FEM,o}$ (f_{FEM}/ $f_{1,FBo}$)**	**$\lambda_{FEM,s}$ (f_{FEM}/ $f_{1,Fbo}$)**	**$\lambda_{A,o}$ (Eq. 4.27)**	**$\lambda_{A,s}$ (Eq. 4-27)**
L_P24-D_R100	4.8	0.313	0.848	0.907	0.861	0.882
	7.2	0.303	0.821	0.907	0.853	0.881
L_P24-D_R75	4.8	0.306	0.829	0.886	0.857	0.875
	7.2	0.297	0.805	0.889	0.849	0.875
L_P24-D_R50	4.8	0.303	0.821	0.878	0.853	0.869
	7.2	0.294	0.797	0.880	0.846	0.869
L_P24-D_R25	4.8	0.300	0.813	0.869	0.846	0.860
	7.2	0.290	0.786	0.868	0.841	0.862

Table 7.11. ξ_{fdn} obtained from FE simulations and Approach 1 for monopile with L_P=38.0m and presence of local scour.

Pile	**S_L (m)**	**$\xi_{fdn,FEM}$ (%)**	**$\xi_{fdn\ A,o}$ (Eq. 4.39)**	**$\xi_{fdn\ A,s}$ (Eq. 4.39)**
L_P38-D_R100	4.8	0.620	0.88	0.61
	7.2	0.680	1.04	0.63
L_P38-D_R75	4.8	0.660	0.96	0.69
	7.2	0.720	1.12	0.71
L_P38-D_R50	4.8	0.750	1.04	0.77
	7.2	0.800	1.20	0.79
L_P38-D_R25	4.8	0.830	1.18	0.88
	7.2	0.860	1.32	0.89

Table 7.12. ξ_{fdn} obtained from FE simulations and Approach 1 for monopile with L_P=24.0m and presence of local scour.

Pile	**S_L (m)**	**$\xi_{fdn,FEM}$ (%)**	**$\xi_{fdn\ A,o}$ (Eq. 4.39)**	**$\xi_{fdn\ A,s}$ (Eq. 4.39)**
L_P24-D_R100	4.8	0.65	0.89	0.58
	7.2	0.80	1.10	0.68
L_P24-D_R75	4.8	0.65	1.01	0.63
	7.2	0.80	1.26	0.74
L_P24-D_R50	4.8	0.70	1.21	0.74
	7.2	0.85	1.62	0.85
L_P24-D_R25	4.8	0.90	1.54	0.94
	7.2	1.05	2.09	1.07